Karlsruher Institut für Technologie

Electroweak Phase Transition in the Next-to-Two Higgs Doublet Model

Masterarbeit
von

Jonas Müller

An der Fakultät für Physik
Institut für Theoretische Physik

Referent: Prof. Dr. M. M. Mühlleitner (KIT, Karlsruhe)
Korreferent: PD Dr. S. Gieseke (KIT, Karlsruhe)

Bearbeitungszeit: 1. Dezember 2016 – 1. Dezember 2017

Hiermit versichere ich, dass ich die vorliegende Arbeit selbständig verfasst und keine anderen als die angegebenen Hilfsmittel benutzt, die wörtlich oder inhaltlich übernommenen Stellen als solche kenntlich gemacht und die Satzung des Karlsruher Instituts für Technologie (KIT) zur Sicherung guter wissenschaftlicher Praxis in der aktuell gültigen Fassung beachtet habe.

Karlsruhe, den 1.12.2017

....

(**Jonas Müller**)

Als Masterarbeit akzeptiert ....

Contents

1 Introduction **1**

2 Theoretical Background **5**
- 2.1 Field Theory at Finite Temperature 5
- 2.2 The Effective Potential 9
- 2.3 Resummation in Hot Field Theory 15

3 The N2HDM **21**
- 3.1 The N2HDM Higgs Sector 21
- 3.2 The Effective Potential in the N2HDM 24

4 Renormalisation **27**

5 Numerical Analysis **31**
- 5.1 Minimisation of the Potential 31
- 5.2 Constraints and Parameter Scan 32
- 5.3 General Idea of the Analysis 35

6 Results **37**
- 6.1 NLO Constraints 37
- 6.2 Electroweak Phase Transition 38
- 6.3 Triple Couplings of the Massive Particles 59

7 Conclusion **65**

Acknowledgments/Danksagungen **67**

Bibliography **69**

CHAPTER 1

Introduction

One of the outstanding problems in today's physics is to explain the baryon asymmetry of the universe (BAU). The Planck experiment determines the BAU to [1]

$$\frac{n_B}{s} \equiv Y_B = (8.59 \pm 0.11) \cdot 10^{-11} \tag{1.1}$$

where n_B is the baryon number and s the entropy density of the universe. In the general understanding of the universe, where it starts with a total balance of baryons and anti-baryons in the big bang, a dynamical production mechanism is needed for the net baryon number. To enable such a dynamical mechanism, Sakharov [2] proposed three sufficient conditions, which a model needs to fulfill in order to explain the BAU. As a first point, the model has to include baryon number violating processes. This is already possible in the Standard Model (SM) through the chiral anomaly [3]. At finite temperature, the tunneling between two vacua is viable via a sphaleron at a sufficient rate, which results in the $B + L$ violation (B is the baryon and L the lepton number), while $B - L$ is still conserved. The second Sakharov condition concerns the requirement of additional CP and C violation, otherwise the corresponding anti process would wash out the generated baryons and one ends in a symmetric universe again. The last condition is the departure from thermal equilibrium. This prevents thermal suppression due to the Boltzmann factor.

For many years now, electroweak baryogenesis (EWB) has been considered as a possible solution which simultaneously fulfills the Sakharovs conditions and provides promising and testable predictions for the Large Hardron Collider (LHC) due to the strong connection to the electroweak sector. In this mechanism, the baryons are produced by the electroweak phase transition (EWPT), which occurs in the early universe. At the beginning of the universe, the SU(2) $\times$ U(1) gauge symmetry is still unbroken. Since the temperature decreases with the evolution of the universe, bubbles with the broken gauge symmetry start to form. Two vacua coexist and CP-violating processes at the bubble wall with top quarks and sphalerons will produce baryons inside the bubbles [4]. If the phase transition (PT) occurs *fast enough*, the produced baryons cannot be *washed out* again via sphaleron interactions at the bubble wall. In order to secure the baryon number, the PT must be of strong first order. This condition can be translated in the *baryon wash out condition* [5]

$$\xi_C \equiv \frac{\langle \phi_C \rangle}{T_C} \geq 1\,. \tag{1.2}$$

The critical temperature T_C is defined as the temperature at which the two vacuum states of the symmetric and broken phase are degenerate, $\langle \phi_C \rangle$ describes the corresponding field configuration of the broken phase at this critical point.
Although the three Sakharov conditions can be fulfilled in the SM, the CP-violation in the Cabibbo-Kobayashi-Maskawa (CKM) matrix is not sufficient [6]. In addition, with the discovery of the SM Higgs boson at the LHC [7], it is known that the Higgs boson is too heavy to enable a strong first order PT in the SM [8, 9]. For all these reasons, physics beyond the SM is needed. For example, additional scalar degrees of freedom can strengthen the PT, such that EWB is possible.
In this work, we study the implications of the strong first order electroweak phase transition (SFOEWPT) for an extended Higgs sector and its phenomenology. There is already a large number of studies of extended Higgs sector models in combination with an EWPT, which includes an additional Higgs doublet, like the two-Higgs doublet model (2HDM) [10–14], or singlet extensions which consider the SM Higgs sector plus a gauge singlet [15–17]. There are also studies which consider supersymmetry like the minimal supersymmetric [18–20] and the next-to-minimal supersymmetric extension of the SM [21, 22].
In this thesis we investigate the Next-to-Two Higgs Doublet Model (N2HDM), which is a CP-conserving 2HDM extended with an additional real singlet. This will allow us to see effects induced by additional doublets and singlets at the same time without the restriction of supersymmetry. The degrees of freedom after electroweak symmetry breaking are the neutral and charged would-be Goldstone bosons G^0 and $G^\pm$, respectively, the CP-odd pseudoscalar A, the charged Higgs boson $H^\pm$ and the three CP-even Higgs bosons.
In order to describe the interplay between the SFOEWPT and the collider phenomenology, we will use the baryon washout condition, given in Eq. (1.2), to quantify if an SFOEWPT is possible in a specific parameter setting. For that purpose, we have calculated the effective potential at finite temperature including two-loop thermal effects by using the daisy resummation. We chose the renormalisation prescription introduced in [14], which allows us to use one-loop masses and mixing angles as direct input for the parameter scan. We will use numerical minimisation algorithms to find the global electroweak minimum of the effective potential in order to determine the critical field configuration $\langle \phi_C \rangle$ and the critical temperature T_C.
The demand of a first order EWPT will constrain the viable parameter phase space, which survives the collider and theoretical constraints. This will allow us to link collider phenomenology with cosmology and leads to testable predictions for future collider experiments.
The outline of this work is as follows: In Chapter 2 we start with a review of the theoretical background, which is needed to cover the calculations, including finite temperature field theory and the effective potential at one-loop approximation and at finite temperature. We will furthermore make some comments on subtle problems of the finite temperature field theory and introduce the resummation prescription used

in this work. Afterwards, in Chapter 3, we introduce our notation and the N2HDM. We will show schematically the diagonalisation of the extended Higgs sector and present the calculation of the mass spectrum. In Chapter 4 the renormalisation prescription is described in detail and in Chapter 5, we will give details on the numerical analysis. In Chapter 6 we will discuss the phenomenological implications of the EWPT for the N2HDM. At the end, in Chapter 7, we will give our conclusion.

CHAPTER 2

Theoretical Background

In the following chapter we will introduce the theoretical basics needed to cover the calculations in this thesis. For more detailed explanations, we will refer to the literature where appropriate. The chapter starts with an introduction to field theory at finite temperature and derives an analytic expression for the one-loop effective potential. This effective potential takes the one-loop quantum corrections into account which allows us to investigate the electroweak symmetry breaking patterns at one-loop approximation. We will also treat the Debye-corrections which allow us to go beyond the one-loop approximation.

2.1 Field Theory at Finite Temperature

There are different ways to formulate a field theory at finite temperature. In principle it is possible to perform all calculations in each of the proposed formalisms, but it is convenient to use the imaginary time formalism for our purposes. Hence, we follow the introduction of [23].

To describe a system that is capable of exchanging energy and particles with a heat bath, the grand canonical ensemble with its partition function is needed,

$$Z(T) = \mathrm{Tr}\,\rho(\beta) = \mathrm{Tr}\exp\left(-\beta\mathcal{H}\right)\,, \tag{2.1}$$

where β is the inverse temperature (in natural units), ρ the density matrix and $\mathcal{H}$ describes the Hamiltonian of the system with the chemical potential μ,

$$\mathcal{H} = H - \mu\,. \tag{2.2}$$

In a statistical ensemble only the thermal averages are observable. They are defined for an operator $\mathcal{O}$ as

$$\langle\mathcal{O}\rangle_\beta = \frac{1}{Z(\beta)}\,\mathrm{Tr}\,\rho(\beta)\mathcal{O}\,. \tag{2.3}$$

Using the cyclicity of the trace leads to the so called Kubo-Martin-Schwinger equation for two Heisenberg-operators $\mathcal{O}_1$ and $\mathcal{O}_2$ at times t and t'

$$\langle\mathcal{O}_1(t)\mathcal{O}_2(t')\rangle_\beta = Z^{-1}\,\mathrm{Tr}\,\mathrm{e}^{-\beta H}\mathcal{O}_1(t)\mathcal{O}_2(t') \tag{2.4}$$

$$
\begin{aligned}
&= Z^{-1}\,\mathrm{Tr}\,\mathrm{e}^{-\beta H}\mathcal{O}_1(t)\mathrm{e}^{+\beta H}\mathrm{e}^{-\beta H}\mathcal{O}_2(t') \\
&= Z^{-1}\,\mathrm{Tr}\,\mathcal{O}_1(t+i\beta)\mathrm{e}^{-\beta H}\mathcal{O}_2(t') \\
&= \langle \mathcal{O}_2(t')\mathcal{O}_1(t+i\beta)\rangle_\beta \; .
\end{aligned}
$$

As can be read off Eq. (2.4), in thermal field theory the time is no longer a real quantity, which will be a crucial aspect of the following discussion. One of many reasons for this is that it is possible to identify the partition function as the functional representation of the path integral, if one allows complex time. Treating the temperature as a new time scale of the physical system will induce a periodicity in the complex time plane. To motivate the transition from the simple Euclidean space $\mathbb{R}^4$ to the periodic space $\mathbb{R}^3 \times S^1$, it is easier to consider the operator approach. For that, we define the thermal n point Greens function as

$$
\mathcal{G}_\beta(x_1 \dots x_n) = \langle \mathcal{T}_C \phi(x_1) \dots \phi(x_n) \rangle \tag{2.5}
$$

with the path order operator $\mathcal{T}_C$. This operator orders the fields $\phi(x_i)$ along the path $C \subset \mathbb{C}$, which corresponds to the *time plane*. Suppose one has a parameterization $z(\tau)$ for the path C with monotonically increasing and real τ, then this triggers the following correspondence for the step-functions[1],

$$
\Theta_C(t-t') = \Theta(\tau - \tau') \, . \tag{2.6}
$$

With this in mind it is possible to split the Greens function as

$$
\mathcal{G}_\beta(x-y) = \mathcal{G}^+_\beta(x-y)\Theta_C(x^0-y^0) + \mathcal{G}^-_\beta(x-y)\Theta_C(y^0-x^0) \tag{2.7}
$$

in two different time-ordered regions with

$$
\mathcal{G}^+_\beta(x-y) = \langle \phi(x)\phi(y)\rangle_\beta = \mathcal{G}^-_\beta(y-x) \, . \tag{2.8}
$$

Then, we insert a complete set of eigenstates $H\,|n\rangle = E_n\,|n\rangle$, taking $\vec{x} = \vec{y} = 0$ so that

$$
\mathcal{G}^+_\beta = \left\langle \phi(x^0,\vec{0})\phi(y^0,\vec{0}) \right\rangle_\beta \sim \sum_{n,m} \left|\, \langle m|\,\phi(0)\,|n\rangle \,\right|^2 \mathrm{e}^{-\mathrm{i}E_n(x^0-y^0)}\mathrm{e}^{\mathrm{i}E_m(x^0-y^0+\mathrm{i}\beta)} \, . \tag{2.9}
$$

The extra exponent $\sim \beta E_m$ originates from the thermal average definition in Eq. (2.3). In order to have a well defined Greens function, $\mathcal{G}^+_\beta$ needs to converge. Therefore one can conclude

$$
-\beta \leqslant \mathrm{Im}(x^0-y^0) \leqslant 0 \tag{2.10}
$$

and in a completely analogous way for $\mathcal{G}^-_\beta$,

$$
0 \leqslant \mathrm{Im}(x^0-y^0) \leqslant \beta \, . \tag{2.11}
$$

Finally one obtains

$$
-\beta \leqslant \mathrm{Im}(x^0-y^0) \leqslant \beta \tag{2.12}
$$

[1] Note that t is complex. Therefore Θ_C refers to the path ordered case and Θ to the well known step function.

for the whole Greens function. By choosing the Matsubara integration contour [24] $t \to -\mathrm{i}\tau$ and using the periodicity of the Greens function for bosonic fields (+) and fermionic fields (−) in Eq. (2.4), it can be shown that,

$$\mathcal{G}_\beta(\tau \le 0) = \pm \mathcal{G}_\beta(\tau + \beta)\,, \tag{2.13}$$

where +(−) corresponds to bosonic (fermionic) fields. Since the Greens functions are periodic in τ, the corresponding Fourier transformation contains discrete sums over frequencies and we can write a general expression for the time part of the Greens function,

$$\mathcal{G}_\beta(\tau) = \frac{1}{\beta}\sum_n \mathrm{e}^{-\mathrm{i}\omega_n\tau}\mathcal{G}_\beta(\omega_n) \tag{2.14}$$

and

$$\mathcal{G}_\beta(\omega_n) = \frac{1}{2}\int_{-\beta}^{\beta} d\tau \mathrm{e}^{\mathrm{i}\omega_n\tau}\mathcal{G}_\beta(\tau) \tag{2.15}$$

with frequencies

$$\omega_n = \frac{\pi n}{\beta}\,. \tag{2.16}$$

By using Eq. (2.13) it can be proven that the two point function vanishes for odd n in the bosonic case and for even n in the fermionic case,

$$\begin{aligned}
\mathcal{G}_\beta(\omega_n) =& \frac{1}{2}\int_{-\beta}^{0} d\tau \mathrm{e}^{\mathrm{i}\omega_n\tau}\mathcal{G}_\beta(\tau) + \frac{1}{2}\int_{0}^{\beta} d\tau \mathrm{e}^{\mathrm{i}\omega_n\tau}\mathcal{G}_\beta(\tau) \\
=& \pm\frac{1}{2}\int_{-\beta}^{0} d\tau \mathrm{e}^{\mathrm{i}\omega_n\tau}\mathcal{G}_\beta(\tau+\beta) + \frac{1}{2}\int_{0}^{\beta} d\tau \mathrm{e}^{\mathrm{i}\omega_n\tau}\mathcal{G}_\beta(\tau) \\
=& \pm\frac{1}{2}\int_{0}^{\beta} d\tau \mathrm{e}^{\mathrm{i}\omega_n(\tau-\beta)}\mathcal{G}_\beta(\tau) + \frac{1}{2}\int_{0}^{\beta} d\tau \mathrm{e}^{\mathrm{i}\omega_n\tau}\mathcal{G}_\beta(\tau) \\
=& \frac{1}{2}\left(1 \pm \mathrm{e}^{-\mathrm{i}\omega_n\beta}\right)\int_{0}^{\beta} d\tau \mathrm{e}^{\mathrm{i}\omega_n\tau}\mathcal{G}_\beta(\tau) \\
=& \frac{1}{2}\left(1 \pm (-1)^n\right)\int_{0}^{\beta} d\tau \mathrm{e}^{\mathrm{i}\omega_n\tau}\mathcal{G}_\beta(\tau)\,.
\end{aligned} \tag{2.17}$$

As a consequence, we introduce the so-called Matsubara frequencies,

$$\omega_n = \begin{cases} \frac{2\pi n}{\beta} & \text{for bosons} \\ \frac{(2n+1)\pi}{\beta} & \text{for fermions} \end{cases} \tag{2.18}$$

and we can formulate an expression for a two-point Greens function,

$$\mathcal{G}_\beta(\vec{x},\tau) = \frac{1}{\beta}\sum_n \int \frac{d^3k}{(2\pi)^3}\mathrm{e}^{-\mathrm{i}(\omega_n\tau - \vec{k}\vec{x})}\mathcal{G}_\beta(\vec{k},\omega_n)\,. \tag{2.19}$$

This Fourier decomposition can be used to obtain the propagator of the fields, for example for a real scalar field in Euclidean space time

$$\left(\frac{\partial^2}{\partial\tau^2} + \nabla^2 - m^2\right)\mathcal{G}_\beta(\vec{x},\tau) = -\delta^{(3)}(x)\delta(\tau)\,.$$

It is solvable in the momentum space with

$$\mathcal{G}_\beta(\vec{k},\omega_n) = \frac{1}{\omega_n^2 + \vec{k}^2 + m^2}\,. \tag{2.20}$$

As a more convenient way of obtaining Feynman rules, the path integral formalism can be taken into account. For this we look at the zero temperature transition amplitude in its functional representation

$$\big\langle \phi(\vec{x}_1,t_1)\big|\phi(\vec{x}_2,t_2)\big\rangle \sim \int \mathcal{D}\phi \mathrm{e}^{\mathrm{i}S} \tag{2.21}$$

with the common action

$$S[\phi] = \int\limits_{t_1}^{t_2} dt \int d^3x \mathcal{L} \tag{2.22}$$

and fixed boundaries

$$\phi(\vec{x_1},t_1) = \phi_1 \tag{2.23}$$
$$\phi(\vec{x_2},t_2) = \phi_2\,. \tag{2.24}$$

We already saw the periodicity of the Greens function in the time component, hence the fields must fulfill those periodic boundary conditions as well,

$$\phi(\vec{x},\beta) = \pm\phi(\vec{x},0)\,. \tag{2.25}$$

Identifying

$$t_1 - t_2 = -\mathrm{i}\beta \tag{2.26}$$

one can write the partition function of the theory in a path integral representation

$$Z(\beta) = \mathrm{Tr}\,\mathrm{e}^{-\beta\mathcal{H}} = \int \mathcal{D}\phi \,\langle\phi|\mathrm{e}^{-\beta\mathcal{H}}|\phi\rangle = N' \int \mathcal{D}\phi \mathrm{e}^{-S_E} \tag{2.27}$$

with the Euclidean action[2]

$$S_E = \int_0^\beta d\tau \int d^3x \mathcal{L}_E\,. \tag{2.28}$$

To end this short motivation for thermal field theory, we rephrase the Matsubara formalism. It enables the formulation of the partition function of a quantum theory by its path integral. The Wick rotation of the time axes to its complex axis consequently allows to obtain a theory in Euclidean space time. The boundary conditions are not given at $t = \pm\infty$ anymore, but at a finite interval, which is defined by the temperature $\beta = T^{-1}$ in natural units. This transition

$$\mathbb{R}^4 \to \mathbb{R}^3 \times S^1 \tag{2.29}$$

also requires that the fields satisfy (anti-) periodic boundary conditions with a period of β. The Feynman rules can be read off the path integral. The vertices and therefore

[2] To be consistent with literature we neglect the contribution of the chemical potential.

the couplings remain the same as in the $T=0$ theory. The only difference between $T=0$ and $T\neq 0$ lies in the propagators, which are now derived from the quadratic part of the Euclidean Lagrangian in a periodic $\mathbb{R}^3\times S^1$. For example in a real scalar field theory

$$\mathcal{D}(\omega_n,\vec{k})=\frac{1}{\omega_n^2+\vec{k}^2+m^2} \tag{2.30}$$

$$p_E=(p_0,\vec{p})\rightarrow(\omega_n,\vec{p}) \tag{2.31}$$

$$\int\frac{d^4k_E}{(2\pi)^4}\rightarrow\frac{1}{\beta}\sum_n\int\frac{d^3k}{(2\pi)^3} \tag{2.32}$$

with the Matsubara frequencies ω_n, given in Eq. (2.18).

2.2 The Effective Potential

We want to investigate the electroweak symmetry breaking pattern at the electroweak phase transition. At a first sight, the classical Higgs potential dictates the behavior of the electroweak symmetry breaking, however quantum effects may change some aspects of the potential. For example a broken symmetry may be restored under radiative corrections [25]. To include such quantum corrections, the effective potential can be investigated. This effective potential, which we will see later, will give the true vacuum state at its minimum taking into account quantum corrections. Unfortunately no closed form for the effective potential exists and it has to be calculated order by order. In the following we will introduce the effective action at zero temperature, derive the effective potential and show one simple way to calculate the one-loop approximation.

2.2.1 Effective Action at zero Temperature

For simplicity, we consider a field theory with only scalar fields. The derived aspects can be generalized for all kinds of theories. For more detailed explanations, the excellent review of finite temperature field theory [5] is recommended.
The generating functional in path integral representation

$$Z[J]=\int\mathcal{D}\phi\exp\left(\mathrm{i}\int d^4x(\mathcal{L}(x)+J(x)\phi(x))\right)=\mathrm{e}^{\mathrm{i}W[J]} \tag{2.33}$$

with the generating functional for connected Greens functions $W[J]$ can be used to show that an expansion of $W[j]$ in $j(x)$ produces the connected Greens functions $\mathcal{G}^{(c)}$ [26]

$$\mathrm{i}W[j]=\sum_{n=0}^{\infty}\frac{\mathrm{i}^n}{n!}\int d^4x_1\dots d^4x_nj(x_1)\dots j(x_n)\mathcal{G}^c_{(n)}(x_1,\dots,x_n)\,. \tag{2.34}$$

In an analogous way one can expand the Legendre transformed effective action

$$\Gamma[\bar{\phi}] = W[j] - \int d^4x \bar{\phi}(x) j(x) \tag{2.35}$$

in terms of the field variable

$$\bar{\phi} = \frac{\delta W[j]}{\delta j(x)} \tag{2.36}$$

by using

$$\Gamma[\bar{\phi}] = \sum_{n=0}^{\infty} \frac{1}{n!} \int d^4x_1 \dots d^4x_n \bar{\phi}(x_1) \dots \bar{\phi}(x_n) \Gamma^{(n)}(x_1, \dots, x_n) \tag{2.37}$$

with the *one-particle-irreducible correlation functions* $\Gamma^{(n)}(x_1 \dots x_n)$. Another way to expand the effective action is done by

$$\Gamma\left[\bar{\phi}\right] = \int d^4x \left[-V_{eff}(\bar{\phi}) + \frac{1}{2}(\partial_\mu \bar{\phi})^2 Z(\bar{\phi}) + \dots \right], \tag{2.38}$$

where the *effective potential* V_{eff} is introduced. The expansion in Eq. (2.38) can be understood as an expansion in external momenta. For a translation invariant theory, the field configuration $\overline{\phi}$ is a constant field configuration in space-time

$$\overline{\phi} = \phi_{cl.} = \text{const.}. \tag{2.39}$$

This allows to reformulate Eq. (2.37) as

$$\Gamma[\phi_{cl.}] = \sum_{n=0}^{\infty} \frac{1}{n!} \phi_{cl.}^n \Gamma^{(n)}(p_i = 0) \int d^4x \,. \tag{2.40}$$

Comparing it to Eq. (2.38), while using that the field configuration is constant, we obtain a diagrammatic expression for the effective potential

$$V_{eff}(\phi_{cl.}) = -\sum_{n=0}^{\infty} \frac{1}{n!} \phi_{cl.}^n \Gamma^{(n)}(p_i = 0) \,. \tag{2.41}$$

Unfortunately, in most cases it is not possible to calculate this expression because of the summation over infinite Feynman diagrams. Therefore we need to express V_{eff} order by order. In the following we derive the first order of the effective potential. To start, an arbitrary rescaling of the Lagrangian for a single scalar field [27] is considered

$$\mathcal{L}(\phi, \partial_\mu \phi, a) = a^{-1} \mathcal{L}(\phi, \partial_\mu \phi) \,. \tag{2.42}$$

The factor a does not need to be small, in fact it can have a magnitude of order one. For convenience we take

$$a = \hbar \,. \tag{2.43}$$

Let P be the power of $\hbar$, I the number of internal lines and V the number of vertices in a given diagram. The relation of these quantities is given by

$$P = I - V \tag{2.44}$$

and can be related to the number of loops of the diagram by

$$L = I - V + 1 \tag{2.45}$$

to yield the final expression

$$P = L - 1\,. \tag{2.46}$$

According to these considerations we can conclude that a perturbative expansion in terms of loops can be directly related to an expansion in powers of $\hbar$.
The idea is now to expand the effective potential in orders of $\hbar$

$$V_{eff} = V^0 + \hbar V^{(1)} + \mathcal{O}(\hbar^2) \tag{2.47}$$

to obtain an expression for the first order loop expansion. To continue we need the action

$$S_J \equiv S + \int d^4x J(x)\phi(x) \tag{2.48}$$

with the external source term $\sim J(x)\phi(x)$. The solution of the Euler-Lagrange equation

$$\frac{\delta S_J(\phi)}{\delta\phi(x)}\Big|_{\phi=\phi_0} = 0 \tag{2.49}$$

is denoted by ϕ_0. Now an expansion of ϕ around ϕ_0 given by

$$\phi(x) = \phi_0(x) + \sqrt{\hbar}\varphi \tag{2.50}$$

can be used to expand the action around its minimum,

$$\begin{aligned} S_J(\phi) &= S_J(\phi_0 + \sqrt{\hbar}\varphi) \qquad (2.51)\\ &= S_J(\phi_0) + \frac{\hbar}{2}\int d^4x d^4y \varphi(x)\frac{\delta^2 S_J}{\delta\phi(x)\delta\phi(y)}\Big|_{\phi=\phi_0}\varphi(y) + \mathcal{O}(\hbar^2)\\ &= S_J(\phi_0) - \frac{\hbar}{2}\int d^4x \int d^4y \varphi(x)\mathcal{D}^{-1}(x,y)\varphi(y) + \cdots\,. \end{aligned}$$

In the last step we defined the inverse propagator $\mathcal{D}^{-1}(x,y)$ in the presence of a background field. Considering Eq. (2.21)

$$\begin{aligned} Z\,[J] &= \int \mathcal{D}\varphi \exp\left(\frac{\mathrm{i}}{\hbar}S_J(\phi_0 + \sqrt{\hbar}\varphi)\right) \qquad (2.52)\\ &= \int \mathcal{D}\varphi \exp\left[\frac{\mathrm{i}}{\hbar}\left(S_J(\phi_0) - \frac{\hbar}{2}\int d^4x d^4y \varphi(x)\mathcal{D}^{-1}(x,y)\varphi(y) + \mathcal{O}(\hbar^2)\right)\right]\\ &= \exp\left(\frac{i}{\hbar}S_J(\phi_0)\right)\left[\det \mathcal{D}^{-1}\right]^{-1/2}\,, \end{aligned}$$

one can write the generating functional for the connected Feynman diagrams as

$$W[J] = S_J(\phi_0) + \frac{\mathrm{i}\hbar}{2}\operatorname{Tr}\ln \mathcal{D}^{-1}\,. \tag{2.53}$$

If we neglect quantum effects and accordingly the loop expansion, the classical field configuration is simply given by the vacuum expectation value (VeV)

$$\phi_{cl.} = \frac{\delta W}{\delta J(x)} = \langle 0|\Phi(x)|0\rangle_J \ . \tag{2.54}$$

To be consistent, the solution ϕ_0 must converge in the $\hbar \to 0$ limit to the classical solution. We expand the classical field configuration in the following sense

$$\phi_{cl.}(x) = \phi_0(x) + \phi_1(x) + \mathcal{O}(\hbar^2) \tag{2.55}$$

where ϕ_1 is the dynamical field and of order $\hbar$. Finally we can write the effective action as

$$\begin{aligned}\Gamma\left[\phi_{cl.}\right] &= W\left[J\right] - \int d^4x \phi_{cl.}(x) J(x) \\ &= S^J(\phi_0) + \frac{i\hbar}{2}\operatorname{Tr}\ln\mathcal{D}^{-1} - \int d^4x(\phi_0+\phi_1)J + \mathcal{O}(\hbar^2) \\ &= S(\phi_0) + \int d^4x\phi_0 J + \frac{i\hbar}{2}\operatorname{Tr}\ln\mathcal{D}^{-1} - \int d^4x(\phi_0+\phi_1)J + \mathcal{O}(\hbar^2) \\ &= S(\phi_0) - \int d^4x\phi_1 J + \frac{i\hbar}{2}\operatorname{Tr}\ln\mathcal{D}^{-1} + \mathcal{O}(\hbar^2) \\ &= S(\phi_{cl.}) + \frac{i\hbar}{2}\operatorname{Tr}\ln\mathcal{D}^{-1} + \mathcal{O}(\hbar^2)\,.\end{aligned} \tag{2.56}$$

In the last step the classical Euler Lagrange equation is used to rewrite the action. In Eq. (2.38) we have already shown that for a constant field configuration the effective action can be related to the effective potential times the phase space Ω. Using this

$$\Gamma[\phi_{cl}] = -\Omega V_{eff}(\phi_{cl.}) = -\Omega V^0(\phi_{cl}) + \frac{\mathrm{i}\hbar}{2}\operatorname{Tr}\ln\mathcal{D}^{-1}\,, \tag{2.57}$$

allows to find a formula for the one-loop effective potential

$$V^{(1)}(\phi_{cl}) = -\frac{\mathrm{i}\hbar}{2}\Omega^{-1}\operatorname{Tr}\ln\mathcal{D}^{-1}\,. \tag{2.58}$$

Note that the inverse propagator is the propagator of the theory shifted by the constant classical field configuration. This will induce effective masses m_{eff}, which in general depend on the field value ϕ_{cl}. The Tr can be rewritten in a more convenient way in the momentum space

$$\begin{aligned}\operatorname{Tr}\ln\mathcal{D}^{-1} &= \int d^4x \left\langle x\right|\ln\mathcal{D}^{-1}\left|x\right\rangle \\ &= \int d^4x \int \frac{d^4k}{(2\pi)^4}\ln\left(-k^2+m_{eff}^2\right) \\ &= \Omega\int \frac{d^4k}{(2\pi)^4}\ln\left(-k^2+m_{eff}^2\right)\end{aligned} \tag{2.59}$$

and after the Wick rotation $k^0 \to \mathrm{i}k_4$ and the limit $\hbar = 1$, we obtain the final result for the one loop effective potential with the Euclidean momentum vector k_E at zero temperature

$$V^{(1)} = \frac{1}{2}\int \frac{d^4k_E}{(2\pi)^4}\ln\left(k_E^2+m_{eff}^2\right)\ . \tag{2.60}$$

2.2.2 The Effective Potential at Finite Temperature

The next section of this work illustrates how the one-loop effective potential at finite temperature for a single scalar field can be obtained. The thereby gained results can be generalized to an extended Higgs sector. For a more detailed discussion we refer to [24].
Let φ be a scalar field with the mass m_φ. According to Eq. (2.60), the one-loop contribution to the effective potential is given by

$$V_\varphi^{(1)} = \frac{1}{2}\int \frac{d^4k}{(2\pi)^4} \ln\left[k_\mu k_\mu + m_\varphi^2\right] \xrightarrow{T\neq 0} \frac{T}{2}\sum_n \int \frac{d^3k}{(2\pi)^3} \ln\left[\omega_n^2 + \vec{k}^2 + m_\varphi^2\right] . \tag{2.61}$$

For the next step we use a common trick [28] to calculate the *Bose sum* to reduce the problem to a three dimensional integral. We note that we can write the sum with the definition $\omega_k^2 = \vec{k}^2 + m_\varphi^2$ as

$$\sum_n^{\text{Bos}} \ln\left(\omega_n^2 + \omega_k^2\right) = \sum_n^{\text{Bos}} \ln\left(\omega_n^2 + 1/\beta^2\right) + \int_{\frac{1}{\beta}}^{\omega_k} du \sum_n^{\text{Bos}} \frac{2u}{u^2 + \omega_n^2} \tag{2.62}$$

and define

$$\nu(u) = \sum_n^{\text{Bos}} \ln\left(\omega_n^2 + u^2\right) . \tag{2.63}$$

Differentiating ν shows that

$$\frac{\partial \nu}{\partial u} = \sum_n^{\text{Bos}} \frac{2u}{\omega_n^2 + u^2} \tag{2.64}$$

and using the identity

$$\sum_{n\in\mathbb{Z}} \frac{y}{y^2 + n^2\pi^2} = \coth(y) \,, \qquad \omega_n = 2\pi n T \,, \tag{2.65}$$

one can rewrite the formula as

$$\frac{\partial \nu}{\partial u} = \beta \left(1 + 2\frac{1}{\mathrm{e}^{\beta u} - 1}\right) . \tag{2.66}$$

Bearing this in mind, the sum can be calculated as follows

$$\begin{aligned}
\sum_n^{\text{Bose}} \ln\left(\omega_n^2 + \omega_k^2\right) &= \sum_n^{\text{Bose}} \ln\left(\omega_n^2 + 1/\beta\right) + \int_{\frac{1}{\beta}}^{\omega_k} du \beta \left(1 + 2\frac{1}{\mathrm{e}^{\beta u} - 1}\right) \\
&= \sum_n^{\text{Bose}} \ln\left(\omega_n^2 + 1/\beta\right) + \beta\omega_k + 2\ln\left(1 - \mathrm{e}^{-\beta\omega_k}\right) + (\omega_k\text{-independent const.}) \\
&= \beta\omega_k + 2\ln\left(1 - \mathrm{e}^{-\beta\omega_k}\right) + (\omega_k\text{-independent const.}) \,.
\end{aligned} \tag{2.67}$$

In this step a typical phenomenon that occurs while evaluating such Bose sums can be seen. The integral is split in two parts, one temperature independent and temperature dependent part,

$$V_\varphi^{(1)} = \int \frac{d^3k}{(2\pi)^3} \frac{\omega_k}{2} + \int \frac{d^3k}{(2\pi)^3} \frac{1}{\beta} \ln\left(1 - \mathrm{e}^{-\beta\omega_k}\right) + (\omega_k\text{-independent const.}) \,. \tag{2.68}$$

The temperature independent part is called Coleman-Weinberg contribution V_{CW}. It is UV divergent and must be renormalized. This is done by using the $\overline{\mathrm{MS}}$ scheme and the fact that

$$\omega_k = \sqrt{\vec{k}^2 + m_\varphi^2} = \lim_{\epsilon\to 0} \frac{-\mathrm{i}}{2\pi} \int_{-\infty}^{\infty} dk_0 \ln\left(-k_0^2 + \vec{k}^2 + m_\varphi^2 - \mathrm{i}\epsilon\right) . \tag{2.69}$$

This allows to rewrite V_{CW} in the Minkowski metric and using the common calculation to renormalise this term. One obtains [29]

$$V_{CW}^{\overline{MS}} = \frac{m_\varphi^4}{64\pi^2}\left(\ln\left(\frac{m_\varphi^2}{\mu^2}\right) - \frac{3}{2}\right) \tag{2.70}$$

where μ is the mass scale introduced in the $\overline{MS}$ scheme. It is convenient to write the temperature dependent part as

$$V_T = \int \frac{d^3k}{(2\pi)^3}\frac{1}{\beta}\ln\left(1 - \mathrm{e}^{-\beta\omega_k}\right) = \frac{1}{2\pi^2\beta^4} J_B[m_\varphi^2\beta^2] \tag{2.71}$$

with the thermal bosonic function J_B defined as

$$J_B[m^2\beta^2] = \int_0^\infty dx\, x^2 \ln\left[1 - \exp(\sqrt{x^2 + \beta^2 m^2})\right] . \tag{2.72}$$

For a complete description of an extended Higgs sector one needs to calculate the contribution of the vector bosons and fermions to the effective potential. Because there is nothing special new, only subtleties, we refer to the literature and give only the result:

$$V_{eff}^{(1)} = V_{tree} + V^1 \equiv V_{tree} + V_{CW} + V_T\,, \tag{2.73}$$

with V_{tree} as the tree level potential and the Coleman-Weinberg contribution

$$V_{CW} = \sum_i \frac{n_i}{64\pi^2}(-1)^{2s_i} m_i^4 \left[\ln\left(\frac{m_i^2}{\mu^2}\right) - c_i\right] , \tag{2.74}$$

where the sum is over all particles in the theory, n_i are the number of degrees of freedom, s_i the spin, m_i the mass of the particle i, μ is the scale of the electroweak symmetry breaking and c_i is the renormalization constant of the $\overline{\mathrm{MS}}$ scheme, which is given by

$$c_i = \begin{cases} \frac{5}{6}, & i = W^\pm, Z, \gamma \\ \frac{3}{2}, & \text{otherwise} \end{cases} . \tag{2.75}$$

The temperature dependent part reads

$$V_T = \sum_i n_i \frac{T^4}{2\pi^2} J_\pm^{(i)}\,, \tag{2.76}$$

with the thermal bosonic J_- and the fermionic J_+ function

$$J_\pm[m^2/T^2] = \mp \int_0^\infty dx\, x^2 \ln\left[1 \pm \exp(\sqrt{x^2 + m^2/T^2})\right] . \tag{2.77}$$

Using Eq. (2.77) for numerical calculations would be very time consuming so that in this work we use a high and low temperature expansion instead of this quantity. We follow [14] and use for small $x^2 \equiv m^2/T^2$

$$J_+(x^2, n) = -\frac{7\pi^4}{360} + \frac{\pi^2}{24}x^2 + \frac{1}{32}x^4(\log x^2 - c_+) \tag{2.78}$$
$$- \pi^2 x^2 \sum_{l=2}^{n} \left(-\frac{1}{4\pi^2}x^2\right)^l \frac{(2l-3)!!\zeta(2l-1)}{(2l)!!(l+1)} \left(2^{2l-1} - 1\right) ,$$
$$J_-(x^2, n) = -\frac{\pi^4}{45} + \frac{\pi^2}{12}x^2 - \frac{\pi}{6}(x^2)^{3/2} - \frac{1}{32}x^4(\log x^2 - c_-) \tag{2.79}$$
$$+ \pi^2 x^2 \sum_{l=2}^{n} \left(-\frac{1}{4\pi^2}x^2\right)^l \frac{(2l-3)!!\zeta(2l-1)}{(2l)!!(l+1)} ,$$

with

$$c_+ = 3/2 + 2\log\pi - 2\gamma_E \quad \text{and} \quad c_- = c_+ + 2\log 4 , \tag{2.80}$$

where γ_E denotes the Euler-Mascheroni constant, $\zeta(x)$ the Riemann ζ-function and $n!!$ the double factorial. For the low temperature limit (large x^2) we use

$$J_\pm(x^2, n) = -\exp(-(x^2)^{1/2}) \left(\frac{\pi}{2}(x^2)^{3/2}\right)^{1/2} \sum_{l=0}^{n} \frac{1}{2^l l!} \frac{\Gamma(5/2+l}{5/2-l}(x^2)^{-l/2} , \tag{2.81}$$

with the Euler-Gamma function $\Gamma(x)$. To have a continuous transition between both approximations, we first determine the point where the derivatives can be continuously connected and afterwards we add a small finite shift to the small x^2 expansion. In this way both approximations are connected continuously. The point of the transition $x_\pm$ and the shift $\delta_\pm$ reads [14]

$$x_+^2 = 2.2161 , \qquad \delta_+ = -0.015603 , \tag{2.82}$$
$$x_-^2 = 9.4692 , \qquad \delta_- = 0.0063109 , \tag{2.83}$$

where $+(-)$ refers to the fermionic (bosonic) approximation. In order to achieve a two percent agreement of the approximation to the numerical evaluation of the integral in Eq. (2.77), we include terms of up to order $n = 4$ in J_+ and $n = 3$ in J_- in the small x^2 approximation. In the large x^2 approximation both types $J_\pm$ are in the two percent range by including terms of up to order $n = 3$.

2.3 Resummation in Hot Field Theory

Our aim is to examine how the temperature affects the perturbative expansion of the quantum field theory and how additional contributions induced by hard thermal loops can be controlled. Therefore this chapter at first addresses the real scalar field theory in order to point out explicit problems in the usual self-coupling expansion. Then the so called Debye-corrections or daisy resummation are introduced and finally the resummation prescription used in this work will be discussed.

2.3.1 The Real Scalar Field

Starting with the Lagrangian for a real scalar field ϕ,

$$\mathcal{L} = \frac{1}{2}(\partial_\mu \phi)^2 + \frac{\mu}{2}\phi^2 - \frac{\lambda}{4}\phi^4 \,, \tag{2.84}$$

we perform the spontaneous symmetry breaking

$$\phi = v + \chi \,, \tag{2.85}$$

where v is the VeV and χ the dynamical field. The tree level minimum is simply given by

$$\langle v \rangle_{tree} = \frac{\mu}{\lambda^{1/2}} \tag{2.86}$$

and the tree level mass of the field χ is

$$m^2(v) = 3\lambda v^2 - \mu^2 \,. \tag{2.87}$$

To go beyond the tree level, we need to calculate the effective potential. This will allow us to gain an insight into the next-to-leading order. Considering finite temperature, the only temperature dependent part of the effective potential is V_T given in Eq. (2.71). For simplicity, we take the high temperature limit of the integral in Eq. (2.78). For the leading contribution this results in [30]

$$V_T(v) = T^4 \left[\frac{-\pi^2}{90} + \frac{m^2(v)}{24T^2} - \frac{m^3(v)}{12\pi T^3} + \mathcal{O}(m^4/T^4) \right] . \tag{2.88}$$

Note that $m^2 \sim \lambda$ and therefore the next-leading order in λ is not λ^2 as one would expect, but $\sim \lambda^{3/2}$. Considering higher order contributions, we need to take into account contributions of order $\lambda^{3/2}$. It was shown in [6] that this order is given by the *ring corrections* which corresponds to the Debye corrections.
Unfortunately, as shown in [5], the perturbative expansion breaks down at the phase transition at one-loop approximation, and in addition one suffers from infrared divergencies caused by the Matsubara zero modes ($n = 0$) of the bosons

$$V_{eff} \sim \ln(\mathcal{D}^{-1}) \xrightarrow{\vec{p}\to 0} \infty \,. \tag{2.89}$$

We therefore need to include the dominant next-to-leading contributions, the ring corrections. These corrections can be obtained as first-order corrections to the mean-field result at one-loop, which is simply a self energy correction in the infrared limit and *hard thermal loop approximation* [24]. This limit implies that loop momenta and masses are small compared to the temperature scale.

Our next point of interest is the calculation of the one-loop corrections to the polarization tensor of the scalar field. The needed diagram is shown in Fig. 2.1. Defining $\omega_k^2 = \vec{k}^2 + m^2$ leads to

$$\pi^{(1)}(\omega_n, \vec{k}) = \pi^{(1)}(0) = 3\lambda T \sum_n \int \frac{d^3k}{(2\pi)^3} \frac{1}{\omega_n^2 + \omega_k^2} \tag{2.90}$$

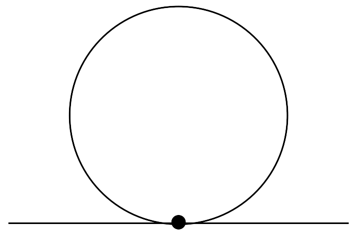

Figure 2.1: One-loop contribution to the polarization tensor of the scalar field.

$$
\begin{aligned}
&= 3\lambda T \int \frac{d^3k}{(2\pi)^3} \frac{1}{2\omega_k} \frac{d}{d\omega_k} \sum_n \ln\left(\omega_n^2 + \omega_k^2\right) \\
&= 3\lambda \left[\int \frac{d^3k}{(2\pi)^3} \frac{1}{2\omega_k} + \int \frac{d^3k}{(2\pi)^3} \frac{1}{\omega_k(\mathrm{e}^{\beta\omega_k} - 1)} \right]
\end{aligned} \tag{2.91}
$$

where we used Eq. (2.67) to perform the summation. The first term can be dropped due to the UV regularisation and the second will give in the limit $m/T \ll 1$

$$
\pi^{(1)}(0) = \lambda \frac{3T^2}{12} \,. \tag{2.92}
$$

This limit is sufficient because in [6] it was demonstrated that the ring corrections are small unless $m/T \ll 1$; therefore we can use the *hard thermal approximation* of Eq. (2.92). If the dominant two loop contribution, the ring corrections, shall be considered, the resummed polarization tensor has to be taken into account. This is equivalent to the replacement of the bare mass with the thermal mass in the propagator

$$
m_0 \to \overline{m} = m_0 + \pi^{(1)}(0) \,. \tag{2.93}
$$

The diagrammatic approach can be seen in Fig. 2.2. On the left side we see the dominant two-loop contributions given by the hard thermal loops with $m/T \ll 1$ and on the right side we see the resummed propagator. The resummed propagator can be obtained by replacing the tree level mass by its thermal mass in the propagator. In [31] it is shown that the replacement of the thermal mass will indeed produce an additional cubic mass term in the V_T potential and therefore it is of the requested order of $\lambda^{3/2}$. In [32] it is suggested to replace all masses by their thermal masses, an approach we will further on refer to as *Parwani method*. This method admixes higher-order contributions which at one-loop level could lead to a non consistent description of the expansion. Another approach is provided in [33]. Here the different Matsubara modes, namely the heavy ($n \neq 0$) and zero ($n = 0$) modes, are handled independently. The motivation behind this approach can be seen in the one-loop integral $I(m)$ in $d = 4 - 2\epsilon$ dimensions if the different Matsubara modes are splitted in the zero and heavy modes

$$
I(m) = I_0 + I_{n\neq 0} \,. \tag{2.94}
$$

The zero mode part reads

$$
I_0 = \mu^{2\varepsilon} T \int \frac{d^{3-2\varepsilon}}{(2\pi)^{3-2\varepsilon}} \frac{1}{k^2 + m^2} = \frac{\Gamma\left(-1/2 + \epsilon\right)}{(4\pi)^{3/2}} \left[\frac{4\pi\mu^2}{m^2}\right]^{\varepsilon} mT \xrightarrow{\varepsilon \to 0} -\frac{1}{4\pi} mT \tag{2.95}
$$

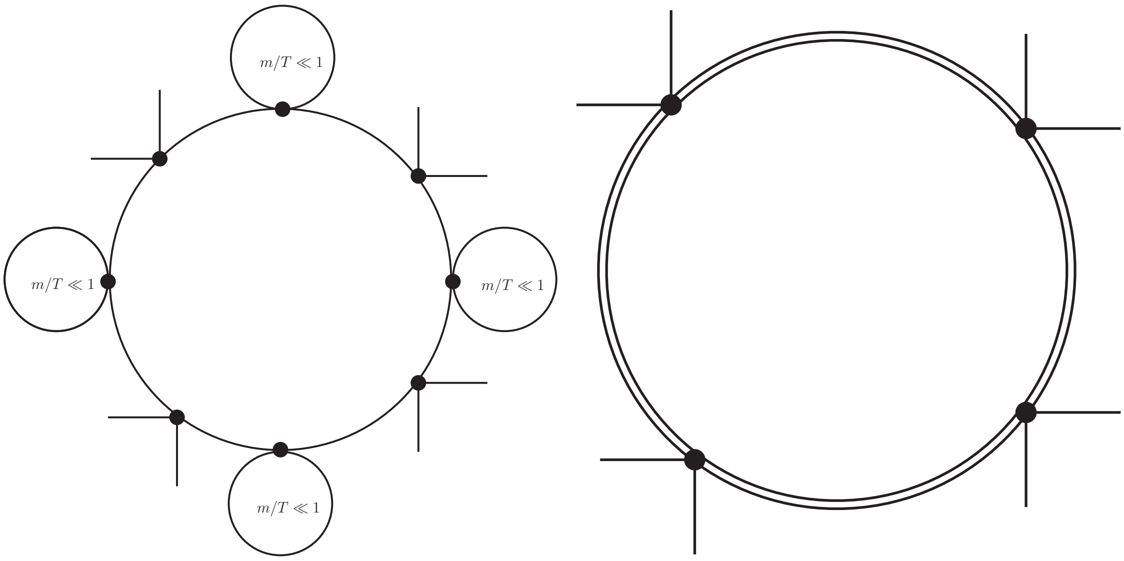

(a)

(b)

Figure 2.2: Diagrammatical approach to the one-loop effective potential. On the left side the dominant two loop contribution with hard thermal loops, the so called ring diagrams. On the right side the resummed effective potential with thermal masses.

and the heavy modes can be evaluated to

$$
\begin{aligned}
I_{n\neq 0} &= 2\mu^{2\varepsilon} T \sum_{n=1}^{\infty} \int \frac{d^{3-2\varepsilon}}{(2\pi)^{3-2\varepsilon}} \frac{1}{(2\pi n T)^2 + k^2 + m^2} \\
&= 2\mu^{2\varepsilon} T \sum_{n=1}^{\infty} \sum_{l=0}^{\infty} \int \frac{d^{3-2\varepsilon}}{(2\pi)^{3-2\varepsilon}} \frac{(-1)^l m^{2l}}{[(2\pi n T)^2 + k^2]^{l+1}} \\
&= \frac{1}{12} T^2 - \frac{1}{16\pi^2} m^2 \left[\frac{1}{\varepsilon} + \ln(\frac{\mu^2}{T^2}) - 2c_b \right] \\
&\quad + T^2 \sum_{l=2}^{\infty} \left(\frac{-m^2}{4\pi^2 T^2} \right)^l \frac{(2l-3)!!}{(2l)!!} \zeta(2l-1) + \mathcal{O}(\varepsilon)\,.
\end{aligned}
\tag{2.96}
$$

The heavy modes can be treated as a perturbative expansion in m^2, while the zero mode breaks this expansion due to the factor[3] $\sim m$. Therefore it is suggested in [33] to only resum the static zero modes of the theory and not mix different orders. In a generic framework with an arbitrary scalar sector and an SM Yukawa sector and gauge symmetries, this method results in a replacement within the thermal integral expression as follows,

$$
J_{\pm}^{(k)} = \begin{cases} J_-(\frac{m_k^2}{T^2}) - \frac{\pi}{6}\left(\overline{m}_k^3/T^3 - m_k^3/T^3\right), & k = W_L, Z_L, \gamma_L, \Phi^0, \Phi^{\pm} \\ J_-(\frac{m_k^2}{T^2}) & k = W_T, Z_T, \gamma_T \\ J_+(\frac{m_k^2}{T^2}) & k = \text{fermion}\,. \end{cases}
\tag{2.97}
$$

[3]Note that $m^2 \sim \lambda$ and therefore an expansion in m^2 corresponds to the expansion in the self-coupling λ.

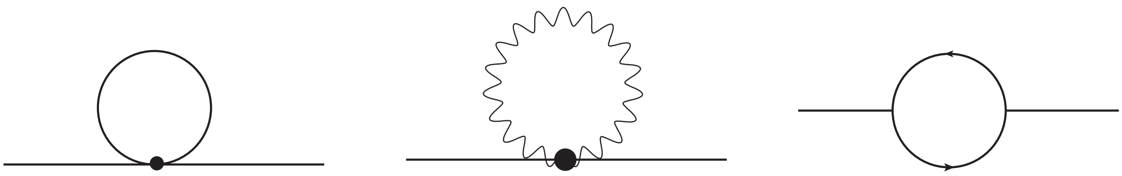

(a) $\Pi_{ij}^{(S)}$ (b) $\Pi_{ij}^{(V)}$ (c) $\Pi_{ij}^{(F)}$

Figure 2.3: The three different contributions to the Higgs polarization tensor at one-loop level with the external legs i and j.

W_L, Z_L and γ_L are the longitudinal modes of the $\mathrm{SU}(2) \times U(1)$ gauge bosons, respectively, T denotes the transversal modes. Φ^0 denotes neutral scalars and $\Phi^\pm$ charged scalars. We refer to this method as *Arnold Espinosa* method. Although some instabilities were observed in the phase transition while using this method, we still consider this method to be more consistent. In addition to that it also allows for a comparison to the existing literature on this subject.

2.3.2 Thermal Masses

In the following we want to calculate the thermally corrected masses of the Higgs and gauge bosons in a generic framework. The thermal masses are required by the Eq. (2.97). As a first step the polarisation tensors of the corresponding fields are needed in order to calculate the thermal mass corrections. Suppose we have a Higgs sector with N additional scalar degrees of freedom and a gauge and fermion sector like in the SM. The Higgs sector is described by a potential V. The three different diagram types for the Higgs corrections are shown in Fig. 2.3. We compute the Higgs polarization tensor in the gauge basis and label the involved Higgs fields in the gauge basis with the indices i, j, k, which each run from 1 to N. The first diagram (2.3a) can then be written as

$$\Pi_{ij}^{(S)} = \sum_{k=1}^{N} \Pi_{ij}^{k} = \sum_{k=1}^{N} \kappa_{ij}^{k} \sum\!\!\!\!\!\!\!\int_P \frac{1}{\omega_n^2 + \vec{p}^{\,2}}\,, \tag{2.98}$$

where we introduced the shorthand notation

$$\sum\!\!\!\!\!\!\!\int_P \equiv \frac{1}{\beta} \sum_n \int \frac{d^3p}{(2\pi)^3} \tag{2.99}$$

and

$$\kappa_{ij}^{k} = -\frac{1}{2} \frac{\partial^4 V}{\partial_{\phi_i} \partial_{\phi_j} \partial_{\phi_k}^2} \tag{2.100}$$

for the quartic couplings. Note that the symmetry factor is already absorbed in κ_{ij}^k. In a complete analogous way to Eq. (2.92) one can compute Eq. (2.98) yielding

$$\Pi_{ij}^{(S)} = \kappa_{ij}^{k} \frac{T^2}{12}\,. \tag{2.101}$$

The gauge boson contribution, shown in Fig. 2.3b, to the Higgs polarisation tensor can be written as ($a = 1, 2, 3$)

$$\Pi_{ij}^{(V)} = \sum_a \Pi_{ij}^{W_\mu^a} + \Pi_{ij}^{B_\mu} \,. \tag{2.102}$$

Defining the involved quartic coupling as

$$\kappa_{ij}^{V} = \frac{1}{2} \frac{\partial^4 \mathcal{L}}{\partial_i \partial_j \partial_V^2} \,, \tag{2.103}$$

where $\partial_V \equiv \frac{\partial}{\partial W_\mu^a}$ or $\partial_V \equiv \frac{\partial}{\partial B_\mu}$, the calculation of the diagram results in[4]

$$\begin{aligned}\Pi_{ij}^{(V)} =& \kappa_{ij}^{V} T \sum_n \int \frac{d^3p}{(2\pi)^3} \frac{\delta_{\mu\nu}}{\omega_n^2 + \vec{p}^2} \left(\delta_{\nu\mu} - \frac{p_\mu p_\nu}{\omega_n^2 + \vec{p}^2} \right) \\ =& \kappa_{ij}^{V} T \sum_n \int \frac{d^3p}{(2\pi)^3} \frac{1}{\omega_n^2 + \vec{p}^2} \left(4 - \frac{\omega_n^2 + \vec{p}^2}{\omega_n^2 + \vec{p}^2} \right) \\ =& 3\kappa_{ij}^{V} T \sum_n \int \frac{d^3p}{(2\pi)^3} \frac{1}{\omega_n^2 + \vec{p}^2} \\ =& \kappa_{ij}^{V} \frac{T^2}{4} \,. \end{aligned} \tag{2.104}$$

For the fermion contribution, depicted in Fig. 2.3c and denoted as $\Pi^{(F)}$, we consider only the top and bottom contribution because of the small Yukawa couplings of the other quarks. The general form of the fermion contribution $\Pi^{(F)}$ depends on the assumptions of the model. Hence, we only show the explicit expression $\Pi^{(F)}$ for the N2HDM later on. The full Higgs polarisation tensor is the sum of all contributions

$$\Pi_{ij}^{(H)} = \Pi_{ij}^{(S)} + \Pi_{ij}^{(V)} + \Pi_{ij}^{(F)} \,. \tag{2.105}$$

The daisy resummed propagator is equivalent to the replacement of the bare masses with the thermal masses which are the eigenvalues of the thermally corrected mass matrix

$$\overline{M} = M_0 + \delta M_T \equiv M_0 - \Pi^{(H)} \,. \tag{2.106}$$

The leading-order mass matrix M_0 can be obtained by the second derivative of the Higgs potential with respect to the fields in the gauge basis.

[4] Note that we use the Landau gauge, which is considered as the most *elegant* way to calculate the effective potential, because in this gauge the ghost contribution drops out. There remains the open question of the gauge dependence of the effective potential. For discussions of this issue, see e.g. [34–37].

CHAPTER 3

The N2HDM

In the following chapter we will introduce the notation used in this thesis and the N2HDM. We will calculate the mass spectrum and introduce the different types of the model. Afterwards we will present the results obtained by applying the formulas introduced in Chapter 2, including the VeV configuration used in the analysis, the effective couplings needed for the Debye corrections and the thermal masses.

3.1 The N2HDM Higgs Sector

The N2HDM consists of a CP-conserving two Higgs Doublet model (2HDM) with a softly broken $\mathbb{Z}_2$ symmetry extended by a real singlet field S. The extension of a 2HDM by a real scalar singlet which does not obtain a VeV and in this way providing a stable dark matter (DM) candidate is discussed in [38–49]. A scenario with a finite singlet VeV but with certain approximations is given in [50]. In this work we investigate the most general N2HDM introduced in [51]. An additional singlet S under the gauge group $\mathrm{SU}(2)_L \times \mathrm{U}_Y$ is added to the CP-conserving 2HDM Lagrangian. To reduce the number of free parameters in the model, we take a real singlet and apply an additional $\mathbb{Z}_2'$ symmetry, so that

$$S \to -S \tag{3.1}$$

is a symmetry of the Lagrangian. The Lagrangian reads as follows:

$$\mathcal{L}^{N2HDM} = (D^\mu \Phi_1)^\dagger (D_\mu \Phi_1) + (D^\mu \Phi_2)^\dagger (D_\mu \Phi_2) + (\partial_\mu S)^2 - \mathrm{V}\,, \tag{3.2}$$

with the two Higgs doublets Φ_1, Φ_2 and the covariant derivative D^μ in terms of the gauge couplings g, g' corresponding to the $\mathrm{SU}(2)_L \times \mathrm{U}(1)_Y$ gauge group,

$$D^\mu = \partial^\mu + i\frac{g}{2}\sigma_a W^{\mu,a} + i\frac{g'}{2}B^\mu, \quad a = 1,2,3\,, \tag{3.3}$$

where σ_a stands for the Pauli matrices and the $\mathrm{SU}(2)\times U(1)$ gauge fields are given by B_μ and $W^{\mu,a}$. The Higgs potential is given by the real CP-conserving softly broken $\mathbb{Z}_2$ symmetric 2HDM potential plus a real singlet potential [51]

$$
\begin{aligned}
V = {} & m_{11}^2\Phi_1^\dagger\Phi_1 + m_{22}^2\Phi_2^\dagger\Phi_2 - m_{12}^2\left(\Phi_1^\dagger\Phi_2 + \text{h.c.}\right) + \frac{\lambda_1}{2}\left(\Phi_1^\dagger\Phi_1\right)^2 + \frac{\lambda_2}{2}\left(\Phi_2^\dagger\Phi_2\right)^2 \\
& + \lambda_3\Phi_1^\dagger\Phi_1\Phi_2^\dagger\Phi_2 + \lambda_4\Phi_1^\dagger\Phi_2\Phi_2^\dagger\Phi_1 + \frac{\lambda_5}{2}\left((\Phi_1^\dagger\Phi_2)^2 + \text{h.c.}\right) \\
& + \frac{1}{2}m_S^2 S^2 + \frac{\lambda_6}{8}S^4 + \lambda_7\left(\Phi_1^\dagger\Phi_1\right)S^2 + \lambda_8\left(\Phi_2^\dagger\Phi_2\right)S^2\,,
\end{aligned}
\tag{3.4}
$$

where the mass parameters m_{11}, m_{22}, m_{12} and m_S as well the coupling parameters $\lambda_1 \dots \lambda_8$ are real due to the required CP-conservation. To prevent flavour changing neutral currents (FCNC) another $\mathbb{Z}_2$ symmetry for the Higgs doublets [52] is introduced,

$$\Phi_1 \to \Phi_1\,, \quad \Phi_2 \to -\Phi_2\,. \tag{3.5}$$

This symmetry is softly broken by the m_{12}^2 term and can be extended to the Yukawa sector. Since we are considering a CP-conserving model, the VeVs v_1, v_2 and v_S that can be acquired by the neutral components of the Higgs doublets and singlet, must also be real. We can then express the Higgs doublets in terms of the real component fields of the charged fields, $\xi_{1,2}$ and $\chi_{1,2}$, respectively, the neutral CP-even and CP-odd fields, $\rho_{1,2,S}$ and $\eta_{1,2}$, respectively,

$$\Phi_1 = \frac{1}{\sqrt{2}}\begin{pmatrix} \xi_1 + i\chi_1 \\ v_1 + \rho_1 + i\eta_1 \end{pmatrix}, \qquad \Phi_2 = \frac{1}{\sqrt{2}}\begin{pmatrix} \xi_2 + i\chi_2 \\ v_2 + \rho_2 + i\eta_2 \end{pmatrix}, \tag{3.6}$$

$$S = v_S + \rho_S\,. \tag{3.7}$$

For later use, we call the field basis

$$\mathrm{B}_{gauge} = \{\xi_1, \xi_2, \chi_1, \chi_2, \eta_1, \eta_2, \rho_1, \rho_2, \rho_S\} \tag{3.8}$$

the gauge basis and the corresponding mass eigenstates the physical basis.
There are three different vacuum configurations. The *normal vacuum* has no CP and no charge breaking (CB) components. In the *charge breaking* vacuum, the field ξ_2 obtains a non-zero VeV. In the CP-breaking vacuum the CP-odd neutral component of the neutral field, ρ_2, acquires a VeV. For the 2HDM, it has been proven, that the normal vacuum, if it exists, is always the global minimum [53]. This does not generalize to the N2HDM, however. For a counterexample for a deeper CP and CB vacuum, we refer to [51]. In the following we investigate the diagonalisation of the Higgs sector at zero temperature and for vanishing CP- and charge breaking VeVs so that the VeV configuration reads

$$\langle\Phi_1\rangle\big|_{T=0} = \frac{1}{\sqrt{2}}\begin{pmatrix} 0 \\ v_1 \end{pmatrix}, \qquad \langle\Phi_2\rangle\big|_{T=0} = \frac{1}{\sqrt{2}}\begin{pmatrix} 0 \\ v_2 \end{pmatrix}, \qquad \langle S\rangle\big|_{T=0} = v_S\,. \tag{3.9}$$

The minimum conditions of the potential read

$$\frac{\partial V}{\partial v_i}\Big|_{\langle \Phi_i \rangle} = 0, \quad i = 1, 2, S\,, \tag{3.10}$$

where the brackets denote the VeV configuration in Eq. (3.9), lead to the following relations

$$\frac{v_2}{v_1} m_{12}^2 - m_{11}^2 = \frac{1}{2}\left(v_1^2 \lambda_1 + v_2^2 \lambda_{345} + v_S^2 \lambda_7\right)\,, \tag{3.11a}$$

$$\frac{v_1}{v_2} m_{12}^2 - m_{22}^2 = \frac{1}{2}\left(v_1^2 \lambda_{345} + v_2^2 \lambda_2 + v_S^2 \lambda_8\right)\,, \tag{3.11b}$$

$$-m_S^2 = \frac{1}{2}\left(v_1^2 \lambda_7 + v_2^2 \lambda_8 + v_S^2 \lambda_6\right)\,, \tag{3.11c}$$

with the shorthand notation $\lambda_{345} = \lambda_3 + \lambda_4 + \lambda_5$. These relations can be used to express the parameters m_{11}^2, m_{22}^2 and m_S^2 in terms of v_1, v_2 and the self-couplings $\lambda_1 \ldots \lambda_8$. Using the parametrisations for the Higgs doublets and the singlet given by Eq. (3.6) and Eq. (3.7) in the potential, the mass matrix can be obtained from the second derivative with respect to the fields in the gauge basis. Due to the CP and charge conservation, the 9×9 mass matrix splits into three blocks, a 4×4 block for the charged fields, a 2×2 block for the neutral CP-odd fields and a 3×3 block for the neutral CP-even fields. The charged and CP-odd sector do not differ from the 2HDM case, because the singlet does not mix with the charged nor the CP-odd fields. Like in the 2HDM, we introduce the rotation matrix

$$R_\beta = \begin{pmatrix} \cos\beta & \sin\beta \\ -\sin\beta & \cos\beta \end{pmatrix}\,, \tag{3.12}$$

with

$$\tan\beta = \frac{v_2}{v_1} \tag{3.13}$$

to diagonalize the charged and pseudoscalar sector. The charged sector reads

$$\begin{pmatrix} G^\pm \\ H^\pm \end{pmatrix} = R_\beta \frac{1}{\sqrt{2}} \begin{pmatrix} \xi_1 \pm i\chi_1 \\ \xi_2 \pm i\chi_2 \end{pmatrix} \tag{3.14}$$

with the charged massless Goldstone boson $G^\pm$ and the charged Higgs boson $H^\pm$, respectively, the pseudoscalar sector

$$\begin{pmatrix} G^0 \\ A \end{pmatrix} = R_\beta \begin{pmatrix} \eta_1 \\ \eta_2 \end{pmatrix}\,, \tag{3.15}$$

with the neutral massless Goldstone boson G^0 and the pseudoscalar A. The remaining 3×3 submatrix M^2_{scalar} for the CP-even scalar sector reads

$$M^2_{scalar} = \begin{pmatrix} v^2\lambda_1 c_\beta^2 + m_{12} t_\beta & v^2 \lambda_{345} c_\beta s_\beta - m_{12} & v v_S \lambda_7 c_\beta \\ v^2 \lambda_{345} c_\beta s_\beta - m_{12} & v^2 \lambda_2 s_\beta^2 + m_{12} c t_\beta & v v_S \lambda_8 s_\beta \\ v v_S \lambda_7 c_\beta & v v_S \lambda_8 s_\beta & v_S^2 \lambda_6 \end{pmatrix} \tag{3.16}$$

in which we already used Eqs. (3.11) to trade the mass terms m_{11}, m_{22}, m_{12} for v, v_S and $\tan\beta$. We furthermore used $v = \sqrt{v_1^2 + v_2^2}$ and introduced the short-hand notation $\sin\beta = s_\beta$, $\cos\beta = c_\beta$, $\tan\beta = t_\beta$, $\cot\beta = ct_\beta$. Introducing the mixing angles α_1, α_2, α_3

$$-\frac{\pi}{2} \leq \alpha_{1,2,3} < \frac{\pi}{2} \tag{3.17}$$

and the rotation matrix

$$R = \begin{pmatrix} c_{\alpha_1} c_{\alpha_2} & s_{\alpha_1} c_{\alpha_2} & s_{\alpha_2} \\ -\left(c_{\alpha_1} s_{\alpha_2} s_{\alpha_3} + s_{\alpha_1} c_{\alpha_3}\right) & c_{\alpha_1} c_{\alpha_3} - s_{\alpha_1} s_{\alpha_2} s_{\alpha_3} & c_{\alpha_2} s_{\alpha_3} \\ -c_{\alpha_1} s_{\alpha_2} c_{\alpha_3} + s_{\alpha_1} s_{\alpha_3} & -\left(c_{\alpha_1} s_{\alpha_3} + s_{\alpha_1} s_{\alpha_2} c_{\alpha_3}\right) & c_{\alpha_2} c_{\alpha_3} \end{pmatrix} \tag{3.18}$$

allows for the diagonalisation of M^2_{scalar}, yielding the three mass eigenstates H_1, H_2, H_3,

$$\begin{pmatrix} H_1 \\ H_2 \\ H_3 \end{pmatrix} = R \begin{pmatrix} \rho_1 \\ \rho_2 \\ \rho_S \end{pmatrix} \tag{3.19}$$

with the mass eigenvalues

$$R M^2_{scalar} R^T = \mathrm{diag}(m^2_{H_1}, m^2_{H_2}, m^2_{H_3})\,. \tag{3.20}$$

We define the mixing angles in a way that we have the mass hierarchy

$$m_{H_1} \leq m_{H_2} \leq m_{H_3}\,. \tag{3.21}$$

To summarize the Higgs sector, we have 12 free parameters and seven physical Higgs bosons in total. The free parameters are chosen such that we have as many physical parameters as possible. The Lagrangian parameters $m^2_{11}, m^2_{22}, m^2_S, \lambda_{1\ldots8}$ and m^2_{12} can be expressed in the *physical basis* $v, v_S, \tan\beta, m_{H_{1\ldots3}}, m_A, m_{H^\pm}, \alpha_{1\ldots3}$ and m^2_{12} by using the minimum conditions in Eq. (3.11). We use the physical basis in our analysis.
By imposing the $\mathbb{Z}_2$ symmetry in Eq. (3.5) four different types of the model that are summarised in Table 3.1 are possible. A complete introduction of all required couplings, Feynman rules and a phenomenological discussion of the N2HDM is given in [51].

3.2 The Effective Potential in the N2HDM

In this section we will present the results obtained by applying the formulas introduced in Chapter 2 to the N2HDM. At first we need to comment on the VeV configuration defined in Eq. (3.9). As mentioned in the introduction of the N2HDM, normal electroweak vacua are always the global minimum of the potential in a 2HDM. This statements only holds for leading-order calculations. By considering the effective potential at one-loop approximation, we include next-to-leading order (NLO) effects. This can affect the stability of the vacuum so that it is reasonable to allow for a CP or even for a charge breaking vacuum to evolve. In addition we consider

	u-type	d-type	leptons	Q	u_R	d_R	L	l_R
Type I	Φ_2	Φ_2	Φ_2	+	-	-	+	-
Type II	Φ_2	Φ_1	Φ_1	+	-	+	+	-
lepton-specific	Φ_2	Φ_2	Φ_1	+	-	+	+	-
flipped	Φ_2	Φ_1	Φ_2	+	-	-	+	+

Table 3.1: The left column shows to which corresponding quark type the Higgs doublet is coupled. To force this specific coupling, a $\mathbb{Z}_2$ symmetry has to be enforced on the quark multiplet. The right column shows which $\mathbb{Z}_2$ parity is assigned for the fermions. Q and L are the quark and lepton doublet, u_R the up-type quark singlet, d_R the down-type singlet and l_R the lepton singlet. All fields, except for S, are even under the $\mathbb{Z}_2'$ symmetry.

finite temperatures which can in principle also affect the stability of the vacuum. We denote the VeVs at finite temperature by ω_i and require

$$\omega_i\Big|_{T=0} = v_i\,, \quad i = 1, 2, S\,. \tag{3.22}$$

For these reasons, we consider the following more general VeV configuration in our analysis in order to quantify the stability of the normal electroweak vacuum,

$$\langle\Phi_1\rangle_T = \frac{1}{\sqrt{2}}\begin{pmatrix} 0 \\ \omega_1 \end{pmatrix}, \qquad \langle\Phi_2\rangle_T = \frac{1}{\sqrt{2}}\begin{pmatrix} \omega_{CB} \\ \omega_2 + i\omega_{CP} \end{pmatrix}, \tag{3.23}$$

$$\langle S\rangle_T = \omega_S\,, \tag{3.24}$$

where $\langle\varphi\rangle_T$ indicates the vacuum expectation value of φ at the temperature T. ω_1, ω_2 and ω_S correspond to the v_1, v_2 and v_S introduced in Eq. (3.6), respectively, ω_{CP} and ω_{CB} denote the contribution of the CP-violating and charge breaking VeV, see Eq. (3.22).

In the N2HDM, there are neutral scalars $\Phi^0 = H_1, H_2, H_3, A, G^0$ and charged scalars $\Phi^\pm = H^+, H^-, G^+, G^-$, leptons l^+,l^-, quarks $q, \bar{q}$ and longitudinal and transversal gauge bosons $V_L = Z_L, W_L^+, W_L^-, \gamma_L$ and $V_T = Z_T, W_T^+, W_T^-, \gamma_T$[1]. The degrees of freedom mentioned in Eq. (2.74) are given by

$$\begin{aligned} &n_{\Phi^0} = 1, \quad n_{\Phi^\pm} = 1, \quad n_{V_T} = 2, \quad n_{V_L} = 1, \\ &n_{l^+} = 2, \quad n_{l^-} = 2, \quad\; n_q = 6, \quad\; n_{\bar{q}} = 6\;\;. \end{aligned}$$

The effective couplings in Eq. (2.100) which are needed to calculate the Debye-corrections to the scalar masses read for the N2HDM scalar contribution

$$\kappa_{ij}^k = \begin{cases} -\left(3\lambda_1 + 2\lambda_3 + \lambda_4 + \frac{1}{2}\lambda_7\right)\delta_{ij} & \phi_i \in \Phi_1 \\ -\left(3\lambda_2 + 2\lambda_3 + \lambda_4 + \frac{1}{2}\lambda_8\right)\delta_{ij} & \phi_i \in \Phi_2 \\ -\frac{3}{2}\lambda_6 - 2(\lambda_7 + \lambda_8) & (i,j) = (9,9) = (\rho_S, \rho_S) \end{cases} \tag{3.25}$$

[1]Due to the finite temperature the photon and Goldstone bosons can acquire an effective thermal mass. Therefore, we need to consider the longitudinal modes as well. In addition a non-zero ω_{CB} can cause a mass difference in the charged particles and a non-zero photon mass. As commented later we exclude these scenarios.

and for the vector boson contribution

$$\kappa_{ij}^{V} = \begin{cases} -\frac{1}{4}\left(3g + g'\right)\delta_{ij} & i \in \{1, \ldots, 8\} \\ 0 & i = 9 = \rho_S\,. \end{cases} \tag{3.26}$$

With the Eq. (2.101) and Eq. (2.104) and the fermionic contribution

$$\Pi_{ii}^{(F)}(0) = \begin{cases} -\frac{y_b^2 T^2}{4} & i = 1, 3, 5, 7 \\ -\frac{y_t^2 T^2}{4} & i = 2, 4, 6, 8 \\ 0 & i = 9\,, \end{cases} \tag{3.27}$$

the scalar polarization tensor can be calculated by using Eq. (2.105). Note that we use Eq. (3.8) to label the corresponding Higgs fields in the gauge basis with the indices $1 \ldots 9$.
Due to the missing singlet coupling to the gauge bosons, the thermal mass corrections of the gauge bosons do not differ from those of the 2HDM. With the thermal VeV $\omega^2 = \omega_1^2 + \omega_2^2$, they are given by [14]

$$\overline{m}_W^2 = \frac{g^2}{4}\omega^2 + 2g^2T^2\,, \tag{3.28a}$$

$$\overline{m}_\gamma^2 = (g^2 + g'^2)\left(T^2 + \frac{\omega^2}{8}\right) - \frac{1}{8}\sqrt{(g^2 - g'^2)^2\left(64T^4 + 16T^2\omega^2\right) + (g^2 + g'^2)^2\omega^4}\,, \tag{3.28b}$$

$$\overline{m}_Z^2 = (g^2 + g'^2)\left(T^2 + \frac{\omega^2}{8}\right) + \frac{1}{8}\sqrt{(g^2 - g'^2)^2\left(64T^4 + 16T^2\omega^2\right) + (g^2 + g'^2)^2\omega^4}\,. \tag{3.28c}$$

Since we are allowing a charge and a CP-breaking VeV at finite temperature, the presented formulas for the bosons masses hold only for $\omega_{CB} = \omega_{CP} = 0$. Note that in the analysis a numerical computation of the boson masses with their full mass matrix is used to obtain the mass values. The numerical results are compared to the values obtained by using Eqs. (3.28). We do not expect to see the generation of CP-violation, due to the CP-conserving potential proposed in Eq. (3.4), nor a CB effect. The comparison of both approaches allows for checking if ω_{CP} or ω_{CB} evolve or have an effect on the masses.

CHAPTER 4

Renormalisation

In this chapter we introduce the renormalisation prescription used in this work. We follow the prescription given in [14].
In the effective potential approach there already is a one-loop contribution at zero temperature, the Coleman-Weinberg potential. Using the approach with the effective potential, includes NLO corrections in the masses. A comparison between simulated data and experimental constraints requires that the loop-corrected masses and mixing angles are taken into account. Since the loop-corrected masses are obtained from the effective potential which itself is subject to constraints, this requires an iterative procedure, which costs a lot of computing time. In order to perform an efficient parameter scan, in the renormalization procedure a finite counter term potential to fix the leading-order masses and mixing angles to their one-loop corrected values is proposed. Thereby the one-loop masses and mixing angles can directly be used as input parameters, which will increase significantly the speed of the parameter scan. The UV divergencies are already absorbed in the $\overline{\text{MS}}$ scheme in V_{CW} so that we are able to modify this renormalisation prescription by introducing a counter term for each parameter of the tree level potential

$$V_{ren.} = V + V_{CT} = V_{tree} + V_{CW} + V_T + V_{CT} \tag{4.1}$$

where V_{CT} reads

$$\begin{aligned} V_{CT} =& \delta m_{11}^2 |\Phi_1|^2 + \delta m_{22}^2 |\Phi_2|^2 - \delta m_{12}^2 \left(\Phi_1^\dagger \Phi_2 + \Phi_2^\dagger \Phi_1\right) + \frac{\delta m_s^2}{2}|S|^2 \\ &+ \frac{\delta\lambda_1}{2}\left(|\Phi_1|^2\right)^2 + \frac{\delta\lambda_2}{2}\left(|\Phi_2|^2\right)^2 + \delta\lambda_3 |\Phi_1|^2|\Phi_2|^2 + \delta\lambda_4\left(\Phi_1^\dagger\Phi_2\right)^2 \\ &+ \frac{\delta\lambda_5}{2}\left((\Phi_1^\dagger\Phi_2)^2 + (\Phi_1^\dagger\Phi_2)^2\right) + \frac{\delta\lambda_6 S^4}{8} + \frac{\delta\lambda_7}{2}\Phi_1^2 S^2 + \frac{\delta\lambda_8}{2}\Phi_2^2 S^2 \\ &+ \delta T_1\left(\rho_1 + v_1\right) + \delta T_2\left(\rho_2 + v_2\right) + \delta T_S\left(\rho_S + v_S\right) \\ &+ \delta T_{CP}\left(\eta_2 + v_{CP}\right) + \delta T_{CB}\left(\xi_2 + v_{CB}\right) \,. \end{aligned} \tag{4.2}$$

In addition we introduced a tadpole counterterm δT_i for each field which acquires a VeV. For the renormalisation conditions we impose the ansatz

$$\partial_{\phi_i} V^{(1)}(T=0) = \partial_{\phi_i} V_{tree}, \quad i \in (1, .., 9) \,, \tag{4.3a}$$

$$\partial_{\phi_i}\partial_{\phi_j}V^{(1)}(T=0)=\partial_{\phi_i}\partial_{\phi_j}V_{tree}, \quad i,j\in(1,..,9)\;. \tag{4.3b}$$

Using this ansatz the minimum remains stable at one-loop level and zero temperature, because Eq.(4.3a) implies the following renormalisation conditions ($i = 1,\ldots,9$)

$$\partial_{\phi_i}V_{CT}(\phi)\big|_{\langle\phi\rangle_{T=0}}=-\partial_{\phi_i}V_{CW}(\phi)\big|_{\langle\phi\rangle_{T=0}} \tag{4.4}$$

with $\phi_i \in \mathrm{B}_{gauge}$ and $\langle\phi\rangle_{T=0}$ is the electroweak minimum defined in Eq. (3.9). To keep the leading-order masses and mixing angles at one-loop, we use Eq. (4.3b) to conclude

$$\partial_{\phi_i}\partial_{\phi_j}V_{CT}(\phi)\big|_{\langle\phi\rangle_{T=0}}=-\partial_{\phi_i}\partial_{\phi_j}V_{CW}(\phi)\big|_{\langle\phi\rangle_{T=0}}\,. \tag{4.5}$$

Applying Eq. (4.4) and Eq. (4.5) to the N2HDM results in 29 non-trivial equations with 17 counterterm parameters. The system is overconstrained and can not be solved. To regularize this equation system we apply two additional conditions on the counterterm parameter sample

$$\delta\lambda_4=0 \quad\text{and}\quad \delta T_S=0\,. \tag{4.6}$$

$\delta\lambda_4$ only occurs as $\delta\lambda_4+\delta\lambda_5$ in these equations, so that setting it to zero does not change physics. Putting δT_S to zero is motivated by physics, because the tadpole counterterms need to vanish anyway. This results in a unique solution for the counterterm parameter set and in additional identities between the first and second derivatives, for example

$$\partial_{\eta_1}\partial_{\eta_2}V_{CW}-\partial_{\chi_1}\partial_{\chi_2}V_{CW}+\frac{v_1}{v_2}\left(\partial_{\eta_1}\partial_{\eta_1}V_{CW}-\partial_{\xi_1}\partial_{\xi_1}V_{CW}\right)=0\,. \tag{4.7}$$

All identities are checked numerically in the analysis and all identities are satisfied up to a numerical fluctuations of order $\mathcal{O}(10^{-9})$. The unique solution for all counterterm parameters reads

$$\delta m_{11}^2=\frac{1}{2}\left[\frac{v_s}{v_1}H^{CW}_{\zeta_1,\zeta_S}+\frac{v_2}{v_1}\left(H^{CW}_{\zeta_1,\zeta_2}-H^{CW}_{\eta_1,\eta_2}\right)+2H^{CW}_{\eta_1,\eta_1}-5H^{CW}_{\eta_1,\eta_1}+H^{CW}_{\zeta_1,\zeta_1}\right]\,, \tag{4.8a}$$

$$\delta m_{22}^2=\frac{1}{2}\left[\frac{v_s}{v_2}H^{CW}_{\zeta_2,\zeta_S}+H^{CW}_{\zeta_2,\zeta_2}-3H^{CW}_{\eta_2,\eta_2}+\frac{v_1}{v_2}\left(H^{CW}_{\zeta_1,\zeta_2}-H^{CW}_{\eta_1,\eta_2}\right)+5\frac{v_1^2}{v_2^2}\left(H^{CW}_{\eta_1,\eta_1}-H^{CW}_{\eta_1,\eta_1}\right)\right]\,, \tag{4.8b}$$

$$\delta m_{12}^2=H^{CW}_{\eta_1,\eta_2}+\frac{v_1}{v_2}\left(H^{CW}_{\eta_1,\eta_1}-H^{CW}_{\eta_1,\eta_1}\right)\,, \tag{4.8c}$$

$$\delta\lambda_1=\frac{1}{v_1^2}\left(2H^{CW}_{\eta_1,\eta_1}-H^{CW}_{\eta_1,\eta_1}-H^{CW}_{\zeta_1,\zeta_1}\right)\,, \tag{4.8d}$$

$$\delta\lambda_2=\frac{1}{v_2^2}\left(H^{CW}_{\eta_2,\eta_2}-H^{CW}_{\zeta_2,\zeta_2}\right)+2\frac{v_1^2}{v_2^4}\left(H^{CW}_{\eta_1,\eta_1}-H^{CW}_{\eta_1,\eta_1}\right)\,, \tag{4.8e}$$

$$\delta\lambda_3=\frac{1}{v_2^2}\left(H^{CW}_{\eta_1,\eta_1}-H^{CW}_{\eta_1,\eta_1}\right)+\frac{1}{v_1v_2}\left(H^{CW}_{\eta_1,\eta_2}-H^{CW}_{\zeta_1,\zeta_2}\right)\,, \tag{4.8f}$$

$$\delta\lambda_4=0\,, \tag{4.8g}$$

$$\delta\lambda_5=\frac{2}{v_2^2}\left(H^{CW}_{\psi_1,\psi_1}-2H^{CW}_{\eta_1,\eta_1}\right)\,, \tag{4.8h}$$

$$\delta m_S^2 = \frac{1}{2}\left(H^{CW}_{\zeta_S,\zeta_S} + \frac{v_2}{v_s}H^{CW}_{\zeta_2,\zeta_S} + \frac{v_1}{v_s}H^{CW}_{\zeta_1,\zeta_S} - \frac{3}{v_S}N^{CW}_{\zeta_S}\right), \tag{4.8i}$$

$$\delta\lambda_6 = \frac{1}{v_s^3}\left(N^{CW}_{\zeta_S} - v_s H^{CW}_{\zeta_S,\zeta_S}\right), \tag{4.8j}$$

$$\delta\lambda_7 = -\frac{1}{v_s v_1}H^{CW}_{\zeta_1,\zeta_S}, \tag{4.8k}$$

$$\delta\lambda_8 = -\frac{1}{v_s v_2}H^{CW}_{\zeta_2,\zeta_S}, \tag{4.8l}$$

$$\delta T_1 = H^{CW}_{\eta_1,\eta_1}v_1 + H^{CW}_{\eta_1,\eta_2}v_2 - N^{CW}_{\zeta_1}, \tag{4.8m}$$

$$\delta T_2 = \frac{v_1^2}{v_2}\left(H^{CW}_{\eta_1,\eta_1} - H^{CW}_{\psi_1,\psi_1}\right) + H^{CW}_{\eta_1,\eta_2}v_1 + H_{\eta_2,\eta_2}v_2 - N^{CW}_{\rho_2}, \tag{4.8n}$$

$$\delta T_S = 0, \tag{4.8o}$$

$$\delta T_3 = \frac{v_1^2}{v_2}H^{CW}_{\zeta_1,\psi_1} + H^{CW}_{\zeta_1,\psi_2}v_1 - N^{CW}_{\psi_2}, \tag{4.8p}$$

$$\delta T_{CB} = -N^{CW1}_{\rho_2}. \tag{4.8q}$$

Here we used a shorthand notation for the first derivative of the Coleman-Weinberg potential

$$N^{CW}_{\phi_i} \equiv \partial_{\phi_i} V_{CW} \tag{4.9}$$

and for the second derivative

$$H^{CW}_{\phi_i\phi_j} = \partial_{\phi_i}\partial_{\phi_j} V_{CW}. \tag{4.10}$$

Reference [54] provides the needed formulas for the first and second derivatives of V_{CW} expressed in terms of the leading-order couplings and masses.
To take into account numerical fluctuations we require that the EW minimum remains at one-loop within the interval

$$|v_{EW} - v_{1-loop}| \leq 2 \text{ GeV}. \tag{4.11}$$

As the conditions on V_{CT} only enforce v_{EW} to be a local minimum we have to check numerically if it is still the global one. The range of 2 GeV is chosen by hand and the exact value does not have an influence on our results. Indeed it is not guaranteed that the electroweak vacuum remains at its leading-order value v_{EW} at NLO. We investigate this NLO vacuum stability after performing the renormalisation prescription presented here. In the following analysis we call a parameter point *stable*, when the electroweak vacuum fulfills Eq. (4.11) at NLO. For a more detailed explanation of the analysis, see Chapter 5.

CHAPTER 5

Numerical Analysis

In order to quantify the strength of the phase transition of a given parameter point, it is necessary to calculate

$$\xi_C = \frac{\langle \phi_C \rangle}{T_C} \,. \tag{5.1}$$

$\langle \phi_C \rangle$ is the field configuration of the broken ground state at the critical temperature. The critical temperature is defined as the temperature at which two degenerate vacua coexist, the symmetric one at $v = 0$ and the broken phase at $v \neq 0$. A sufficient condition for the electroweak phase transition is to require [29]

$$\xi_C \geq 1 \,. \tag{5.2}$$

In the following section we present the numerical analysis for the calculation of this quantity.

5.1 Minimisation of the Potential

We implemented the formulas for the effective potential and the model, following the previous chapters, in a C++ class used by the in house program in order to calculate the effective potential at a given VeV configuration $\{\omega_i\}$ and at a given temperature T. To find the global minimum[1], we use two different algorithms for the numerical minimisation. This enables us to cross check both algorithms with respect to numerical instabilities. The first one is the CMA − ES algorithm [55]. We use 10^{-5} for the relative tolerance between two solutions found by this algorithm. The other algorithm is the local Nelder-Mead-Simplex algorithm from the GNU Scientific Library [56] (GSL_multimin_fminimizer_nmsimplex2), also with a tolerance of 10^{-5}. For the GSL algorithm we produce 500 random VeV configurations in the interval

$$\omega_{1,2,CP,CB} \in [-500, 500]\,\text{GeV}, \quad \omega_S \in [1, 1000] \;\; \text{GeV} \tag{5.3}$$

[1] Metastable vacua and tunnneling is out of scope of this work.

and use the GSL algorithm to find the next local minimum. Since the selection of the interval of ω_S has no effect on the numerical calculation of the global minimum, we choose the same parameter range for ω_S as chosen in the ScannerS parameter setting. Among the 500 obtained solutions of the GSL algorithm, the solution with the lowest value of the effective potential is chosen as the global minimum. The solutions of the CMA-ES and GSL algorithms are compared numerically and the lower value of the effective potential is taken as the solution for the ground state for the given temperature. Although we allow the CP and CB VeV to evolve at finite temperature, we observe that in all scanned parameter points up to numerical fluctuations the CB and CP VeVs do not acquire any significant values[2]. To determine T_C we use a bisection method starting at the temperature $T_S = 0$ and ending at $T_E = 300$ GeV. We determine the global electroweak minimum and its corresponding electroweak VeV

$$v_{EW,T}^2 = \omega_1^2 + \omega_2^2 + \omega_{CP}^2 + \omega_{CB}^2 \neq 0 \tag{5.4}$$

at each temperature step and look for the temperature interval where the $v_{EW,T}$ *jumps to zero*. At this point there exist two degenerated ground states, the symmetric state ($v_{EW,T} = 0$) and the broken state ($v_{EW,T} \neq 0$). We stop the bisection as soon as the corresponding temperature interval gets smaller than 10^{-2} GeV and define the beginning of the temperature interval as T_C, respectively, $v_{EW,T_C} = v_C$. In addition to that we exclude points that acquire an electroweak VeV, which does not obey

$$\left| v_{EW} - 246.22 \text{ GeV} \right| \leq 2 \text{ GeV} \tag{5.5}$$

at zero temperature or which do not acquire a zero-valued electroweak VeV at T_E. Once T_C is determined, the corresponding VeV configuration $\langle \phi_C \rangle$ can be extracted by

$$v_C = \langle \phi_C \rangle \,. \tag{5.6}$$

5.2 Constraints and Parameter Scan

In our numerical analysis we will discuss type I and type II N2HDM. For our parameter scan we use parameter points which are already physical in the sense that they obey theoretical and experimental constraints. As theoretical constraints we require that the tree level potential is bounded from below [52], that tree level perturbative unitarity holds and that the electroweak minimum is the global one. All these requirements are implemented in ScannerS and discussed in [51] for the N2HDM. ScannerS provides the possibility to check for recent collider constraints, like electroweak precision constraints with the oblique parameters S,T and U calculated with the general formulas provided by [57, 58]. A 2σ compatibility with the SM fit [59] including the full correlations is demanded. In addition, ScannerS enables to check

[2]Since we do not take into account CP-violation in our model for example through a CP-violating CKM, we did not expect to observe CP-violation in our analysis. The CB effects are observed for few parameter points, but all these points are excluded consistently in our analysis, because they are unphysical.

for the exclusion bounds arising from Tevatron, LEP and LHC. For this it uses an interface with HiggsBounds v4.3.1 [60–62] which is used for a compatibility check with all 2σ exclusion limits from LEP, Tevatron and LHC Higgs searches. The needed cross section ratios are provided by N2HDECAY [51, 63] and the dominant production cross sections via gluon fusion (ggF) and b-quark fusion (bbF) are obtained at next-to-next-to-leading order QCD from SusHi v1.6.0 [64, 65].
The check of the compatibility of the discovered Higgs signal with respect to the SM-like Higgs boson is obtained by using the individual signal strengths fit of Ref. [66]. This approach is used for simplicity. A global fit to current Higgs data is likely to give a stronger bound than this approach. The fermion initiated cross section normalized to the SM is given by

$$\mu_F = \frac{\sigma_{N2HDM}(ggF) + \sigma_{N2HDM}(bbF)}{\sigma_{SM}(ggF)}\,, \tag{5.7}$$

where the bbF contribution of the SM in the normalization is neglected, because it is small compared to gluon fusion. The production through vector boson fusion (VBF) or associated production with a vector boson (VH) normalized to the SM reads

$$\mu_V = \frac{\sigma_{N2HDM}(VBF)}{\sigma_{SM}(VBF)} = \frac{\sigma_{N2HDM}(VH)}{\sigma_{SM}(VH)}\,. \tag{5.8}$$

For the check of the properties of the SM-like Higgs boson we use

$$\mu_{xx} = \mu_F \frac{\mathrm{BR}_{N2HDM}(h_{125} \to xx)}{\mathrm{BR}_{SM}(H_{SM} \to xx)}\,, \tag{5.9}$$

where H_{SM} denotes the SM Higgs boson with mass 125.09 GeV. Recent studies on $\mathcal{R}_b$ [67, 68] and $B \to Xs\gamma$ [69–71] give 2σ exclusion bounds in the $m_{H^\pm} - \tan\beta$ plane. These bounds enforce in the type II model[3] [72]

$$m_{H^\pm} \geq 580 \text{ GeV}\,. \tag{5.10}$$

For the type I model the constraint on the charged Higgs boson is more strongly dependent on $\tan\beta$ so that the bounds on the charged mass are weaker. For our analysis, we then use the parameter points obtained with ScannerS which fulfill the above described theoretical and experimental constraints. The scan ranges of the physical parameters are given in Tables 5.1 and 5.2 for type I and II, respectively. We force one CP-even Higgs boson to be the SM-like Higgs boson with a mass of $m_{h_{125}} =$ 125.09 GeV [73], which we refer to as h_{125}. We do not take into account degenerate Higgs signals and therefore scenarios with non-SM-like Higgs bosons within the mass window of 125 GeV $\pm$ 5 GeV are excluded. The remaining two non-SM-like CP-even Higgs bosons are labeled as $h_\downarrow$ and $h_\uparrow$ where $h_\downarrow$ denotes to the mass eigenstate with the lower mass[4] compared to $h_\uparrow$. Their masses are labeled as $m_\downarrow$ and $m_\uparrow$, respectively. Now three different mass hierarchies are possible

[3]These studies consider the 2HDM. Since the charged and pseudoscalar sector of the 2HDM and the N2HDM are identical, the experimental constraints hold also for the N2HDM.

[4]Remember the implied mass hierarchy $m_{H_1} \leq m_{H_2} \leq m_{H_3}$.

$m_{h_{125}}$	$m_{\downarrow}$	$m_{\uparrow}$ in GeV	m_A	$m_{H^{\pm}}$	m_{12}^2 in GeV^2
125.09	30-1000	30-1000	30-1000	30-1000	0-10^5

Table 5.1: Parameter ranges for the type I N2HDM used in ScannerS.

$m_{h_{125}}$	$m_{\downarrow}$	$m_{\uparrow}$ in GeV	m_A	$m_{H^{\pm}}$	m_{12}^2 in GeV^2
125.09	30-1000	30-1000	30-1000	580-1000	0-10^5

Table 5.2: Parameter ranges for the type II N2HDM used in ScannerS.

1. $m_{h_{125}} \leq m_{\downarrow} \leq m_{\uparrow}$
2. $m_{\downarrow} \leq m_{h_{125}} \leq m_{\uparrow}$
3. $m_{\downarrow} \leq m_{\uparrow} \leq m_{h_{125}}$

which we call mass order M_1, M_2 and M_3.
The SM parameter we are using in the analysis are given in the following: We use the fine structure constant taken at the Z boson mass scale [74, 75]

$$\alpha_{EM}^{-1}(M_Z^2) = 128.962 \tag{5.11}$$

and the masses for the massive gauge bosons are chosen as

$$m_W = 80.385 \text{ GeV} \quad \text{and} \quad M_Z = 91.1876 \text{ GeV}\,. \tag{5.12}$$

For the lepton masses we choose

$$m_e = 0.510998928 \text{ MeV}, \quad m_\mu = 105.6583715 \text{ MeV}, \quad m_\tau = 1.77682 \text{ GeV}\,, \tag{5.13}$$

and for the light quark masses

$$m_u = m_d = m_s = 100 \text{ MeV}\,. \tag{5.14}$$

To be consistent with the CMS and ATLAS analyses, we take the on-shell top quark mass as [76]

$$m_t = 172.5 \text{ GeV} \tag{5.15}$$

and the recommended charm and bottom quark on-shell masses

$$m_c = 1.51 \text{ GeV} \quad \text{and} \quad m_b = 4.92 \text{ GeV}\,. \tag{5.16}$$

For simplicity we take the CKM as unit matrix. Finally the electroweak VeV is set

$$v_{EW} = 1/\sqrt{\sqrt{2}G_F} = 246.22 \text{ GeV}\,. \tag{5.17}$$

5.3 General Idea of the Analysis

In the following we present the general idea of our analysis. We start with a sample of *physical* parameter points provided by ScannerS. These points are compatible with the described theoretical and experimental constraints. As a first step we check the vacuum stability at NLO. For this purpose we check if the global minimum of the one-loop effective potential remains at the electroweak VeV, using Eq. (5.5). Unstable points are considered as unphysical and are excluded from the analysis. In addition we observe that some of the points generate a v_{CB} of the order of a few GeV. These points with a charge breaking VeV configuration are excluded as well because they are unphysical. Points with

$$|v_{CB}| \geq 1 \text{ GeV} \tag{5.18}$$

are excluded. This threshold will exclude all non-physical points but at the same time it is not sensitive to numerical fluctuations, which have a magnitude of order $\mathcal{O}(10^{-4})$. With our chosen renormalisation prescription the NLO corrections to the Higgs self-couplings might get large so that the unitarity constraint applied in ScannerS can be spoiled at NLO. These unitarity constraints have been derived for the tree-level couplings for the N2HDM in [51]. They read

$$|\lambda_3 - \lambda_4| < 8\pi \,, \tag{5.19a}$$

$$|\lambda_3 + 2\lambda_4 \pm 3\lambda_5| < 8\pi \,, \tag{5.19b}$$

$$|\frac{1}{2}\left(\lambda_1 + \lambda_2 + \sqrt{(\lambda_1 - \lambda_2)^2 + 4\lambda_4^2}\right)| < 8\pi \,, \tag{5.19c}$$

$$|\frac{1}{2}\left(\lambda_1 + \lambda_2 + \sqrt{(\lambda_1 - \lambda_2)^2 + 4\lambda_5^2}\right)| < 8\pi \,, \tag{5.19d}$$

$$|\frac{1}{2}a_{1,2,3}| < 8\pi \,, \tag{5.19e}$$

where $a_{1,2,3}$ are the real solutions of

$$\begin{aligned} &4\left(-27\lambda_1\lambda_2\lambda_6 + 12\lambda_3^2\lambda_6 + 12\lambda_3\lambda_4\lambda_6 + 3\lambda_4^2\lambda_6 + 6\lambda_2\lambda_7^2 - 8\lambda_3\lambda_7\lambda_8 - 4\lambda_4\lambda_7\lambda_8 + 6\lambda_1\lambda_8^2\right) \\ &+ x\left(36\lambda_1\lambda_2 - 16\lambda_3\lambda_4 - 4\lambda_4^2 + 18\lambda_1\lambda_6 + 18\lambda_2\lambda_6 - 4\lambda_7^2 - 4\lambda_8^2\right) \\ &+ x^2\left(-6(\lambda_1 + \lambda_2) - 3\lambda_6\right) + x^3 = 0 \,. \end{aligned} \tag{5.20}$$

In a first rough approximation we insert the one-loop corrected self-couplings extracted from the loop-corrected effective potential in the unitarity constraints in Eq. (5.19). This approach allows for an approximate estimate of the unitarity stability without calculating the full NLO $2 \to 2$ scattering matrix. To further constrain the phase space, we require that the retained parameter points provide a sufficiently strong phase transition of first order. This can be achieved by imposing Eq. (5.2). Points with $\xi_C \leq 1$ cannot produce a net baryon number that would explain the baryon asymmetry observed today; therefore we are considering these points to be unphysical as well. The phenomenology of the phase space of the N2HDM providing a strong first order electroweak phase transition will be discussed in detail. In addition, the remaining points will be investigated with respect to the trilinear self-couplings between the massive particles. Using the formulas for the third derivatives of V_{CW} [54], the trilinear couplings are calculated between all massive Higgs states and compared to their tree level values and to the SM value.

CHAPTER 6

Results

In the following we present the results of the analysis. We consider both type I and type II of the N2HDM. The phenomenology of the mass hierarchy M_1 is discussed in detail, while the other mass hierarchies M_2 and M_3 are not presented to the same extent, because our used parameter sample does not provide a sufficient number of parameter points. In our parameter sample only one point provides a strong first order electroweak phase transition with the mass hierarchy M_3 so that this point will be discussed exceptionally.

6.1 NLO Constraints

We first present the results of the NLO vacuum stability check. An overview of the sample size is given in Table 6.1. In both types around $\sim 20\%$ of the M_1 sample is lost due to the NLO vacuum stability while in the second mass order M_2 almost half of the parameter space is lost. A significant difference between both types can be observed in the NLO unitarity check through our approximate approach presented in Chapter 5.3. In the type I N2HDM $\sim 20\%$ of the remaining parameter points are excluded due to the NLO unitarity constraint, on the other hand in the type II N2HDM almost all parameter points with a stable electroweak vacuum obey the NLO unitarity requirement. In Fig. 6.1 two examples, one for the type I and one for type II, of the allowed mass regions of the N2HDM are shown with the black points denoting the full sample that fulfills the theoretical and valid collider constraints. The grey points passed the NLO vacuum stability check, the blue ones obey the NLO unitarity and the orange coloured points provide an SFOEWPT. Overall the NLO check does not have any significant visible effects on the phase space. The two presented examples, however, show an observable and exceptional effect on the phase space. The mass plane in Fig. 6.1a shows the mass differences of the CP-even non-SM Higgs bosons $h_\uparrow$ and $h_\downarrow$ compared to the charged Higgs boson mass. In the mass region $m_\uparrow - m_{H^\pm} \lesssim -350$ GeV only few parameter points remain which provide a stable electroweak vacuum and fulfill NLO unitarity. In Fig. 6.1b the mass plane m_A and $m_{H^\pm}$ for the type II model is shown. The mass region $m_A \leq 340$ GeV is quite

Model	ScannerS	NLO stable vacuum	NLO unitarity	SFOEWPT
TI M_1	464571	371440($\cong$ 80.0%)	282751($\cong$ 76.1%)	1583($\cong$ 0.6%)
TI M_2	31750	18508($\cong$ 58.3%)	14888($\cong$ 80.4%)	66($\cong$ 0.4%)
TI M_3	3677	1726($\cong$ 46.7%)	1406($\cong$ 81.1%)	1($\approx$ 1‰)
TII M_1	495118	424551($\cong$ 85.2%)	412468($\cong$ 97.2%)	3713($\cong$ 0.9%)
TII M_2	4732	2331($\cong$ 49.3%)	2271($\cong$ 97.4%)	97($\cong$ 4.3%)
TII M_3	52	0	0	0

Table 6.1: Overview of the sample size for the three different mass orders M_1, M_2 and M_3: starting with the provided ScannerS sample which fulfills theoretical and experimental constraints, followed by the remaining sample size which provides a stable electroweak NLO vacuum and NLO unitarity. Finally in the last column the sample size with an SFOEWPT is shown. In brackets the percentage of the remaining sample size with respect to the previously applied constraint is given.

interesting for phenomenological reasons. The pseudoscalar with $m_A \lesssim 340$ GeV has a significant branching ratio into Zh [14]. These relatively large branching ratios allow for collider searches in this mass region, and quite some parameter space has already been excluded experimentally [77–79]. By requiring a stable electroweak vacuum, the smallest masses of m_A are almost excluded, while the NLO unitarity forces $m_A \geq 200$ GeV. The impact of the PT will be discussed later.

6.2 Electroweak Phase Transition

In the following we present the implications of the requirement of the electroweak phase transition. We start with rather pedagogical examples to show the effects of the finite temperature on the effective potential. For this purpose we take a valid type I N2HDM parameter point given by

$$m_\downarrow = 172.2 \text{ GeV}, \; m_\uparrow = 903.5 \text{ GeV}, \; m_A = 512.2 \text{ GeV}, \; m_{H^\pm} = 145.9 \text{ GeV}, \tag{6.1a}$$

$$\tan\beta = 1.36, \; \alpha_1 = 1.36, \; \alpha_2 = -0.06, \; \alpha_3 = -0.03, \tag{6.1b}$$

$$v_C = 180.8 \text{ GeV}, \; T_C = 120.7 \text{ GeV} \tag{6.1c}$$

and show the evolution of the effective potential for different temperatures in Fig. 6.2. In order to see the evolution of the effective potential V_{eff} in terms of the electroweak VeV, we choose the *electroweak path*

$$\{0, 0, 0, 0, v_S^{min}\} \to \{\omega_1^{min}, \omega_2^{min}, \omega_{CP}^{min}, \omega_{CB}^{min}, v_S^{min}\} . \tag{6.2}$$

Since we keep v_S fixed at this path, we are able to see the evolution of the effective potential induced only by the electroweak VeV. We choose v_S to be fixed at its zero

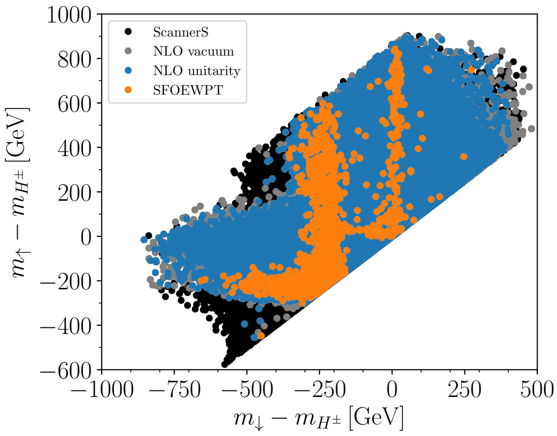

(a) Type I and mass order I

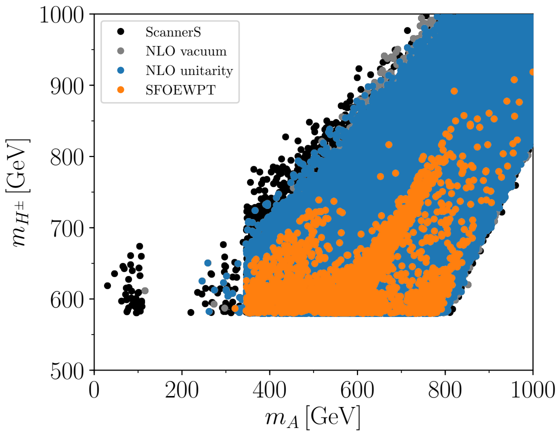

(b) Type II and mass order I

Figure 6.1: Black points denote the full ScannerS sample. Grey points passed the NLO vacuum stability check and the blue points obey the NLO unitarity checks. The orange points provide an SFOEWPT. Left: The mass differences $m_\uparrow - m_{H^\pm}$ versus $m_\downarrow - m_{H^\pm}$ for the type I in the mass order M_1; right: the pseudoscalar mass m_A versus the charged mass $m_{H^\pm}$ for the type II in the mass order M_1.

temperature value for that we minimised the effective potential at zero temperature and denote the VeV configuration as

$$v_i^{min} = \omega_i^{min}\Big|_{T=0}, \quad i = 1, 2, CP, CB, S\,. \tag{6.3}$$

Starting at zero temperature the effective potential has a potential barrier between its symmetric and broken phase, while the broken phase it is still deeper. Increasing the temperature leads to decreasing the electroweak VeV, which is given by

$$\omega_{EW}^2 = \omega_1^2 + \omega_2^2 + \omega_{CP}^2 + \omega_{CB}^2\,. \tag{6.4}$$

Increasing the temperature the global minimum gets enhanced, until it is degenerate with the symmetric phase. For temperatures $T \geq T_C$ the potential is symmetric and only one minimum exists, the symmetric phase at $\{\omega\} = (0, v_S^{min})$. For a clearer overview of the VeV evolution see Fig. 6.3. In the upper plot of Fig. 6.3 the evolution of the electroweak (blue) and the singlet VeV (orange) as a function of the temperature can be seen. The electroweak VeV starts at the standard value at zero temperature $v_{EW} = 246.22$ GeV and slowly decreases with increasing temperature. At the critical temperature, the global minimum jumps from the broken phase to the symmetric one, observable through the jump from v_C to zero at T_C. At this parameter point, the singlet VeV does not show any significant signs of evolution with increasing temperature, but this does not hold as a general statement. There are parameter points which show a singlet VeV evolution. The evolution of the electroweak VeV with its jump at T_C is typical for a phase transition of first order. For a phase transition of second order, we would observe a continuous transition from v_{EW} to zero.

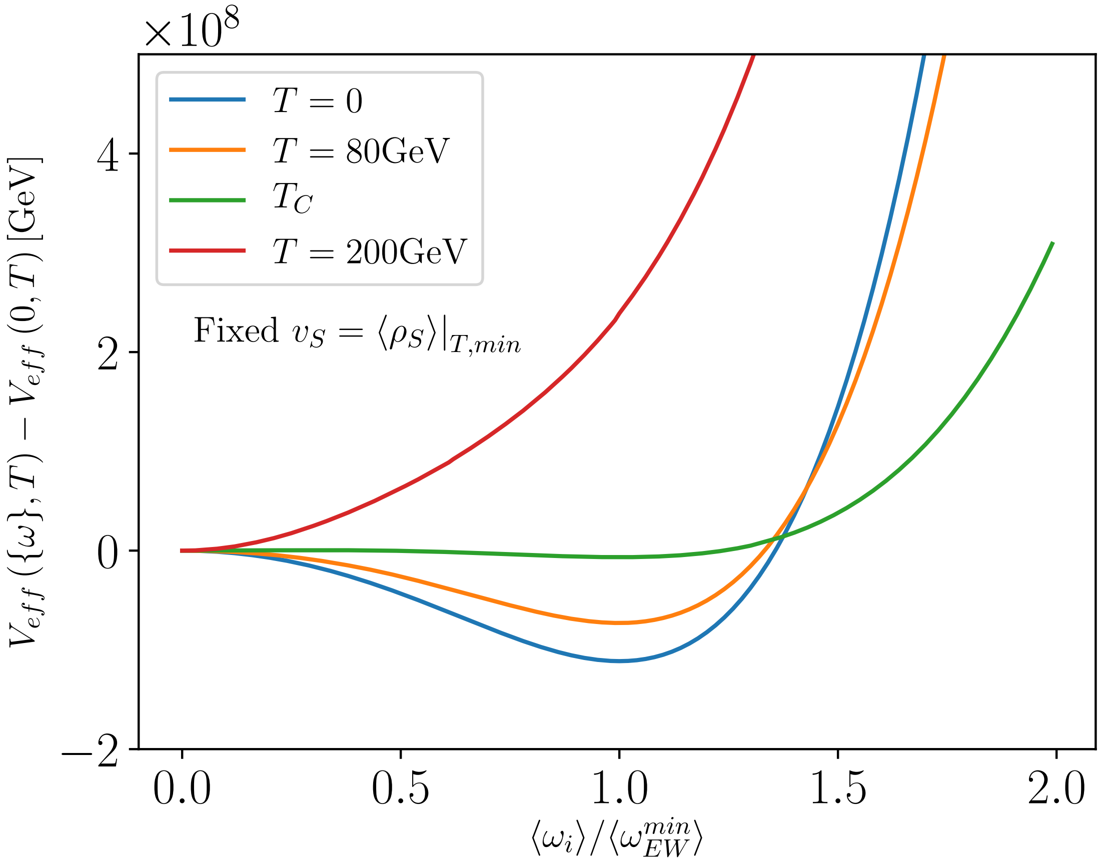

Figure 6.2: Evolution of the effective potential along the *electroweak* direction for different temperatures.

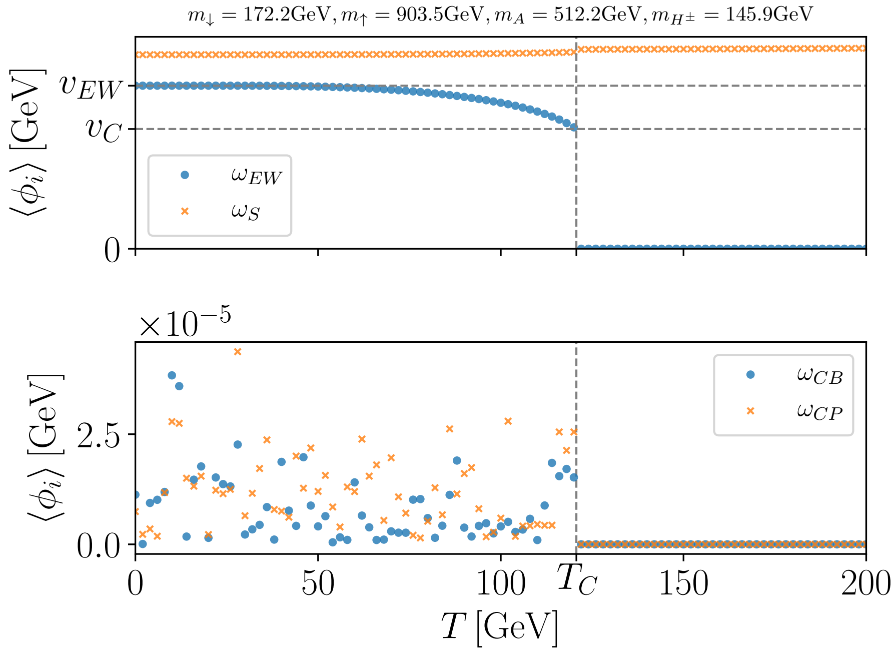

Figure 6.3: Upper half: The electroweak VeV (blue) and the singlet VeV (orange) as a function of the temperature; lower half: The CP (orange) and CB (blue) VeV as a function of the temperature.

In the lower plot of Fig. 6.3 the charge (blue) and CP-breaking (orange) VeVs ω_{CB} and ω_{CP} with rising temperature are displayed. Note that the axis is multiplied with 10^{-5} so that the magnitude of ω_{CB} and ω_{CP} is of order $\mathcal{O}(10^{-5})$ and can be explained as numerical fluctuations. In our numerical analysis we chose 0.5 GeV as threshold for the electroweak VeV, such that a electroweak VeV configuration with

$$\omega_{EW} = \sqrt{\omega_1^2 + \omega_2^2 + \omega_{CP}^2 + \omega_{CB}^2} \leq 0.5 \text{ GeV} \tag{6.5}$$

is set to zero. Therefore all ω_{CP} and ω_{CB} are zero above the critical temperature. We observe in our analysis, that ω_{CP} does not gain any significant values at zero or finite temperature, so that we can conclude that the CP-conservation is a symmetry, which remains stable at finite temperature in the N2HDM. Note that we did not include CP violation in the CKM matrix, which we set to unity. Only a few points acquired a CB VeV ω_{CB} of order of some GeV, but these points are excluded from our analysis, because they are unphysical.

6.2.1 Mass order M_1 and Type I

In this section we address the implication of the electroweak phase transition on the parameter sample of type I with the mass order M_1. To start this discussion, first the relevant particles and physical parameters of interest shall be elucidated: In the N2HDM we have five non-SM Higgs bosons: the pseudoscalar A, the charged $H^\pm$ and two neutral scalar Higgs bosons $h_\downarrow, h_\uparrow$. All of them are massive particles,

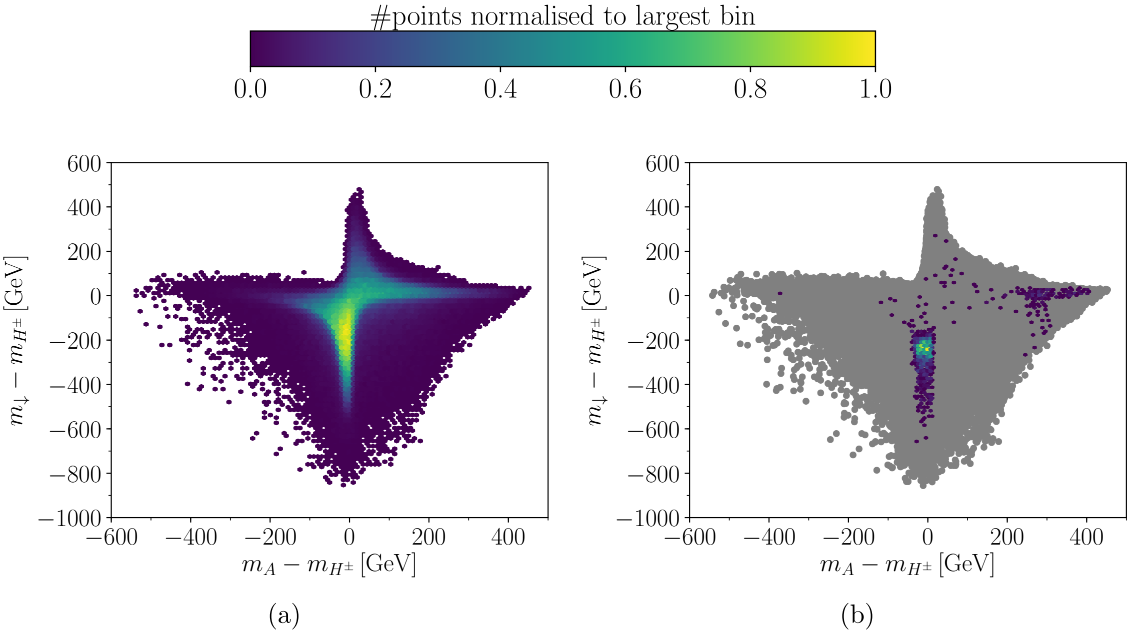

Figure 6.4: Type I and mass order M_1: The mass differences $m_A - m_{H^\pm}$ versus $m_\downarrow - m_{H^\pm}$. Left: the ScannerS sample with all parameter points fulfilling theoretical and experimental constraints; right: Grey points correspond to the ScannerS sample and the coloured points provide an SFOEWPT. The colour code denotes the relative frequency normalized to the largest bin.

masses of which can in principle be measured at the LHC. Due to the electroweak precision variables, the charged mass is the strongest constrained mass parameter. In type I, small charged masses are still possible but forced to be degenerate with another non-SM Higgs boson by the S, T and U parameters. This behavior can be observed in Fig. 6.4a, where the relative frequencies of the ScannerS sample of the mass differences $m_A - m_{H^\pm}$ versus $m_\downarrow - m_{H^\pm}$ are shown for type I. The colour code denotes the relative frequency normalized to the largest bin. Most points in Fig. 6.4a have a small mass difference which indicates the mass degeneracy of the charged Higgs boson mass with the corresponding particle. Nevertheless, there is still some allowed phase space with a finite mass gap. Considering the requirement of an SFOEWPT in Fig. 6.4b, the same mass configuration is displayed with the whole ScannerS sample denoted by the grey points. Parameter points providing an SFOEWPT are shown with the colour code indicating the relative frequencies. The phase transition favors the mass degeneracy of m_A with $m_{H^\pm}$ and a mass gap of around 200 GeV between $m_\downarrow$ and $m_{H^\pm}$, while the other scenario $m_{H^\pm} \approx m_\downarrow$ is still possible. Apart from a few exceptions, in this scenario only points with enhanced pseudoscalar masses survive the requirement of an SFOEWPT.
In Fig. 6.5 the mass differences $m_A - m_{H^\pm}$ versus $m_\uparrow - m_{H^\pm}$ are shown. The colour code denotes the relative frequencies normalised to the largest bin. On the left side the full ScannerS sample, while on the right side the parameter points providing an SFOEWPT (coloured) are shown. The grey points in the background indicates

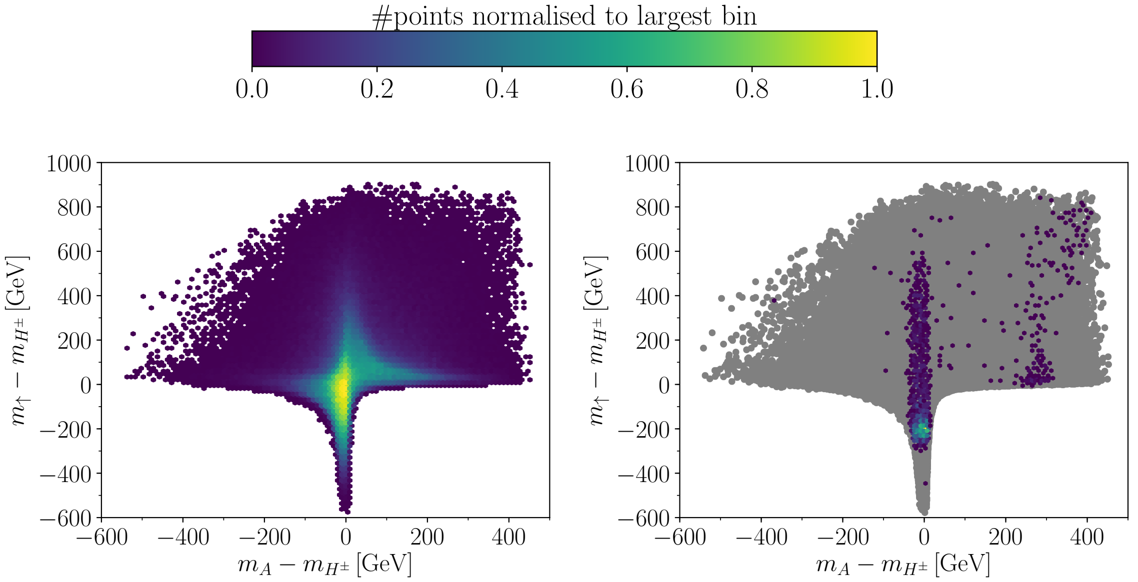

(a) (b)

Figure 6.5: Type I and mass order M_1: The mass differences $m_A - m_{H^\pm}$ versus $m_\uparrow - m_{H^\pm}$. Left: the ScannerS sample with all parameter points fulfilling theoretical and experimental constraints; right: Grey points correspond to the ScannerS sample and the coloured points provide an SFOEWPT. The colour code denotes the relative frequency normalized to the largest bin.

the ScannerS sample. As can be inferred from Fig. 6.5a, the oblique parameters accounting for the EW precision data force the mass differences between m_A and $m_{H^\pm}$ to be small if the charged mass gets larger than $m_\uparrow$. The favored mass configuration of the ScannerS sample indicates that the masses $m_A, m_{H^\pm}$ and $m_\uparrow$ are all close to each other. By requiring the SFOEWPT two branches are forming in the mass plane given in Fig. 6.5b. The first one is at $m_A \approx m_{H^\pm}$, where a shift of the density to a larger mass gap between $m_\uparrow$ and $m_{H^\pm}$ around 250 GeV is observable. The second branch is at $m_A - m_{H^\pm} \approx 230$ GeV. These points are corresponding to the branch with $m_\downarrow - m_{H^\pm} \approx 0$ GeV in Fig. 6.4b.
In Figs. 6.6a and 6.6b the mass plane $m_\downarrow$ versus m_A is displayed. Here a significant change is visible in the relative frequency density if an SFOEWPT is required. On the left side the full parameter sample of ScannerS is provided. On the right side one sees that CP-even scalar masses $m_\downarrow$ around 400 GeV are favored by the SFOEWPT, while the mass interval from 180 GeV up to 1000 GeV is allowed by theoretical and experimental constraints. In addition, the pseudoscalar masses around 600 GeV are favored by an SFOEWPT. In [80] it was suggested to use the decay $A \to ZH$ as a benchmark process. Here the authors claim that the SFOEWPT strongly favors the mass regions in which $m_A \geq m_H + m_Z$. Therefore by taking into account the possibility of an SFOEWPT, future studies of this particular decay channel may allow to obtain a *smoking gun signal* for the 2HDM. For this reason, we added the

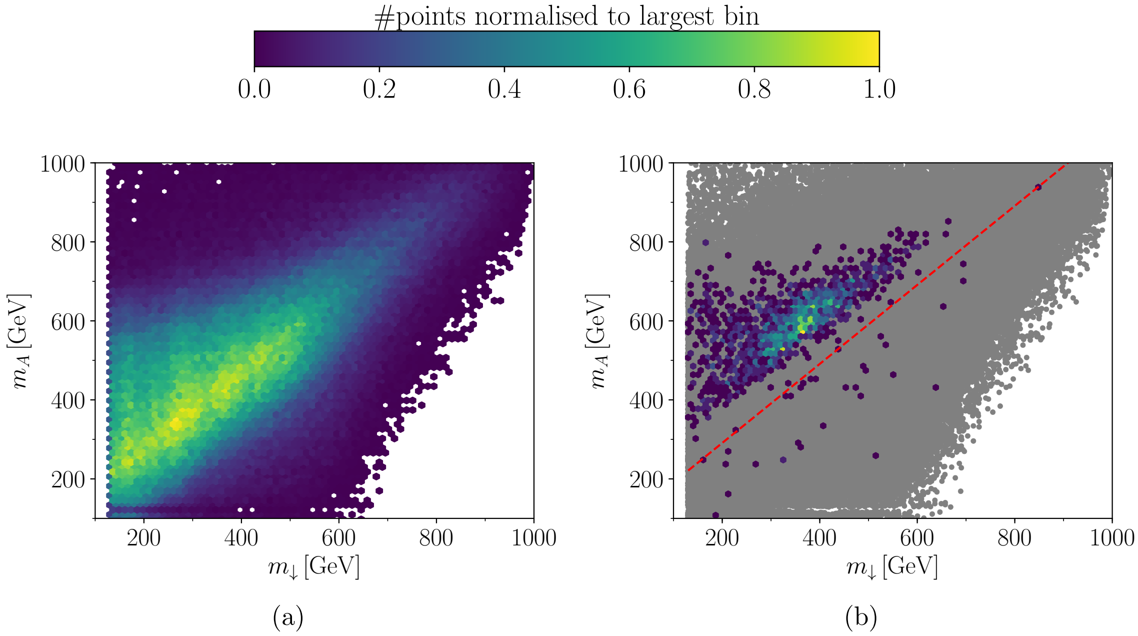

Figure 6.6: Type I and mass order M_1: The mass plane $m_\downarrow$ versus m_A. Left: the ScannerS sample with all parameter points fulfilling theoretical and experimental constraints; right: Grey points correspond to the ScannerS sample and the coloured points provide an SFOEWPT. The colour code denotes the relative frequency normalized to the largest bin. The red line on the right plot denotes the mass relation $m_A = m_\downarrow + m_Z$.

red line in Fig. 6.6b which displays

$$m_A = m_\downarrow + m_Z\,. \tag{6.6}$$

It can be seen that the PT in fact pushes the phase space above the red line, which confirms the prediction of [80]. Nevertheless the N2HDM still allows for scenarios with $m_A \leq m_\downarrow + m_Z$. To end the phenomenological discussion of the masses in type I and the mass order M_1 we turn to Fig. 6.7. We define the mass asymmetry as follows

$$\Delta_{m_1,m_2} = \frac{m_1 - m_2}{m_1 + m_2}\,, \tag{6.7}$$

so that two masses which are degenerate have a Δ of approximately zero. In Fig. 6.7 we show $\Delta_{m_\downarrow,m_{H^\pm}}$ versus $\Delta_{m_\uparrow,m_{H^\pm}}$ and the colour code denotes $\Delta_{m_A,m_{H^\pm}}$. In this way we compare all non-SM Higgs bosons to the charged Higgs boson at once. All points which have a non-zero color code, i.e. those points which fulfill an SFOEWPT, lie in the interval 0% up to 15% of either $\Delta_{m_\downarrow,m_{H^\pm}}$ or $\Delta_{m_\uparrow,m_{H^\pm}}$. All other points are close to zero in $\Delta_{m_A,m_{H^\pm}}$. Therefore we can conclude that the PT favors scenarios in which the charged mass is degenerate with at least one of the non-SM Higgs bosons in a range of up to 15%. By further investigation of all mass distributions, we observe the tendency, that the scalar masses $m_\downarrow$ and $m_\uparrow$ get decreased by the SFOEWPT and on the other hand the charged and CP-odd scalar tend to larger masses.

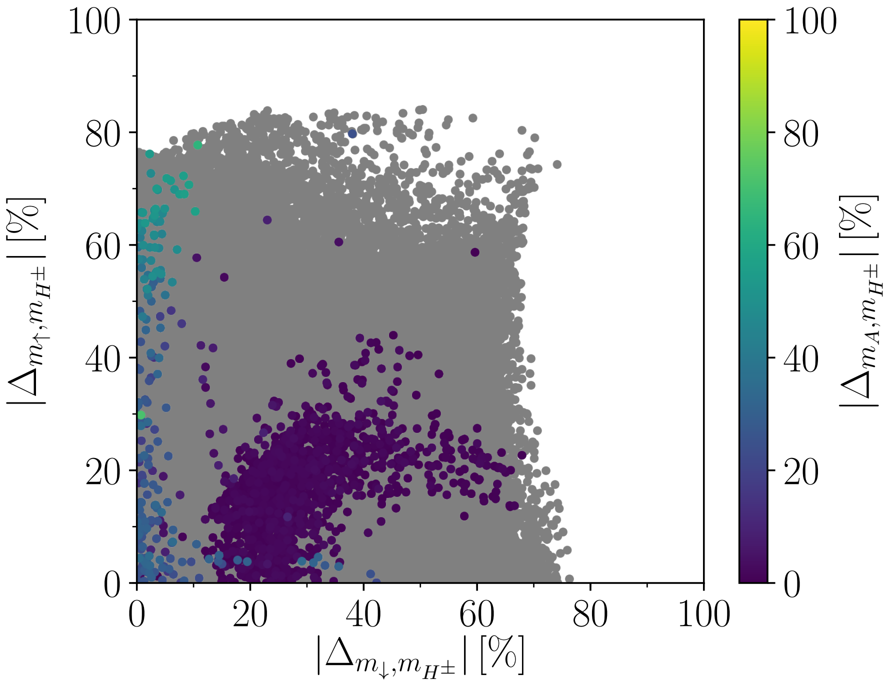

Figure 6.7: Type I and mass order M_1: The mass asymmetries of all non-SM Higgs bosons in the N2HDM compared the charged Higgs boson mass. Grey points correspond to the ScannerS sample and coloured points provide an SFOEWPT.

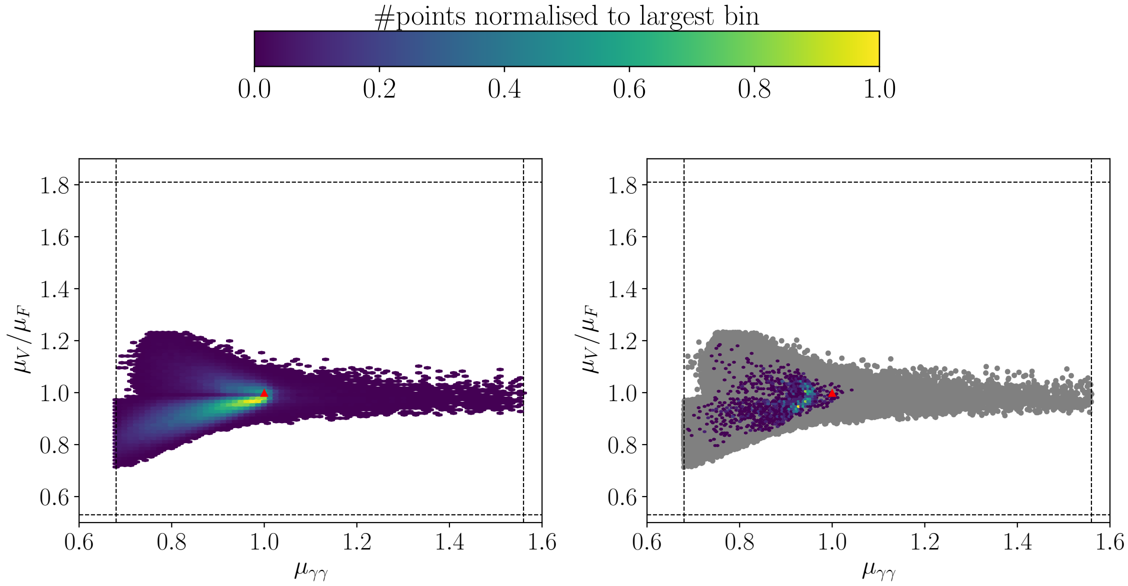

(a)

(b)

Figure 6.8: Type I and mass order M_1: $\mu_{\gamma\gamma}$ versus μ_V/mu_F. Left: the ScannerS sample with all parameter points fulfilling theoretical and experimental constraints; right: Grey points correspond to the ScannerS sample and the coloured points provide an SFOEWPT. The colour code denotes the relative frequency normalized to the largest bin.

Another phenomenologically interesting quantity is the signal rate of the SM-like Higgs boson, which checks the compatibility of the discovered Higgs signal with h_{125}. The investigation of the signal rates in view of an SFOEWPT gives us insights in the prefered decay channels with respect to succesful baryogenesis. In Fig. 6.8 we display the signal rates of the discovery channel $\mu_{\gamma\gamma}$ versus the fraction μ_V/μ_F. The dashed lines corresponds to the recent experimental bounds and the red triangle to the SM value. On the left side we show the full sample and on the right side the parameter points, which provide an SFOEWPT with the whole sample as grey background. The colour code indicates again the relative frequency normalized to the largest bin. In the N2HDM the experimental bounds (dashed lines in Fig. 6.8) of the μ_V/μ_F rate can be significantly tightened, if all applied theoretical and experimental constraints are taken into account. The $\mu_{\gamma\gamma}$ rate can take all values which are still allowed by the experimentel bounds. A factor of 1.56 is still possible in the N2HDM. On the other side the SFOEWPT shrinks the possible ranges significantly. The upper bound of $\mu_{\gamma\gamma}$ decreases down to 1.04, while the fraction μ_V/μ_F is less strictly constrained by the SFOEWPT. Overall the tendency is still towards to the SM value, such that the signal rates of the N2HDM are still compatible with the SM, but the SFOEWPT tightens the possible phase space. This statement holds also for the other promising decay channels of the SM-like Higgs boson, $\mu_{\tau\tau}$ and μ_{VV}, in Fig. 6.9. Applying the SFOEWPT reduces the upper bounds slightly, but it is still compatible with the SM value.

To conclude the discussion of the signal rates in type I and M_1 of the N2HDM

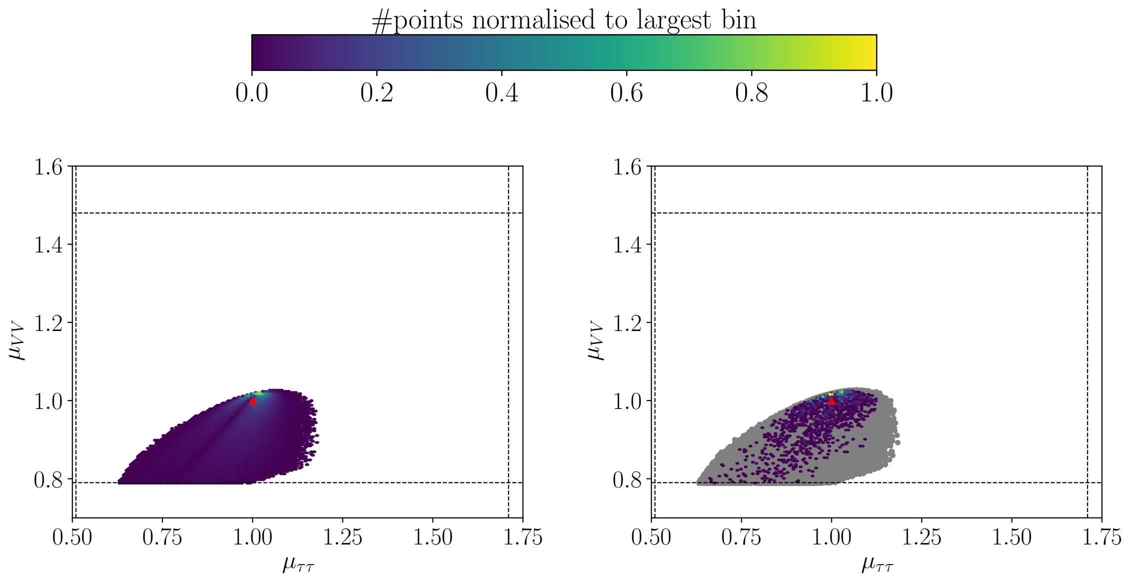

(a) (b)

Figure 6.9: Type I and mass order M_1: $\mu_{\tau\tau}$ versus μ_{VV}. Left: the ScannerS sample with all parameter points fulfilling theoretical and experimental constraints; right: Grey points correspond to the ScannerS sample and the coloured points provide an SFOEWPT. The colour code denotes the relative frequency normalized to the largest bin.

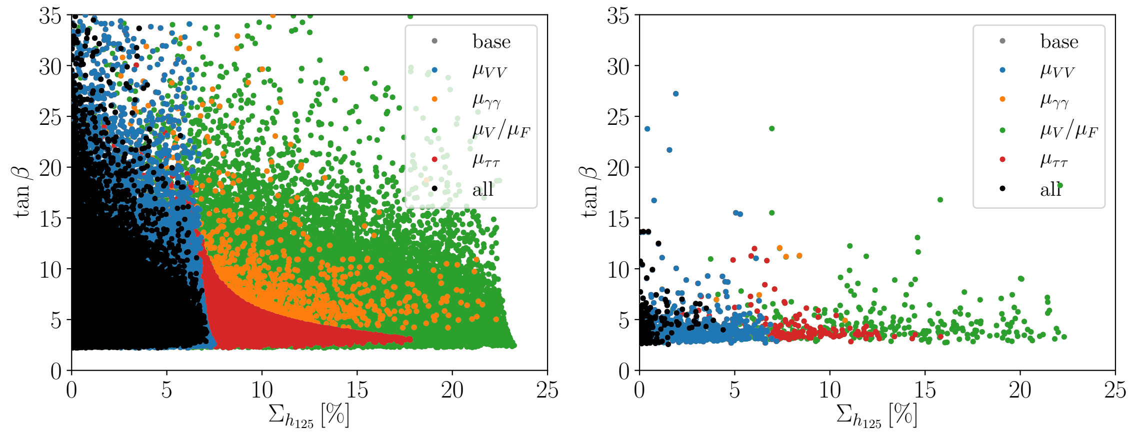

(a) (b)

Figure 6.10: Type I and mass order M_1: Singlet admixture $\Sigma_{h_{125}}$ as a function of $\tan\beta$ and the precision in the μ-values. The color code denotes the μ-values within 5% of the SM reference where *base* denotes the ScannerS sample. The whole sample with theoretical and experimental constraints (left) and the parameter points, which provide an SFOEWPT (right).

we investigate the constraining power of the measurement of every particular decay channel towards the singlet admixture and $\tan\beta$. In Fig. 6.10 the singlet admixture $\Sigma_{h_{125}}$ to SM-like Higgs boson versus $\tan\beta$ is displayed. The singlet admixture to the SM-like Higgs boson is given by

$$\Sigma_{h_{125}} = R_{i3}^2 \tag{6.8}$$

where i corresponds to the CP-even Higgs boson which denotes the SM-like Higgs boson[1]. The colour code indicates a possible measurement of the respective decay channel within 5% of the SM value. In [51] the authors conclude, that for the type I model the decay channel $h_{125} \to ZZ$ is the most promising channel to constraint the singlet admixture, as one can see in Fig. 6.9a (blue points). Requiring a 5% precise measurement in all decay channels hardly improves the constraint on $h_{125} \to ZZ$. On the other side, if one requires an SFOEWPT the upper bound on the singlet admixture shrinks from around 8% down to 5% taking into account the combination of all decay channels. The measurement of μ_{VV} is still the most constraining channel, but combining all decay channels in addition of the SFOEWPT has indeed some effects on the bounds. To obtain a constraint on $\tan\beta$ in combination with an SFOEWPT, the channels $h_{125} \to \gamma\gamma$ and $h_{125} \to \tau\tau$ (orange and red points) are promising. Within a 5% range of the SM value they allow $\tan\beta$ in a range of 2.3 up to 13.

6.2.2 Mass order M_1 and Type II

To continue the discussion of the implications of the SFOEWPT, the type II N2HDM for the mass order M_1 is presented. We start again with the phenomenology of the non-SM masses. In Fig. 6.11 the mass plane m_A versus $m_\downarrow$ is shown. We already mentioned in Sec. 6.1 the phenomenologically interesting parameter space $m_A \lesssim 340$ GeV. These points have a significant branching ratio in the decay channel $A \to Zh_{125}$. The requirement of NLO vacuum stability started to tighten the constraints on those points, but the SFOEWPT excludes them almost in total. Only one point with a mass of $m_A = 321.4$ GeV survives the SFOEWPT requirement, which provides a branching of $\mathrm{BR}_{A\to Zh_{125}} \approx 32\%$. Comparing both density distributions in Fig. 6.11a and Fig. 6.11b one observes an overall tendency towards smaller CP-even scalar masses $m_\downarrow$ and pseudoscalar masses around 600 GeV. The red line denotes again the mass relation $m_A = m_\downarrow + m_Z$. As noticed in type I the SFOEWPT favors scenarios with $A \to Zh_{125}$ as promising channel, but nevertheless the N2HDM still allows phase space besides this consideration.

Turning to the mass plane $m_A - m_{H^\pm}$ versus $m_\downarrow - m_{H^\pm}$ in Fig. 6.12 the SFOEWPT favors a mass gap between $m_\downarrow$ and $m_{H^\pm}$ around 200 GeV, but at the same time excludes very large gaps beyond 600 GeV. Only few scenarios with $m_\downarrow \geq m_{H^\pm}$ survive the SFOEWPT check, such that again larger charged masses are favored. A more significant change can be observed in the mass plane $m_A - m_{H^\pm}$ versus $m_\uparrow - m_{H^\pm}$

[1] The corresponding index i can be obtained by considering the mass order: $i = 1$ for the mass order M_1, $i = 2$ for M_2 and $i = 3$ for M_3.

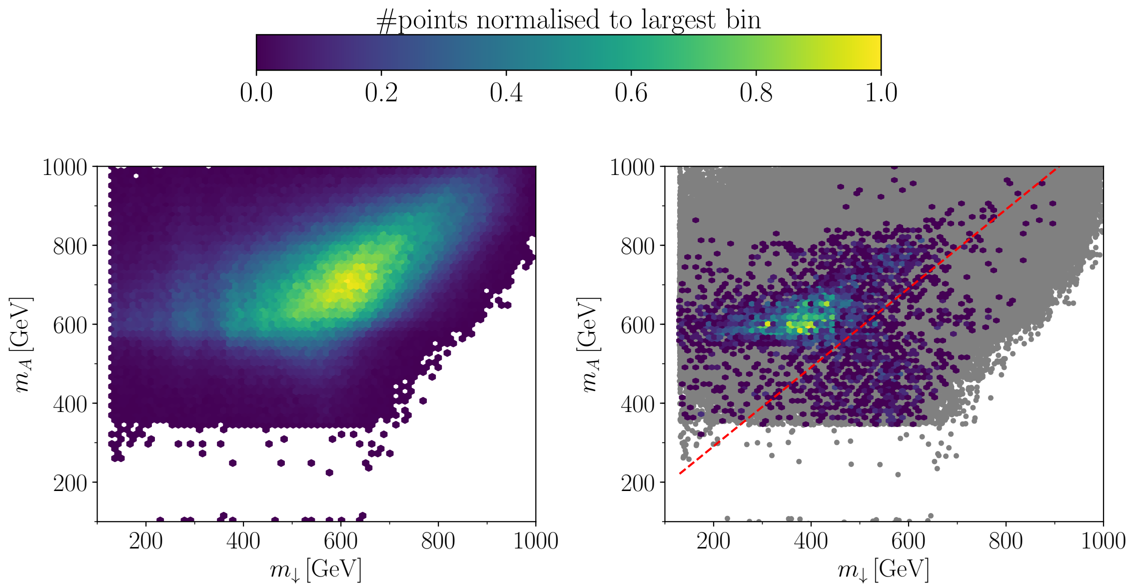

(a) (b)

Figure 6.11: Type II and mass order I: The mass plane $m_\downarrow$ versus m_A. Left: The ScannerS sample fulfilling theoretical and experimental constraints; right: Grey points correspond to the ScannerS sample and the coloured points provide an SFOEWPT. The colour code shows the relative frequency normalized to the largest bin. The red line on the right plot denotes the mass relation $m_A = m_\downarrow + m_Z$.

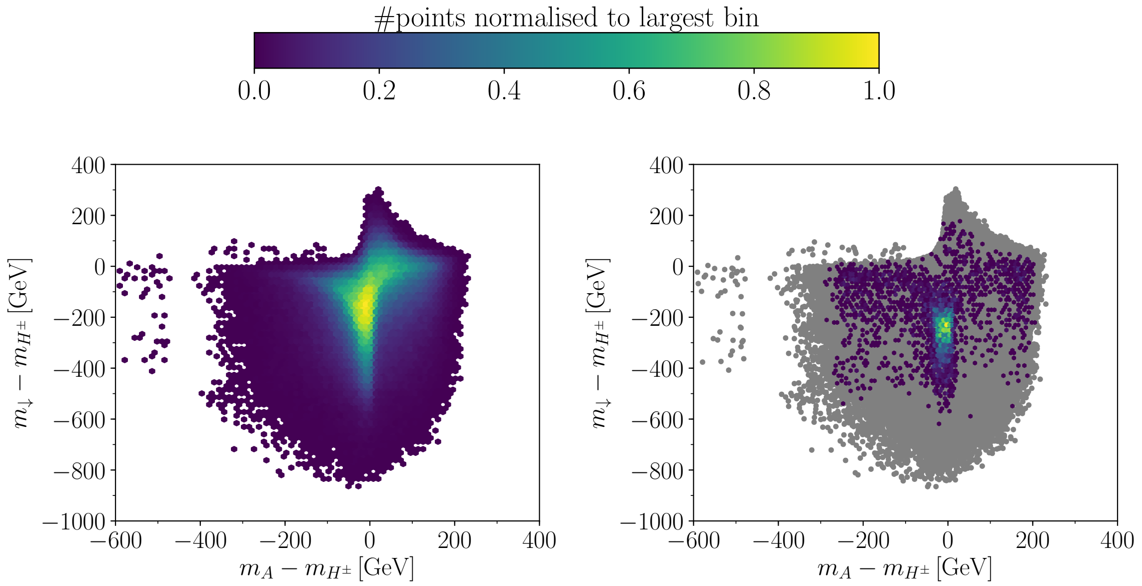

(a) (b)

Figure 6.12: Type II and mass order M_1: The mass differences $m_A - m_{H^\pm}$ versus $m_\downarrow - m_{H^\pm}$. Left: The ScannerS sample fulfilling theoretical and experimental constraints; right: Grey points correspond to the ScannerS sample and the coloured points provide an SFOEWPT. The colour code shows the relative frequency normalized to the largest bin.

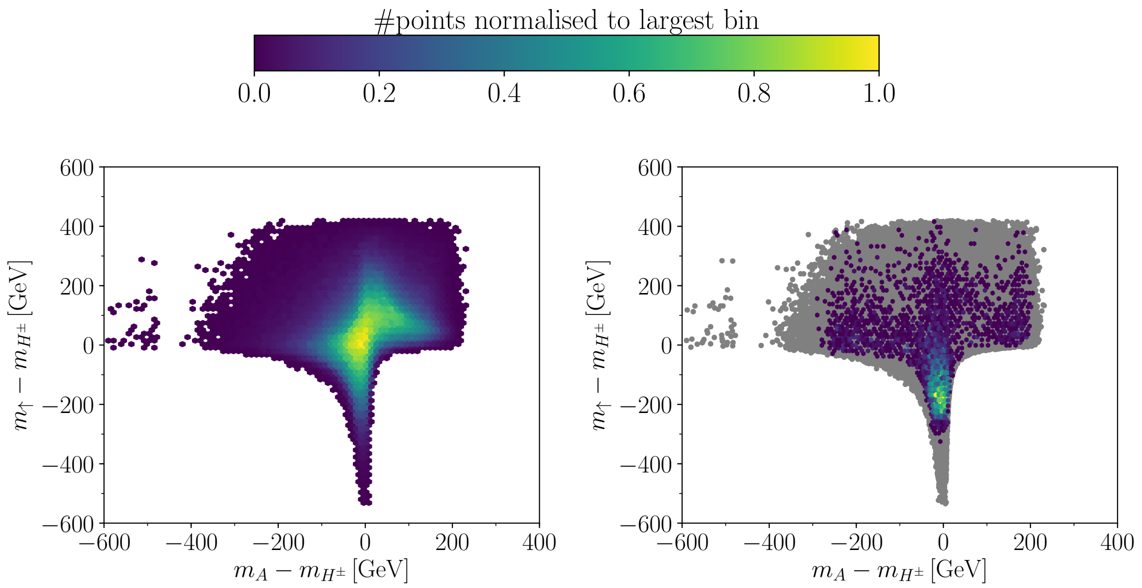

(a) (b)

Figure 6.13: Type II and mass order M_1: The mass differences $m_A - m_{H^\pm}$ versus $m_\uparrow - m_{H^\pm}$. Left: The ScannerS sample fulfilling theoretical and experimental constraints; right: Grey points correspond to the ScannerS sample and the coloured points provide an SFOEWPT. The colour code shows the relative frequency normalized to the largest bin.

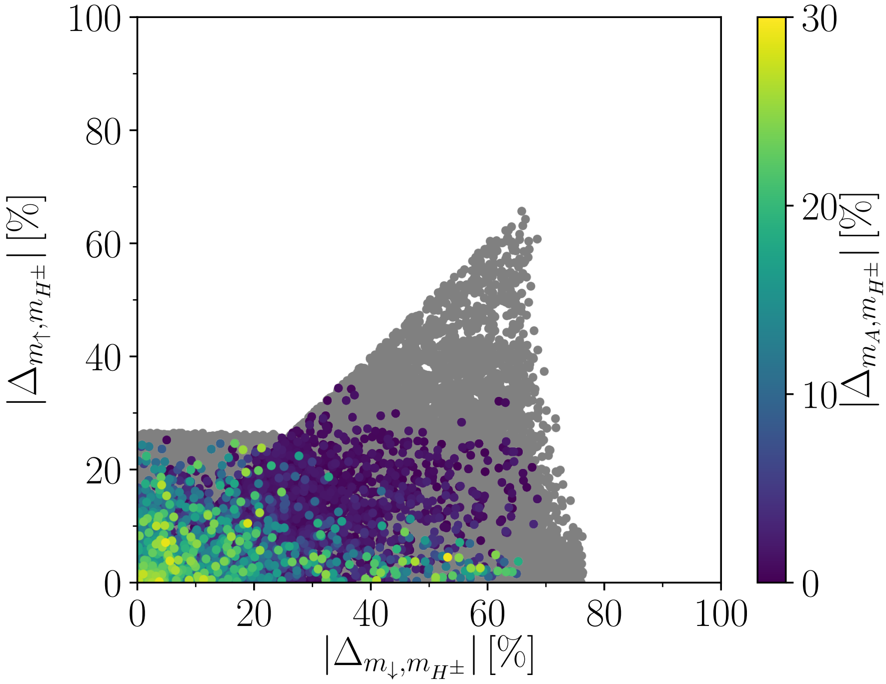

Figure 6.14: Type I and mass order M_1: The mass asymmetries of all non-SM Higgs bosons in the N2HDM compared the charged Higgs boson mass. Grey points correspond to the ScannerS sample and coloured points provide an SFOEWPT.

in Fig. 6.13. While the theoretical and experimental constraints force the masses to be close to each other, the SFOEWPT favors a mass gap between $m_\uparrow$ and $m_{H^\pm}$ around 200 GeV.

One significant difference with respect to the type I model is, that the mass asymmetries $\Delta_{m_\uparrow,m_{H^\pm}}$ and $\Delta_{m_A,m_{H^\pm}}$ are larger compared to the type I case. They are at most 35% if one requires an SFOEWPT, as can be inferred from Fig. 6.14. Due to the already heavy charged mass $m_{H^\pm} \gtrsim 580$ GeV [72] a mass degeneracy with $m_\downarrow$ would imply an even heavier $m_\uparrow$. On the other side, the overall tendency of the SFOEWPT is to have smaller CP-even non-SM Higgs boson masses, so that a mass asymmetry $\Delta_{m_\uparrow,m_{H^\pm}}$ up to 35% is observed. Since a mass degeneracy between m_A and $m_{H^\pm}$ is favored by the SFOEWPT, the pseudoscalar mass is forced to larger values so that the exclusion of the mass region $m_A \leq 340$ GeV can be explained.

Heading towards the signal rates for type II, we compare the same signal rates as in type I. Starting with $\mu_{\gamma\gamma}$ versus μ_V/μ_F in Fig. 6.15, we observe that the SFOEWPT tighten the upper and lower bounds on the signal rates in both cases

$$\mu_{\gamma\gamma} \in [0.68, 1.49] \Longrightarrow [0.72, 1.32] \tag{6.9}$$

$$\mu_V/\mu_F \in [0.53, 1.27] \Longrightarrow [0.72, 1.17] \;. \tag{6.10}$$

Although the SM value is not contained in the density distribution of the parameter points with SFOEWPT, the overall tendency of the PT is towards the SM value. In Fig. 6.16 we show the signal rate into τ leptons versus the signal rate μ_{VV}. To have a

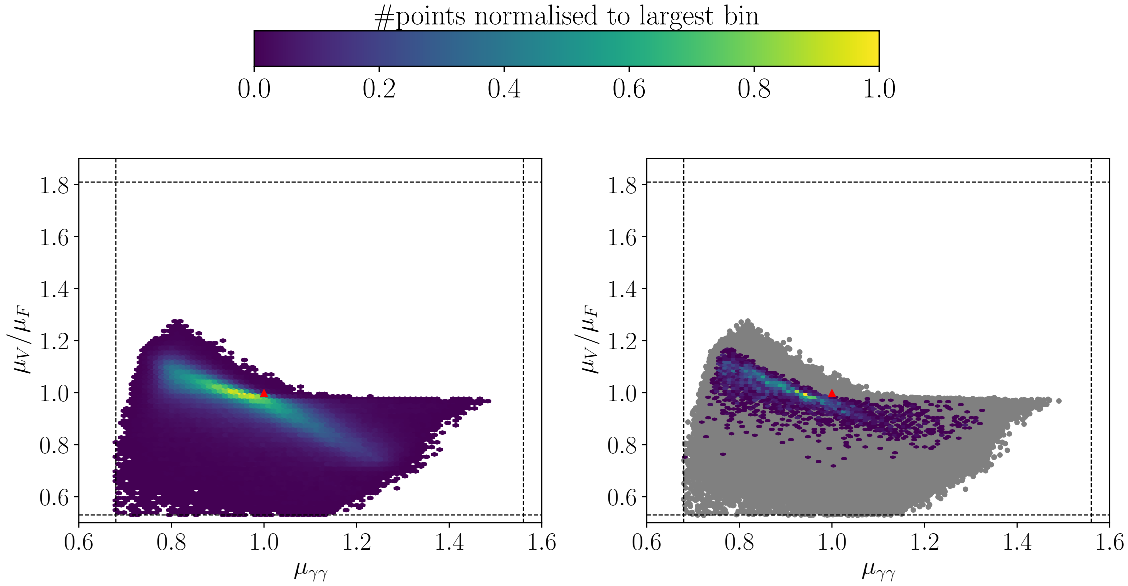

(a) (b)

Figure 6.15: Type II and mass order M_1: $\mu_{\gamma\gamma}$ versus μ_V/mu_F. Left: the ScannerS sample with all parameter points fulfilling theoretical and experimental constraints; right: Grey points correspond to the ScannerS sample and the coloured points provide an SFOEWPT. The colour code denotes the relative frequency normalized to the largest bin.

consistent comparison with [51], we discuss the three different regions with enhanced $\mu_{\tau\tau}$ separately. The largest enhancement in $\mu_{\tau\tau}$ is obtained for simultaneously enhanced μ_{VV}. This can be explained by the production mechanism and corresponds to the enhanced couplings to top quarks [51]. In this region the PT tightens quite significantly the constraints on $\mu_{\tau\tau}$ down to $\mu_{\tau\tau} \leq 1.14$, while the theoretical and experimental constraints allow $\mu_{\tau\tau} \leq 1.34$. The 2HDM-like region in Fig. 6.16 with enhanced $\mu_{\tau\tau}$ but reduced μ_{VV} is quite compatible with the SFOEWPT. The parameter points with enhanced $\mu_{\tau\tau}$ and $\mu_{VV} \approx 1$ are attributed to the *wrong sign regime*, which we will discuss in detail later on.

Considering future collider studies allowing for the measurement of the signal rates within a 5% precision of the SM value, we compare the constraining power of each particular decay channel of h_{125} towards the singlet admixture. In Fig. 6.17 the singlet admixture to the SM particle versus $\tan\beta$ is shown. The colour codes indicates again the decay channel, which provides a measurement within 5% of the SM signal rate. $\mu_{\tau\tau}$ constrains (red points) the singlet admixture at most stricly for larger $\tan\beta$, while allowing up to 22% for small $\tan\beta$. Nevertheless the measurement of $h_{125} \to \tau\tau$ allows to reduce the bounds on the admixture most efficiently. Combining all signal rates and the SFOEWPT one can set an upper bound on the singlet admixture from 12% (without the SFOEWPT) down to 8%. Therefore it can be concluded that although it is assumed that the measurement of the signal rates allows only a deviation of 5% compared to the SM, it is still possible to have a significant admixture up to 8% of the singlet to the h_{125}.

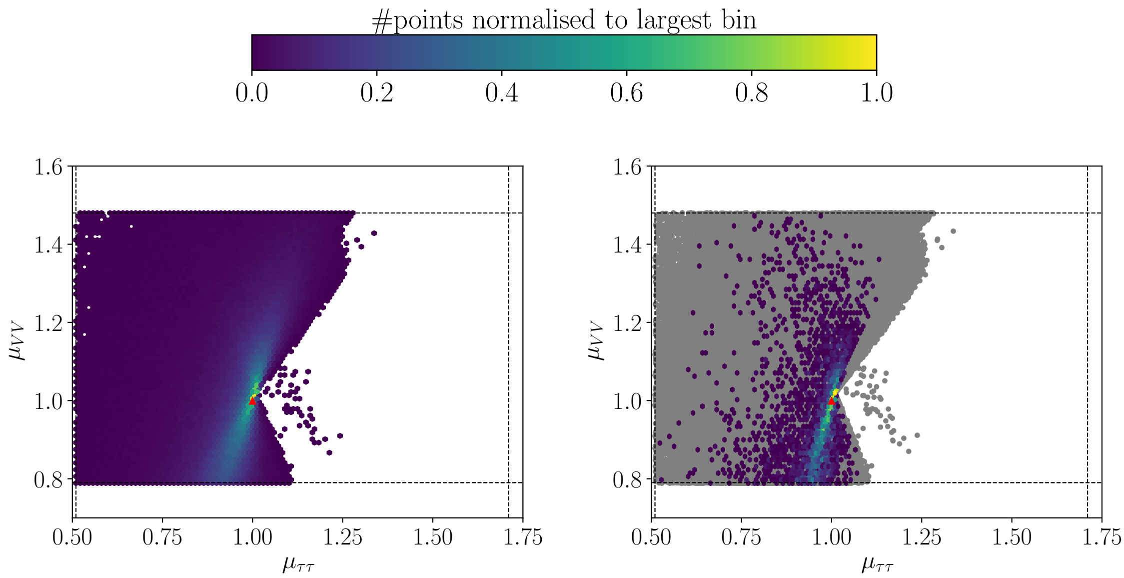

(a) (b)

Figure 6.16: Type II and mass order M_1: $\mu_{\tau\tau}$ versus μ_{VV}. Left: the ScannerS sample with all parameter points fulfilling theoretical and experimental constraints; right: Grey points correspond to the ScannerS sample and the coloured points provide an SFOEWPT. The colour code denotes the relative frequency normalized to the largest bin.

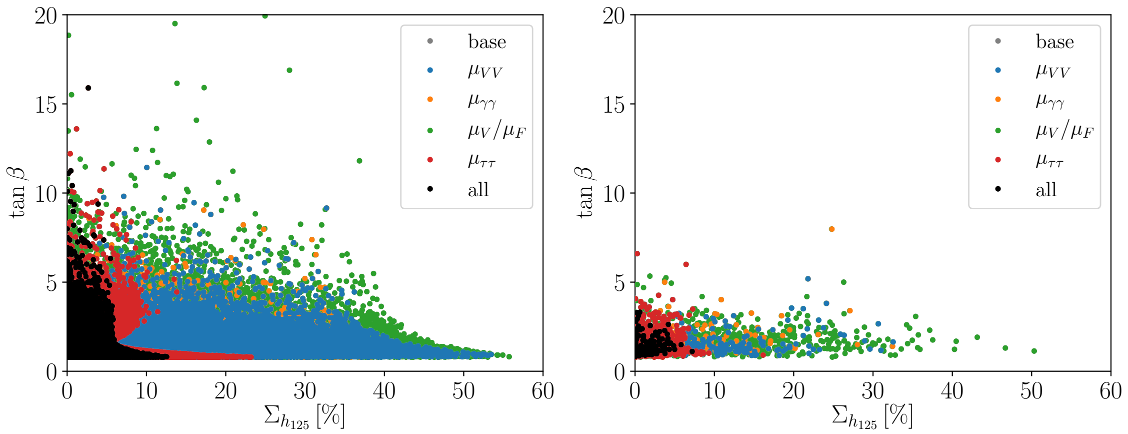

(a) (b)

Figure 6.17: Type II and mass order M_1: Singlet admixture $\Sigma_{h_{125}}$ as a function of $\tan\beta$ and the precision in the μ-values. The color codes denotes the μ-values within 5% of the SM reference where *base* denotes the ScannerS sample. The whole sample with theoretical and experimental constraints (left) and the parameter points, which provide an SFOEWPT(right).

6.2.2.1 Wrong sign limit

One interesting phenomenological scenario is the so called *wrong sign limit* [81]. In this scenario the coupling of the h_{125} to the gauge bosons normalised to the SM value has an opposite sign with respect to the coupling of h_{125} to the bottom-quark normalised to the SM value. In contrast to the SM, this is possible in the N2HDM. The wrong sign limit has some consequences like the non-decoupling of heavy particles, which are discussed in [82, 83] for the 2HDM. The implications for the N2HDM are presented in [51]. For the type I N2HDM the wrong sign limit cannot be realised, due to the fact, that the up- and down-type couplings to the fermions are the same and therefore different signs requires $\tan\beta < 1$, which is excluded by experiment. For the type II N2HDM, there exists a still allowed phase space with an opposite sign in the Yukawa coupling to down-type fermions with respect to the coupling to gauge bosons. This requires $\sin\alpha > 0$ in the 2HDM and to obtain the 2HDM limit from the N2HDM, a redefinition of the mixing angles is needed in the following way

$$N2HDM \to 2HDM \Longleftrightarrow \begin{cases} \alpha_1 \to \alpha + \frac{\pi}{2} \\ \alpha_2 \to 0 \\ \alpha_3 \to 0\,. \end{cases} \tag{6.11}$$

In this way the N2HDM can be seen as a real CP-conserving 2HDM plus a decoupled singlet extension. To match the convention of [51], we chose

$$\mathrm{sgn}\left(c(h_{125}VV)\right) \cdot \sin\left(\alpha_1 - \frac{\pi}{2}\right) > 0 \tag{6.12}$$

as the condition for the wrong sign limit. In Fig. 6.18 the wrong sign regime discriminator versus $\tan\beta$ is shown. We show all parameter points provided by ScannerS as grey points and the coloured points indicate the parameter points which provide an SFOEWPT. The colour code denotes the strength of the phase transition. As can inferred in Fig. 6.18 the phase space with positive $\mathrm{sgn}\left(c(h_{125}VV)\right) \cdot \sin\left(\alpha_1 - \frac{\pi}{2}\right)$ is excluded by the SFOEWPT, so that we do not find any allowed phase space point within the wrong-sign regime. In addition, the SFOEWPT reduces $\tan\beta$ quite significantly from $\tan\beta = 19.9$ to $\tan\beta = 8.0$.

6.2.3 Mass order M_2

Turning to the mass order M_2 in which the mass of the mass eigenstate $h_\downarrow$ is smaller than the SM-like Higgs boson mass of 125.09 GeV, the corresponding sample sizes can be seen in Table 6.1. The sample sizes of parameter points providing a sufficient SFOEWPT in the mass order M_2 are less than 100 points in both N2HDM types. Due to the immense computation time required by the numerical analysis, the sample size was limited to the noted amount. In Fig. 6.19 the mass asymmetries of all non-SM Higgs bosons compared to the charged Higgs boson mass are displayed for the type I N2HDM. On the axes, we show $\Delta_{m_\downarrow,m_{H^\pm}}$ and $\Delta_{m_\uparrow,m_{H^\pm}}$ defined in

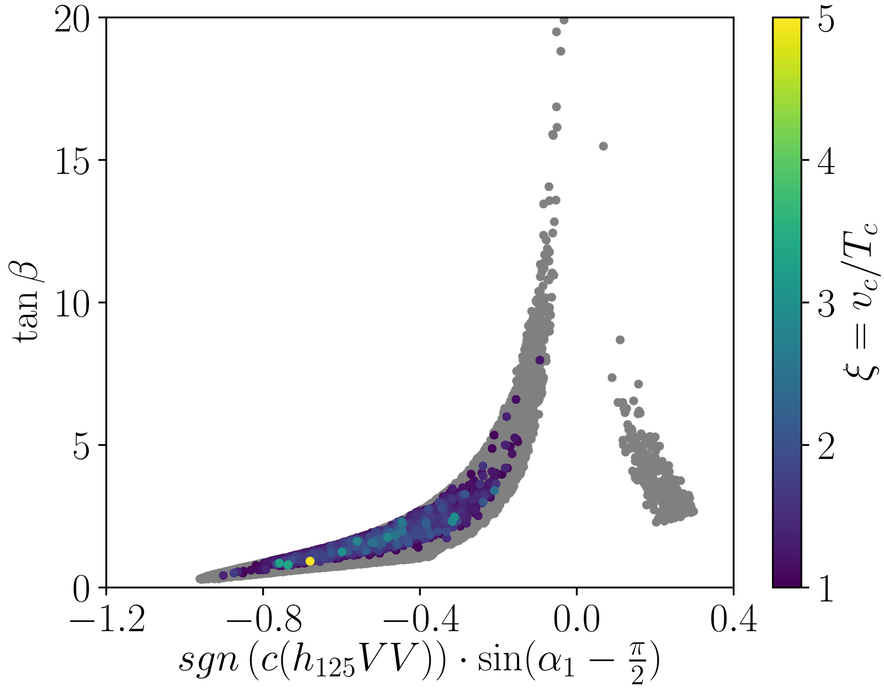

Figure 6.18: Type II and mass order M_1: Wrong sign regime discriminator versus $\tan\beta$. The colour code shows the strength of the phase transition. Grey points passed the experimental and theoretical constraints and coloured points provide an SFOEWPT.

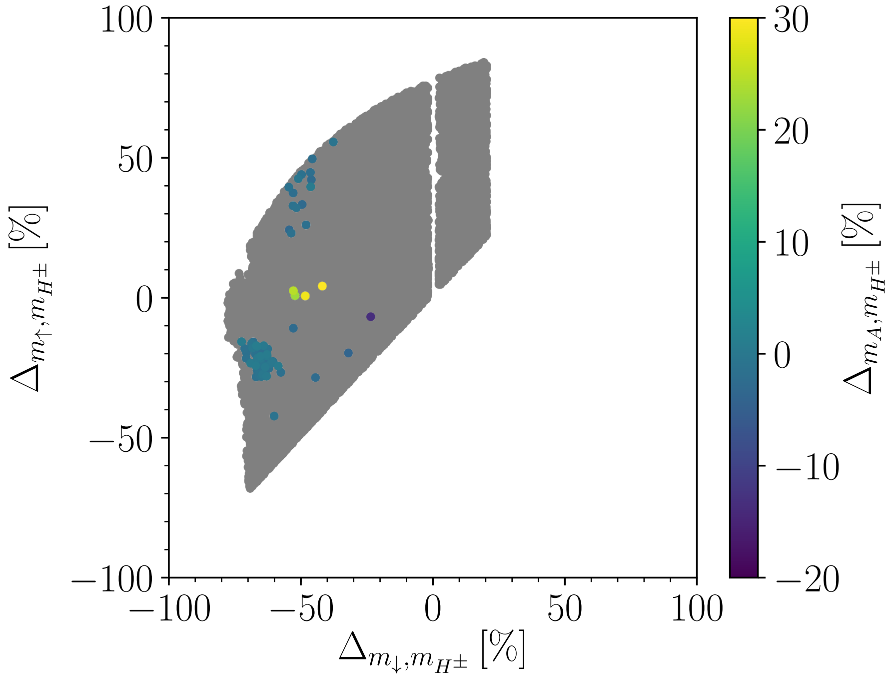

Figure 6.19: Type I Mass order M_2: The mass asymmetries of the non-SM Higgs bosons compared to the charged Higgs mass. On the axis $\Delta_{m_\downarrow,m_{H^\pm}}$ versus $\Delta_{m_\uparrow,m_{H^\pm}}$ and the colour code indicates the mass asymmetry $\Delta_{m_A,m_{H^\pm}}$, for the definition see Eq. (6.7).

Eq. (6.7), and the colour code shows $\Delta_{m_A,m_{H^\pm}}$. As already mentioned in the type I M_1 discussion, two scenarios in the mass configuration can be observed by requiring an SFOEWPT. Most of the points have $m_A \approx m_{H^\pm}$ and a mass gap in the range $\Delta_{m_\downarrow,m_{H^\pm}} \in [-70,-50]\,\%$. This implies that $m_\downarrow$ is significantly smaller than the charged mass. In this scenario the mass gap between $m_\uparrow$ and $m_{H^\pm}$ can be $\gtrsim 25\%$ or $\lesssim -20\%$ so that both cases- a heavier $h_\uparrow$ or a heavier $H^\pm$ - can be realized. The five points (four yellows and one dark blue point) with a non-zero $\Delta_{m_A,m_{H^\pm}}$ in Fig. 6.19 have a $\Delta_{m_\uparrow,m_{H^\pm}}$ close to zero. Four of them (yellow) have a larger pseudoscalar mass and only one point (dark blue) provides a slightly heavier charged mass compared to the pseudoscalar. The mass degeneracy between $h_\downarrow$ and $H^\pm$ is already excluded by theoretical and experimental constraints.

In Fig. 6.20 the same configuration for the type II N2HDM is shown. Again the mass degeneracy of $m_\downarrow$ and $m_{H^\pm}$ is already not valid anymore due to the experimental and theoretical constraints. Points with $m_A \approx m_{H^\pm}$ have a mass gap between $m_\uparrow$ and $m_{H^\pm}$ around 200 GeV. In the type II N2HDM this mass scenario ($m_A \approx m_{H^\pm}$) implies that the charged mass is greater than $m_\uparrow$. Due to the flavour constraints $B \to X_s\gamma$ the charged mass is forced to be $m_{H^\pm} \geq 580$ GeV so that $m_\uparrow \geq m_{H^\pm}$ would imply very large CP-even scalar masses which are disfavored by the PT.

For the mass degeneracy of $m_\uparrow$ and $m_{H^\pm}$ both cases ($m_A \geq m_{H^\pm}$ and $m_A \leq m_{H^\pm}$) are possible. Due to the already very large charged mass, the asymmetry $\Delta_{m_A,m_{H^\pm}}$ lies in the smaller interval $\approx \pm 15\%$ compared to the type I N2HDM.

Coming to the signal rates for this mass configuration, no significant changes are

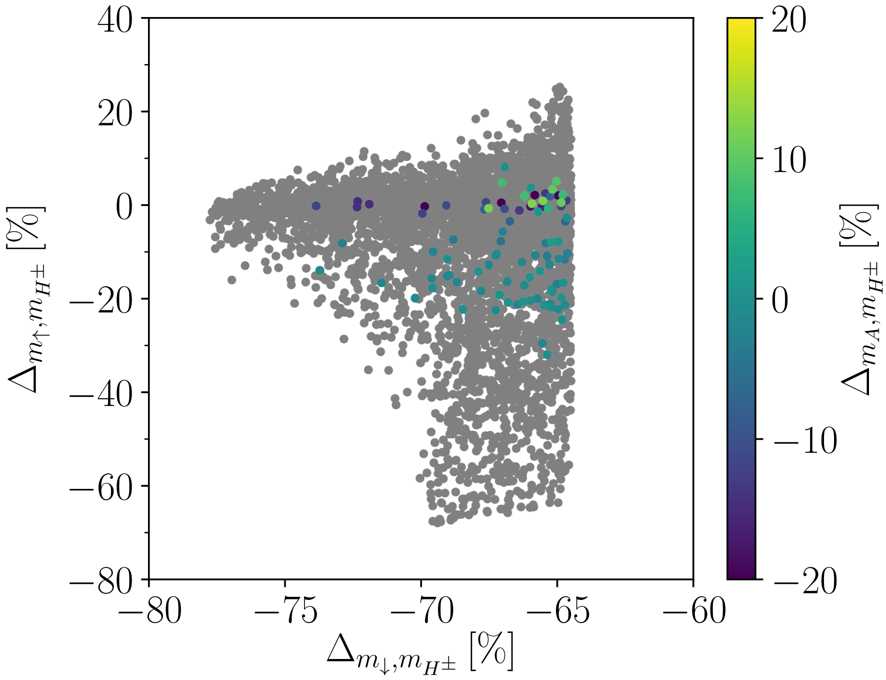

Figure 6.20: Type II Mass order M_2: The mass asymmetries of the non-SM Higgs compared to the charged Higgs mass. On the axis $\Delta_{m_\downarrow,m_{H^\pm}}$ versus $\Delta_{m_\uparrow,m_{H^\pm}}$ and the colour code indicates the mass asymmetry $\Delta_{m_A,m_{H^\pm}}$, for the definition see Eq. (6.7).

observable. All statements in the N2HDM M_1 discussion (both types) coincide with the observations in M_2.

6.2.4 Mass order M_3

To end the discussion of the different mass orders the mass hierarchy $m_\downarrow \leq m_\uparrow \leq m_{h_{125}}$ is considered. In this scenario the two non-SM Higgs bosons are lighter than the SM-like Higgs boson h_{125}. In the type I model we have a sample of 3677 points which fulfill theoretical and experimental constraints. As can inferred from Table 6.1, around 46% of these points provide a stable electroweak vacuum at NLO and only a small amount of the points are lost due to the NLO unitarity constraint. In this mass order there are large mass gaps between the pseudoscalar and the CP-even Higgs bosons, so that the NLO corrections might get large. Therefore the NLO stability of the electroweak vacuum is not guaranteed. Applying the SFOEWPT on these remaining parameter points reduces the size of the sample to one single point. The parameter point can be read off from Table 6.2. The pseudoscalar and charged mass are close to each other while the CP-even scalar masses are significantly smaller. This mass configuration can be observed in the type I M_1as well. Due to the small $\alpha_{1,2}$ and $\alpha_3 \approx \frac{\pi}{2}$ the singlet contribution to h_{125} is almost decoupled and attributed to the $h_2 = h_\uparrow$ state which results in the high singlet admixture $\Sigma^S_{h_\uparrow}$. The large $\tan\beta$ allows for a small mass of the $h_1 = h_\downarrow$ state. All the signal rates are compatible with

$m_\downarrow$ [GeV]	$m_\uparrow$ [GeV]	m_A [GeV]	$m_{H^\pm}$ [GeV]	v_S [GeV]	$\tan\beta$	m_{12}^2 [GeV^2]
97.7	105.7	215.2	227.3	1437.3	27.8	334.6
	α_1	α_2	α_3	$\Sigma^S_{h_\uparrow}$	$\Sigma^S_{h_{125}}$	
	-0.108	-0.196	1.494	0.56%	95.7%	
μ_V/μ_F	$\mu_{\gamma\gamma}$	μ_{VV}	$\mu_{\tau\tau}$	ξ_C	T_C [GeV]	v_C [GeV]
0.99	0.89	1.0	1.0	1.75	112.5	196.8

Table 6.2: Type I M_3: The single parameter point in the mass order M_3which provides an SFOEWPT.

BR(h_{125})	BR($h_{125} \to bb$) = 59.0%	BR($h_\downarrow$)	BR($h_\downarrow \to bb$) = 80.0%
	BR($h_{125} \to WW$) = 21.0%		BR($h_\downarrow \to WW$) = 0.32%
	BR($h_{125} \to \tau\tau$) = 6.3%		BR($h_\downarrow \to \tau\tau$) = 8.3%
	BR($h_{125} \to \gamma\gamma$) = 0.21%		BR($h_\downarrow \to \gamma\gamma$) = 0.04%
BR($H^\pm$)	BR($H^\pm \to W^\pm h_\downarrow$) = 96.3%	BR($h_\uparrow$)	BR($h_\uparrow \to bb$) = 77.3%
	BR($H^\pm \to W^\pm h_\uparrow$) = 3.1%		BR($h_\uparrow \to WW$) = 3.2%
	BR($H^\pm \to W^\pm h_{125}$) = 0.1%		BR($h_\uparrow \to \tau\tau$) = 8.0%
BR(A)	BR($A \to Zh_\downarrow$) = 97.6%		BR($h_\uparrow \to \gamma\gamma$) = 0.19%

Table 6.3: Type I and mass order M_3: Branching ratios of the point given in Table 6.2

the SM, only the $\gamma\gamma$ rate is slightly decreased compared to the SM.
Concerning the branching ratios of the CP-even Higgs bosons in Table 6.3, it can be observed that the decay in two bottom quarks is the most dominant channel for all neutral CP-even Higgs bosons. Due to the small masses of the CP-even non-SM Higgs bosons, the branching into two W bosons is substantially decreased compared to the SM-like Higgs boson h_{125}. Beside this difference the decay channels of the CP-even Higgs bosons are hard to distinguish. The pseudoscalar and charged Higgs bosons mainly decay in the corresponding $h_\downarrow$ channel so that the SM-like decay channels almost do not contribute to their decay channels.
In the type II M_3 N2HDM we do not find any valid parameter point which provides an SFOEWPT, because the requirement of a stable NLO electroweak vacuum already excludes the whole phase space, as can be inferred in Table 6.1.

6.3 Triple Couplings of the Massive Particles

One of the last unknown properties of the SM-Higgs boson is the trilinear self-coupling. The measurement of this quantity would allow an insight in the electroweak symmetry breaking mechanism [84] and could lead to a deeper understanding of the physics beyond the SM. In this context we calculate the trilinear self-couplings at zero temperature from the effective potential approach according to

$$\lambda^{NLO}_{\phi_i\phi_j\phi_k} \equiv -\partial^3_{ijk}V_{eff} = -\left(\partial^3_{ijk}V_{tree} + \partial^3_{ijk}V_{CW} + \partial^3_{ijk}V_{CT}\right) . \tag{6.13}$$

Note that, V_T does not contribute, due to the fact that the couplings are calculated at zero temperature. The Coleman-Weinberg contribution is given by [54] and implemented in our program. The calculated values are compared to the SM NLO value which is given by [85]

$$\lambda^{NLO}_{hhh}(SM) = -\frac{3m_h^2}{v}\left[1 - \frac{N_c}{3\pi^2}\frac{m_t^4}{v^2m_h^2}\left\{1 + \mathcal{O}\left(\frac{m_h^2}{m_t^2}, \frac{p_i^2}{m_t^2}\right)\right\}\right] . \tag{6.14}$$

For the following discussion of the results, we note that the strength of the SFOEWPT increases with the size of the couplings of the light Higgs bosons to the SM-like Higgs boson and decreases with the Higgs boson mass [19]. Since all CP-even neutral Higgs bosons receive a VeV through mixing and hence contribute to the phase transition, an SFOEWPT requires the participating Higgs bosons either to be light or to have an electroweak VeV contribution close to zero [86]. To discuss further implications with respect to the SFOEWPT, a new quantity is introduced, the *doublet admixture*

$$\Sigma_i^D = R_{i1}^2 + R_{i2}^2 \equiv 1 - \Sigma_i^S , \tag{6.15}$$

where R_{ij} is the mixing matrix defined in Eq. (3.18). This quantity describes the percentage of the two doublets to the mass eigenstate. Since the different mass orders M_1, M_2 and M_3 do not show significant differences in their trilinear self-couplings, we show only the results for the first mass order M_1. In this mass hierarchy we have the most parameter points which allows for a sufficient discussion of the phenomenology.

6.3.1 Type I: M_1

In Fig. 6.21 the relative distribution of the tree level versus the NLO trilinear self-coupling between three h_{125}, both normalized to the SM value, is displayed. The theoretical and experimental constraints allow enhanced NLO trilinear self-couplings by a factor of 15, but are significantly decreased by the SFOEWPT. Nevertheless it is remarkable, that the NLO couplings are enhanced by a factor of 2.5. In addition, the SFOEWPT requires a non-zero h_{125} self-coupling. Note that, an SFOEWPT needs enhanced self-couplings, but on the other side the scalar particle spectrum participating to the PT should not become too heavy, thus restricting the size of the quartic coupling parameters in the Higgs potential. Therefore the NLO corrections

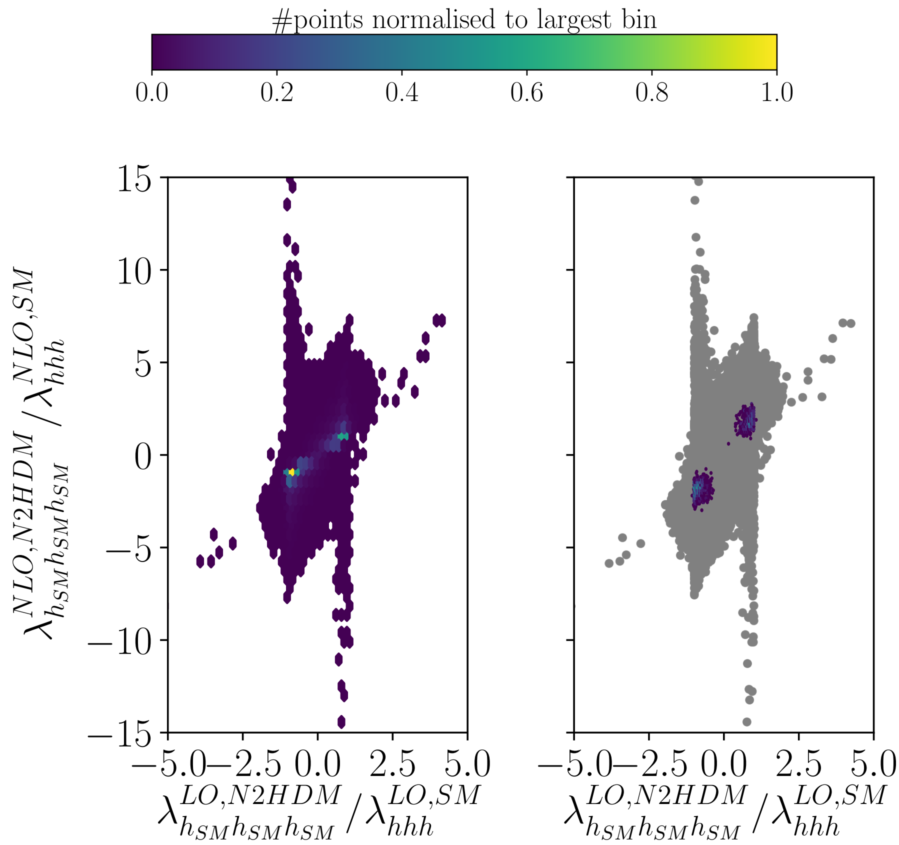

Figure 6.21: Type I and mass order M_1: The tree level trilinear self-coupling of the h_{125} versus the NLO trilinear self-coupling of h_{125} both normalized to the SM value. Left: the ScannerS sample with all parameter points fulfilling theoretical and experimental constraints; right: Grey points correspond to the ScannerS sample and the coloured points provide an SFOEWPT. The colour code denotes the relative frequency normalized to the largest bin.

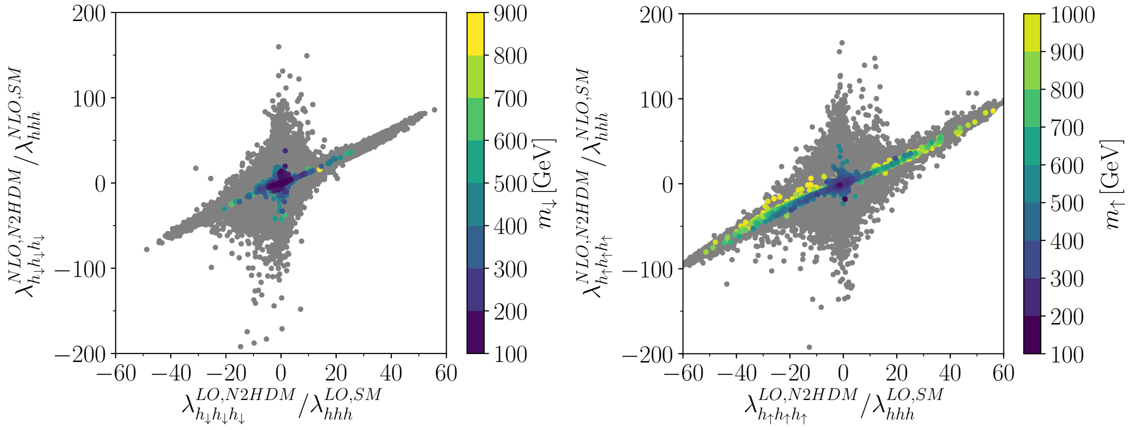

(a) (b)

Figure 6.22: Type I and mass order M_1: The tree level trilinear self-coupling of $h_\downarrow$(left) and $h_\uparrow$(right) versus the NLO trilinear self-coupling of $h_\downarrow$(left) and $h_\uparrow$(right) both normalized to the SM value. The colour code indicates $m_\downarrow$(left) and $m_\uparrow$ (right). The grey points denote the full ScannerS sample, while the coloured points provide an SFOEWPT.

to the trilinear self-couplings are reduced with respect to the maximum enhancement compatible with the theoretical and experimental constraints.

Considering all other possible combinations of trilinear couplings in the N2HDM, we observe that the trilinear self-couplings can be supressed or substantially enhanced compared to the SM value. For further examples of trilinear couplings, we show the self-couplings between three $h_\downarrow$ and $h_\uparrow$, respectively the leading-order versus the NLO self-couplings $\lambda_{h_\downarrow h_\downarrow h_\downarrow}$, $\lambda_{h_\uparrow h_\uparrow h_\uparrow}$ are shown in Fig. 6.22. The colour code denotes the mass of the corresponding particle. Apart from a few exceptions, the parameter points providing an SFOEWPT lie on a straight line, so that one can conclude that the NLO trilinear self-coupling is enhanced approximately by a factor of two compared to the leading-order self-coupling in these scenarios. However, the maximum of the NLO self-couplings compatible with the applied constraints is reduced by considering the SFOEWPT. Bearing in mind that the CP-even neutral Higgs bosons either are light or acquire an electroweak VeV close to zero, in order not to weaken the PT, we investigate the heaviest CP-even neutral Higgs boson $h_\uparrow$. In Fig.6.23 the doublet admixture of $h_\uparrow$ versus the NLO trilinear self-coupling normalized to the SM value is displayed. The colour code indicates $m_\uparrow$. Significantly enhanced NLO couplings are observed up to a doublet admixture of 25%. In this region the $h_\uparrow$ state does not contribute significantly to the VeV and at the same time there are also the largest masses. For doublet admixtures above 25% the SFOEWPT reduces the possible phase-space of the trilinear coupling to smaller values. These findings are in agreement with those in Ref. [86].

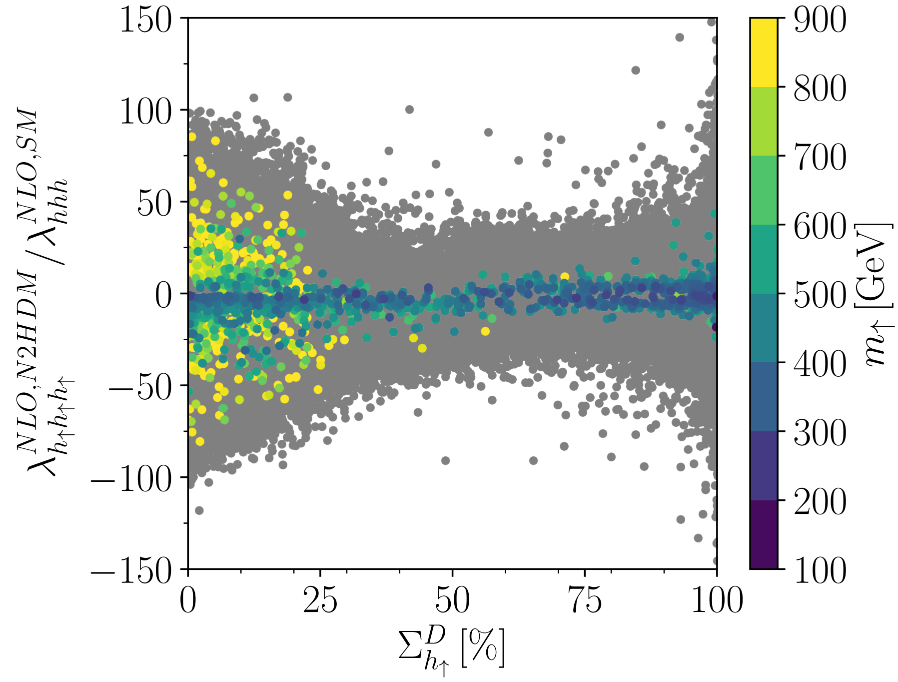

Figure 6.23: Type I and mass order M_1: The NLO trilinear self-coupling of the $h_\uparrow$ normalized to the SM value versus the doublet admixture $\Sigma^D_{h_\uparrow}$. Grey points denote the ScannerS sample and the colour code indicates $m_\uparrow$.

6.3.2 Type II: M_1

We begin the discussion of the type II N2HDM with the trilinear h_{125} self-coupling. In Fig. 6.24 the NLO versus the tree level trilinear self-coupling is shown. Again significantly enhanced self-couplings by a factor of 7.5 are compatible with theoretical and experimental constraints. The SFOEWPT on the other hand reduces these NLO enhancements down to an upper bound of 2.8 and demands a non-zero NLO and tree-level coupling at the same time. As mentioned in the type I discussion, this can be explained by the interplay between the requirement of enhanced self-couplings and a light scalar spectrum which directly affects the quartic couplings of the Higgs potential and in this way limits the NLO corrections [86]. In Fig. 6.25 the self-couplings of three $h_\downarrow$ and $h_\uparrow$, respectively, are shown. The colour code indicates the mass of the specific particle. As observed in the type I N2HDM, almost all parameter points providing an SFOEWPT lie on a straight line which indicates that the NLO self-couplings are enhanced by a factor of two compared to the leading-order self-couplings. Coming to the VeV contribution of the heaviest CP-even Higgs boson, we show in Fig. 6.26 the doublet admixture of $h_\uparrow$ versus the NLO trilinear self-coupling $\lambda_{h_\uparrow h_\uparrow h_\uparrow}$ normalized to the SM value. Again we observe that the biggest NLO self-couplings are obtained for small doublet admixtures, so that the contribution of the heaviest CP-even neutral Higgs boson to the electroweak VeV is small.

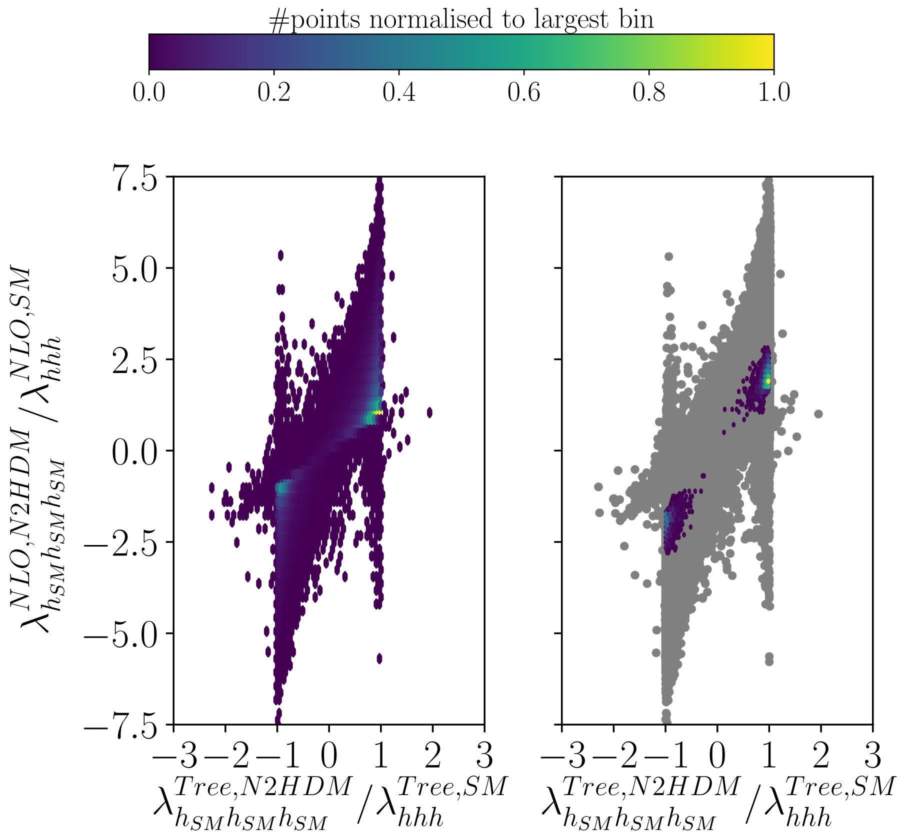

Figure 6.24: Type II and mass order M_1: The tree level trilinear self-coupling of the h_{125} versus the NLO trilinear self-coupling of h_{125} both normalized to the SM value. Left: the ScannerS sample with all parameter points fulfilling theoretical and experimental constraints; right: Grey points correspond to the ScannerS sample and the coloured points provide an SFOEWPT. The colour code denotes the relative frequency normalized to the largest bin.

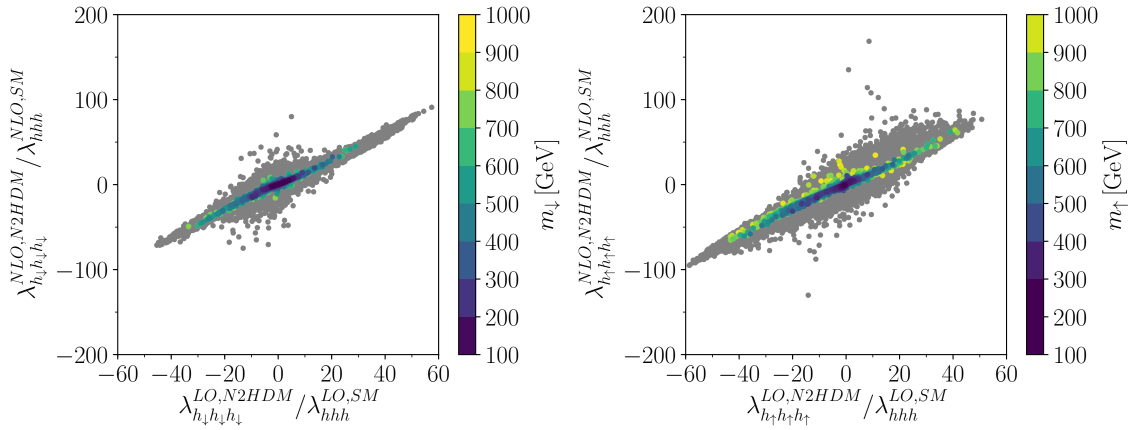

(a) (b)

Figure 6.25: Type II and mass order M_1: The tree level trilinear self-coupling of $h_\downarrow$(left) and $h_\uparrow$(right) versus the NLO trilinear self-coupling of $h_\downarrow$(left) and $h_\uparrow$(right) both normalized to the SM value. The colour code indicates $m_\downarrow$(left) and $m_\uparrow$ (right). The grey points denote the full ScannerS sample, while the coloured points provide an SFOEWPT.

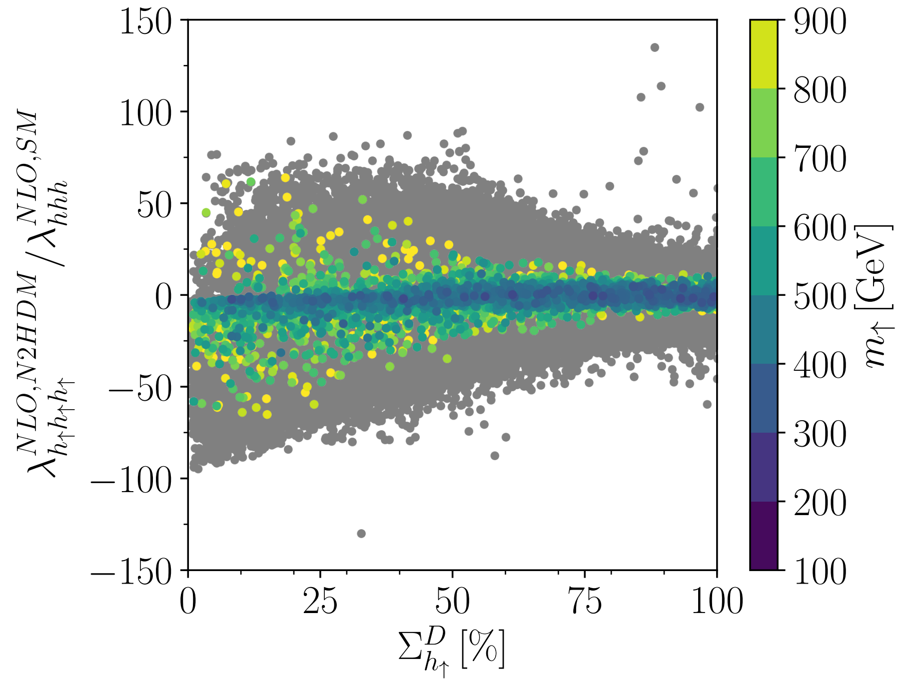

Figure 6.26: Type II and mass order M_1: The NLO trilinear self-coupling of the $h_\uparrow$ versus normalized to the SM value versus the doublet admixture $\Sigma^D_{h_\uparrow}$. Grey points denote to the ScannerS sample and the colour code indicates $m_\uparrow$.

CHAPTER 7

Conclusion

In this thesis, we studied the implications of the electroweak phase transition in an extended Higgs model, the N2HDM. This study allows to combine the experimental and theoretical constraints with the cosmological aspect, the electroweak phase transition. We used the *baryon washout condition* in order to quantify if a specific parameter setting is able to provide a sufficiently strong first order electroweak phase transition. If this condition holds for a parameter point, it can be possible to explain the observed baryon asymmetry of the universe in this setting.

We started by introducing the aspects of finite temperature field theory and the effective potential at one-loop approximation in order to be able to calculate the strength of the phase transition. We showed the subtle problems of the self-coupling expansion at finite temperature and presented the resummation prescription used in this work. Afterwards, we introduced our notation and reviewed the N2HDM and its mass spectrum. Subsequently, we introduced the new counter term prescription [14] allowing us to use one-loop masses and angles as direct input parameters. We then gave an overview of our numerical analysis and the applied constraints.

Within this work, the C++ code used for the 2HDM analysis in [14] was extended and developed for the N2HDM. The system of equations for the counter term prescription was solved and the related identities were checked numerically.

In the numerical analysis, presented in Chapter 6, we have investigated the type I and II N2HDM within all possible mass orders M_1, M_2 and M_3 and we have shown the implications on the Higgs mass spectrum by first requiring NLO stability and afterwards a strong first order electroweak phase transition. By doing so we showed that the electroweak phase transition favors mass scenarios with either degenerate pseudoscalar and charged masses or a degeneracy of one CP-even non-SM-like Higgs boson mass with the charged mass, independently of the N2HDM type and mass order. In the Higgs mass setting $m_A \approx m_{H^\pm}$, we observed a finite mass gap between the charged and the CP-even non-SM-like Higgs boson for all types and mass orders[1].

All signal rates of the promising decay channels of the SM-like Higgs boson were investigated with respect to deviations compared to the SM case. We observed that

[1] Except for the type II N2HDM in the mass order M_3, because there is no valid phase space.

the tendency of the signal rates are towards to the SM rates and in that way the N2HDM signal rates are compatible with the SM in both types and all mass orders. We investigated the constraining power on the singlet admixture to h_{125} given by the signal rates of every particular decay channel. We found agreement with [51] and concluded that in the type I model the decay $h_{125} \to ZZ$ is the most promising candidate for the first mass order. A measurement within a 5% of the SM value would allow to set an upper bound of 5% on the singlet admixture to the SM-like Higgs boson by additionally taking into account an electroweak phase transition. In the type II and mass order M_1 we observed that the $h_{125} \to \tau\tau$ channel allows to constrain the singlet admixture most efficiently. For small $\tan\beta$ the upper bound provided by ScannerS is reduced from 12% down to $\approx 8\%$ after requiring an SFOEWPT. Subsequently, in the type II discussion we excluded the wrong-sign limit in the N2HDM by requiring a strong first order electroweak phase transition. It might be possible to find a parameter point which fulfills the wrong sign condition and a phase transition, but due to the limited computation time, we did not find any valid parameter point in our analysis.
Concerning the trilinear couplings among the neutral Higgs bosons of the N2HDM, we showed that the trilinear coupling among the three SM-like Higgs bosons h_{125} are enhanced at next-to-leading order. Additionally, the electroweak phase transition requires a non-zero self-coupling which deviates significantly enough from the SM value to possibly be measurable at the LHC. We confirmed the statement in [86] that either the scalar mass spectrum is as light as possible or the lighter non-SM-like Higgs boson receives the larger portion of the VeV in order not to weaken the strength of the phase transition.
For future work, it would be interesting to scan a larger sample size in order to find more valid parameter points providing a phase transition, especially for the mass order M_2 and M_3. This might lead to valid parameter point in the type II M_3 scenario. In this specific setting a very large mass gap exists between the CP-even scalars and the pseudoscalar mass. This leads to large NLO corrections which results in the instability of the electroweak vacuum. Another interesting point for further investigations would be to consider variations of the N2HDM, like dark matter models in the framework of the N2HDM. Such studies would allow a phenomenological comparison between these models, and possible exclusion scenarios could arise to distinguish these models from other beyond Standard models.
Furthermore, in this thesis a CP-conserving model was presented, and we did not find a CP-violating phase evolving at finite temperatures, so that it would be interesting to extend the presented analysis to a complex extension of the N2HDM. In this way, it would be possible to include CP-violating effects in the analysis. Unfortunately, the complex N2HDM in its general form would consist of a very large free parameter space which complicates the phenomenological discussion.

Acknowledgments/Danksagungen

Mein besonderer Dank gilt Frau Prof. Dr. M. Margarete Mühlleitner für die spannende Themenstellung und die Möglichkeit, diese Masterarbeit am Institut für Theoretische Physik anzufertigen. Durch ihre freundliche Art fühlte ich mich gleich in ihrer Arbeitsgruppe wohl. Ihre zahlreiche Ratschläge und die gute Zusammenarbeit mit ihrer Arbeitsgruppe ermöglichten mir ein lehrreiches und produktives Arbeitsumfeld. Des Weiteren möchte ich mich bei Frau Prof. Mühlleitner für die Ermöglichung des Forschungsaufenhalts in Lissabon bedanken.
Ich bedanke mich bei PD Dr. Stefan Gieseke, der sich bereiterklärte Koferent dieser Arbeit zu sein.
I would like to thank all members of the ITP and in special the working group of Prof. Mühlleitner for the pleasant atmosphere and various discussions.
Ein weiterer besonderer Dank gilt Philipp Basler, der mir von Anfang an mehr Fragen als ich mich erinnern kann, beantwortet hat. Durch seine fröhliche Art ging der Spaß an der Arbeit auch in Zeiträumen, in denen die Numerik nicht funktionieren wollte, nie verloren. Weiterhin möchte ich mich für die Bereitstellung seines Codes, der innerhalb seiner Masterarbeit erstellt wurde, bedanken.
Ebenso möchte ich mich bei Jonas Wittbrodt bedanken, der mir das ScannerS Datensample für das N2HDM bereit gestellt und viele Fragen bezüglich ScannerS beantwortet hat.
Weiterhin möchte ich mich bei Alexander Wlotzka bedanken, der mir am Anfang meiner Arbeit mit vielen Tipps und seinen Mathematica Notebooks einen leichteren Einstieg in die Materie ermöglichte.
Ein besonderer Dank geht an Lisa Brambach, Martin Gabelmann, Thiemo Schmelzer und Matthias Linster für deren Korrektur und hilfreiche Rückmeldungen.
Nicht zuletzt möchte ich mich bei meiner Familie und meiner Freundin bedanken, die mich stets während meines Studiums unterstützt haben. Ohne sie wäre ich heute nicht da, wo ich bin.

Bibliography

[1]P. A. R. Ade et al., "Planck 2013 results. XVI. Cosmological parameters", Astron. Astrophys. **571**, A16 (2014).

[2]A. D. Sakharov, "Violation of CP Invariance, c Asymmetry, and Baryon Asymmetry of the Universe", Pisma Zh. Eksp. Teor. Fiz. **5**, [Usp. Fiz. Nauk161,61(1991)], 32–35 (1967).

[3]A. Riotto, "Theories of baryogenesis", in Proceedings, Summer School in High-energy physics and cosmology: Trieste, Italy, June 29-July 17, 1998 (1998), pp. 326–436.

[4]D. Bailin and A. Love, *Cosmology in gauge field theory and string theory* (Institute of Physics Publishing, Bristol and Philadelphia).

[5]M. Quiros, "Field theory at finite temperature and phase transitions", Helv. Phys. Acta **67**, 451–583 (1994).

[6]M. E. Carrington, "The Effective potential at finite temperature in the Standard Model", Phys. Rev. **D45**, 2933–2944 (1992).

[7]G. Aad et al., "Observation of a new particle in the search for the Standard Model Higgs boson with the ATLAS detector at the LHC", Phys. Lett. **B716**, 1–29 (2012).

[8]Z. Fodor, J. Hein, K. Jansen, A. Jaster, and I. Montvay, "Simulating the electroweak phase transition in the SU(2) Higgs model", Nucl. Phys. **B439**, 147–186 (1995).

[9]K. Jansen, "Status of the finite temperature electroweak phase transition on the lattice", Nucl. Phys. Proc. Suppl. **47**, 196–211 (1996).

[10]L. Fromme, S. J. Huber, and M. Seniuch, "Baryogenesis in the two-Higgs doublet model", JHEP **11**, 038 (2006).

[11]G. C. Dorsch, S. J. Huber, and J. M. No, "A strong electroweak phase transition in the 2HDM after LHC8", JHEP **10**, 029 (2013).

[12]J. M. Cline, K. Kainulainen, and M. Trott, "Electroweak Baryogenesis in Two Higgs Doublet Models and B meson anomalies", JHEP **11**, 089 (2011).

[13]G. C. Dorsch, S. J. Huber, and J. M. No, "A strong electroweak phase transition in the 2HDM after LHC8", JHEP **10**, 029 (2013).

[14]P. Basler, M. Krause, M. Muhlleitner, J. Wittbrodt, and A. Wlotzka, "Strong First Order Electroweak Phase Transition in the CP-Conserving 2HDM Revisited", JHEP **02**, 121 (2017).

[15]J. R. Espinosa, T. Konstandin, and F. Riva, "Strong Electroweak Phase Transitions in the Standard Model with a Singlet", Nucl. Phys. **B854**, 592–630 (2012).

[16]S. J. Huber and M. G. Schmidt, "Baryogenesis at the electroweak phase transition for a SUSY model with a gauge singlet", in Strong and electroweak matter. Proceedings, Meeting, SEWM 2000, Marseille, France, June 13-17, 2000 (2000), pp. 272–278.

[17]S. Profumo, M. J. Ramsey-Musolf, and G. Shaughnessy, "Singlet Higgs phenomenology and the electroweak phase transition", JHEP **08**, 010 (2007).

[18]M. Carena, G. Nardini, M. Quiros, and C. E. M. Wagner, "MSSM Electroweak Baryogenesis and LHC Data", JHEP **02**, 001 (2013).

[19]M. Carena, G. Nardini, M. Quiros, and C. E. M. Wagner, "The Baryogenesis Window in the MSSM", Nucl. Phys. **B812**, 243–263 (2009).

[20]C. Balazs, M. Carena, A. Menon, D. E. Morrissey, and C. E. M. Wagner, "The Supersymmetric origin of matter", Phys. Rev. **D71**, 075002 (2005).

[21]S. J. Huber, T. Konstandin, T. Prokopec, and M. G. Schmidt, "Electroweak Phase Transition and Baryogenesis in the nMSSM", Nucl. Phys. **B757**, 172–196 (2006).

[22]S. J. Huber, T. Konstandin, T. Prokopec, and M. G. Schmidt, "Baryogenesis in the MSSM, nMSSM and NMSSM", Nucl. Phys. **A785**, 206–209 (2007).

[23]A. Das, *Finite temperature field theory* (2004).

[24]J. I. Kapusta, *Finite-temperature field theory (cambridge monographs on mathematical physics)* (Cambridge University Press, July 1989).

[25]S. R. Coleman and E. J. Weinberg, "Radiative Corrections as the Origin of Spontaneous Symmetry Breaking", Phys. Rev. **D7**, 1888–1910 (1973).

[26]M. E. Peskin and D. V. Schroeder, *An introduction to quantum field theory*, 4. print. (Addison-Wesley, Reading, Mass. [u.a.], 1997).

[27]R. Jackiw, "Functional evaluation of the effective potential", Phys. Rev. **D9**, 1686 (1974).

[28]A. K. Das, "Topics in finite temperature field theory", (2000).

[29]H. H. Patel and M. J. Ramsey-Musolf, "Baryon Washout, Electroweak Phase Transition, and Perturbation Theory", JHEP **07**, 029 (2011).

[30]M. L. Bellac, *Thermal field theory* (Cambridge University Press, 1996).

[31]P. Arnold, "Phase transition temperatures at next-to-leading order", Phys. Rev. D **46**, 2628–2635 (1992).

[32]R. R. Parwani, "Resummation in a hot scalar field theory", Phys. Rev. **D45**, [Erratum: Phys. Rev.D48,5965(1993)], 4695 (1992).

[33]P. B. Arnold and O. Espinosa, "The Effective potential and first order phase transitions: Beyond leading-order", Phys. Rev. **D47**, [Erratum: Phys. Rev.D50,6662(1994)], 3546 (1993).

[34]L. Dolan and R. Jackiw, "Symmetry Behavior at Finite Temperature", Phys. Rev. **D9**, 3320–3341 (1974).

[35]H. H. Patel and M. J. Ramsey-Musolf, "Baryon Washout, Electroweak Phase Transition, and Perturbation Theory", JHEP **07**, 029 (2011).

[36]C. Wainwright, S. Profumo, and M. J. Ramsey-Musolf, "Gravity Waves from a Cosmological Phase Transition: Gauge Artifacts and Daisy Resummations", Phys. Rev. **D84**, 023521 (2011).

[37]M. Garny and T. Konstandin, "On the gauge dependence of vacuum transitions at finite temperature", JHEP **07**, 189 (2012).

[38]X.-G. He, T. Li, X.-Q. Li, J. Tandean, and H.-C. Tsai, "Constraints on Scalar Dark Matter from Direct Experimental Searches", Phys. Rev. **D79**, 023521 (2009).

[39]B. Grzadkowski and P. Osland, "Tempered Two-Higgs-Doublet Model", Phys. Rev. **D82**, 125026 (2010).

[40]H. E. Logan, "Dark matter annihilation through a lepton-specific Higgs boson", Phys. Rev. **D83**, 035022 (2011).

[41]M. S. Boucenna and S. Profumo, "Direct and Indirect Singlet Scalar Dark Matter Detection in the Lepton-Specific two-Higgs-doublet Model", Phys. Rev. **D84**, 055011 (2011).

[42]X.-G. He, B. Ren, and J. Tandean, "Hints of Standard Model Higgs Boson at the LHC and Light Dark Matter Searches", Phys. Rev. **D85**, 093019 (2012).

[43]Y. Bai, V. Barger, L. L. Everett, and G. Shaughnessy, "Two-Higgs-doublet-portal dark-matter model: LHC data and Fermi-LAT 135 GeV line", Phys. Rev. **D88**, 015008 (2013).

[44]X.-G. He and J. Tandean, "Low-Mass Dark-Matter Hint from CDMS II, Higgs Boson at the LHC, and Darkon Models", Phys. Rev. **D88**, 013020 (2013).

[45]Y. Cai and T. Li, "Singlet dark matter in a type II two Higgs doublet model", Phys. Rev. **D88**, 115004 (2013).

[46]L. Wang and X.-F. Han, "A simplified 2HDM with a scalar dark matter and the galactic center gamma-ray excess", Phys. Lett. **B739**, 416–420 (2014).

[47]A. Drozd, B. Grzadkowski, J. F. Gunion, and Y. Jiang, "Extending two-Higgs-doublet models by a singlet scalar field - the Case for Dark Matter", JHEP **11**, 105 (2014).

[48]R. Campbell, S. Godfrey, H. E. Logan, A. D. Peterson, and A. Poulin, "Implications of the observation of dark matter self-interactions for singlet scalar dark matter", Phys. Rev. **D92**, 055031 (2015).

[49]S. von Buddenbrock, N. Chakrabarty, A. S. Cornell, D. Kar, M. Kumar, T. Mandal, B. Mellado, B. Mukhopadhyaya, R. G. Reed, and X. Ruan, "Phenomenological signatures of additional scalar bosons at the LHC", Eur. Phys. J. **C76**, 580 (2016).

[50]C.-Y. Chen, M. Freid, and M. Sher, "Next-to-minimal two Higgs doublet model", Phys. Rev. **D89**, 075009 (2014).

[51]M. Muhlleitner, M. O. P. Sampaio, R. Santos, and J. Wittbrodt, "The N2HDM under Theoretical and Experimental Scrutiny", JHEP **03**, 094 (2017).

[52]G. C. Branco, P. M. Ferreira, L. Lavoura, M. N. Rebelo, M. Sher, and J. P. Silva, "Theory and phenomenology of two-Higgs-doublet models", Phys. Rept. **516**, 1–102 (2012).

[53]P. M. Ferreira, R. Santos, and A. Barroso, "Stability of the tree-level vacuum in two Higgs doublet models against charge or CP spontaneous violation", Phys. Lett. **B603**, [Erratum: Phys. Lett.B629,114(2005)], 219–229 (2004).

[54]J. E. Camargo-Molina, A. P. Morais, R. Pasechnik, M. O. P. Sampaio, and J. Wessén, "All one-loop scalar vertices in the effective potential approach", JHEP **08**, 073 (2016).

[55]E. Benazera and N. Hansen, *Libcmaes*, (2014) `https://github.com/beniz/libcmaes` (visited on 05/19/2016).

[56]M. G. et al, "Gnu scientific library reference manual", (2016).

[57]W. Grimus, L. Lavoura, O. M. Ogreid, and P. Osland, "A Precision constraint on multi-Higgs-doublet models", J. Phys. **G35**, 075001 (2008).

[58]W. Grimus, L. Lavoura, O. M. Ogreid, and P. Osland, "The Oblique parameters in multi-Higgs-doublet models", Nucl. Phys. **B801**, 81–96 (2008).

[59]M. Baak, J. Cúth, J. Haller, A. Hoecker, R. Kogler, K. Mönig, M. Schott, and J. Stelzer, "The global electroweak fit at NNLO and prospects for the LHC and ILC", Eur. Phys. J. **C74**, 3046 (2014).

[60]P. Bechtle, O. Brein, S. Heinemeyer, G. Weiglein, and K. E. Williams, "HiggsBounds: Confronting Arbitrary Higgs Sectors with Exclusion Bounds from LEP and the Tevatron", Comput. Phys. Commun. **181**, 138–167 (2010).

[61]P. Bechtle, O. Brein, S. Heinemeyer, G. Weiglein, and K. E. Williams, "HiggsBounds 2.0.0: Confronting Neutral and Charged Higgs Sector Predictions with Exclusion Bounds from LEP and the Tevatron", Comput. Phys. Commun. **182**, 2605–2631 (2011).

[62]P. Bechtle, O. Brein, S. Heinemeyer, O. Stål, T. Stefaniak, G. Weiglein, and K. E. Williams, "HiggsBounds − 4: Improved Tests of Extended Higgs Sectors against Exclusion Bounds from LEP, the Tevatron and the LHC", Eur. Phys. J. **C74**, 2693 (2014).

[63]A. Djouadi, J. Kalinowski, and M. Spira, "HDECAY: A Program for Higgs boson decays in the standard model and its supersymmetric extension", Comput. Phys. Commun. **108**, 56–74 (1998).

[64]R. V. Harlander, S. Liebler, and H. Mantler, "SusHi: A program for the calculation of Higgs production in gluon fusion and bottom-quark annihilation in the Standard Model and the MSSM", Comput. Phys. Commun. **184**, 1605–1617 (2013).

[65]R. V. Harlander, S. Liebler, and H. Mantler, "SusHi Bento: Beyond NNLO and the heavy-top limit", Comput. Phys. Commun. **212**, 239–257 (2017).

[66]G. Aad et al., "Measurements of the Higgs boson production and decay rates and constraints on its couplings from a combined ATLAS and CMS analysis of the LHC pp collision data at $\sqrt{s} = 7$ and 8 TeV", JHEP **08**, 045 (2016).

[67]H. E. Haber and H. E. Logan, "Radiative corrections to the Z b anti-b vertex and constraints on extended Higgs sectors", Phys. Rev. **D62**, 015011 (2000).

[68]O. Deschamps, S. Descotes-Genon, S. Monteil, V. Niess, S. T'Jampens, and V. Tisserand, "The Two Higgs Doublet of Type II facing flavour physics data", Phys. Rev. **D82**, 073012 (2010).

[69]F. Mahmoudi and O. Stal, "Flavor constraints on the two-Higgs-doublet model with general Yukawa couplings", Phys. Rev. **D81**, 035016 (2010).

[70]T. Hermann, M. Misiak, and M. Steinhauser, "$\bar{B} \to X_s\gamma$ in the Two Higgs Doublet Model up to Next-to-Next-to-Leading Order in QCD", JHEP **11**, 036 (2012).

[71]M. Misiak et al., "Updated NNLO QCD predictions for the weak radiative B-meson decays", Phys. Rev. Lett. **114**, 221801 (2015).

[72]M. Misiak and M. Steinhauser, "Weak radiative decays of the B meson and bounds on $M_{H^\pm}$ in the Two-Higgs-Doublet Model", Eur. Phys. J. **C77**, 201 (2017).

[73]G. Aad et al., "Combined Measurement of the Higgs Boson Mass in *pp* Collisions at $\sqrt{s} = 7$ and 8 TeV with the ATLAS and CMS Experiments", Phys. Rev. Lett. **114**, 191803 (2015).

[74]K. A. Olive et al., "Review of Particle Physics", Chin. Phys. **C38**, 090001 (2014).

[75]L. H.C.S. W. Group, (2016) `https://twiki.cern.ch/twiki/bin/view/LHCPhysics/` (visited on 06/06/2016).

[76]S. Dittmaier et al., "Handbook of LHC Higgs Cross Sections: 1. Inclusive Observables", (2011) `10.5170/CERN-2011-002`.

[77]G. C. Dorsch, S. J. Huber, K. Mimasu, and J. M. No, "Echoes of the Electroweak Phase Transition: Discovering a second Higgs doublet through $A_0 \to ZH_0$", Phys. Rev. Lett. **113**, 211802 (2014).

[78]CMS, "Search for extended Higgs sectors in the H to hh and A to Zh channels in sqrt(s) = 8 TeV pp collisions with multileptons and photons final states", (2013).

[79]*Beyond Standard Model Higgs boson searches at a High-Luminosity LHC with ATLAS*, tech. rep. ATL-PHYS-PUB-2013-016 (CERN, Geneva, 2013).

[80]G. C. Dorsch, S. J. Huber, T. Konstandin, and J. M. No, "A Second Higgs Doublet in the Early Universe: Baryogenesis and Gravitational Waves", JCAP **1705**, 052 (2017).

[81]P. M. Ferreira, R. Guedes, M. O. P. Sampaio, and R. Santos, "Wrong sign and symmetric limits and non-decoupling in 2HDMs", JHEP **12**, 067 (2014).

[82]X.-F. Han and L. Wang, "Wrong sign Yukawa coupling of 2HDM with a scalar dark matter confronted with dark matter and Higgs data", (2017).

[83]K. Cranmer, S. Kreiss, D. Lopez-Val, and T. Plehn, "Decoupling Theoretical Uncertainties from Measurements of the Higgs Boson", Phys. Rev. **D91**, 054032 (2015).

[84]J. Baglio, A. Djouadi, R. Gröber, M. M. Mühlleitner, J. Quevillon, and M. Spira, "The measurement of the Higgs self-coupling at the LHC: theoretical status", JHEP **04**, 151 (2013).

[85] S. Kanemura, S. Kiyoura, Y. Okada, E. Senaha, and C. P. Yuan, "New physics effect on the Higgs selfcoupling", Phys. Lett. **B558**, 157–164 (2003).

[86] P. Basler, M. Mühlleitner, and J. Wittbrodt, "The CP-Violating 2HDM in Light of a Strong First Order Electroweak Phase Transition and Implications for Higgs Pair Production", (2017).